Deformation bands in chalk – control on distribution and mechanism of formation.

Master thesis in Geodynamics

Heidi Husebø Knutsen

Department of Earth Science

University of Bergen

June, 2016

Abstract

Deformation bands are narrow tabular zones that accommodates strain through the reorganization of grains by shearing and/or volumetric deformation in porous and granular rocks. Deformation bands in porous sandstones are widely documented, fewer studies are done on deformation bands in porous carbonate rocks. There are even fewer published examples of deformation bands in porous chalk. Inspired by this fact, the current study presents the results of detailed thin-section and SEM analyses of deformation bands present within carbonate rocks from the Upper Maastrichtian to Danian chalk from the Oseberg Field area, northern North Sea.

The studied deformation bands are hosted in chalks from the Hardråde/Jorsalfare Formation in the Oseberg fault block in association with stylolites, located 2200 to 2300 m below the sea level. The deformation bands found in the chalk are very thin with a μm-scale thickness, i.e. much thinner than mm- to cm-thick deformation bands typically found in porous sandstones and carbonate grainstones. Two types of deformation bands have been described and classified in the chalk by structural analysis and microscopic investigations: (1) bed-parallel compaction bands (CBs) and (2) bedding-oblique solution-compactive shear bands (SCSBs). For the structural analysis of the deformation bands in the studied cores, methods include recording the frequency of deformation structures (the amount of deformation structures bisecting the scanline per 0.2 m) along scanlines and the orientations of the different deformation structures that bisect the scanline. The microstructural characterization of the deformation bands involved thin-section analysis by means of the optical microscope and SEM. The porosity measurements of the deformation bands and the host rock were performed by the ImageJ software.

Both deformation bands and extension fractures seem to be present in the chalk as what has been referred to a "hairline fractures" or "healed fractures". Due to the difficulty of distinguishing the two different deformation structures at the macroscopic scale, it has been concluded that microscopic analysis is necessary to distinguish between the two.

In this work, the deformation bands are suggested to have been formed due to burial and differential compaction, where the maximum stress axis (σ_1) was oriented perpendicular to the bedding. Differential compaction could have occurred due to lateral variation in the thickness to the fault basin filled sediments comprising of the syn-rift sediments of Jurassic and the post-rift sediments of Cretaceous overlain by Cenozoic sediments. Evident by the top Cretaceous sediments shaping out as an open anticline, the differential compaction would have applied even more strain to the bedding than burial compaction alone.

The deformation band features where not easy to observe in SEM-images. Their narrowness, with an apparent thickness of about 30-220 μm, could be one of the reasons why these features easily have been overlooked in many chalk reservoirs. The grain size reduction has occurred solely by disaggregation of grains and pressure solution mechanism. It is suggested by this study that the stylolites is the baffle and controls the conduits of fluid flow, with some influence by the deformation bands within the studied chalk reservoir.

Acknowledgements

First and foremost, I would like to thank my admirable supervisors Prof. Haakon Fossen, Prof. Atle Rotevatn and Dr.Ole Petter Wennberg (Statoil) for guidance and support. I wish to thank Statoil Research Centre in Bergen for the usage of their cores and to Geir Torkildsen (Statoil) for the preparation of good thin section samples for this project.

I would also like to thank Niels Bo Jensen and Thomas Thuesen for their expertise regarding the ImageJ software. Casey Nixon is thanked for helping with my data analysis, Egil S. Erichsen and Irene Heggstad for the supervision regarding the SEM.

I would like to thank my good friends and fellow students at the University of Bergen for five great and memorable years, at the university, the field trips, UNIS and other social gatherings. Particularly I want to mention Karen and Louise for all our memorable moments and how we would “get in the water”. In addition, I would also like to mention Marthe, Ingvild, Ragnhild, Anna KD, Maria, Synne, Vilde, Karoline, Erika and the people at “Hovedkvarteret” Idun, Emilie, Eva and Merethe for the daily support, motivation and help through this journey.

I want to thank my grandparents, my grandfather who put me on this path to become a geologist, unfortunately you past away right before I attended the University. My grandmother for the continuous support in life, whom I almost lost this winter, and to my mother. These people are my biggest inspirators in life.

An extra gratitude towards my parents in “law” for the support and help through this hectic times. Finally, I would like to thank my partner in life Runar S. Kristensen for his support and love during my time of needs. You mean everything to me.

Bergen, 30th of June 2016

Heidi

Heidi Husebø Knutsen

Table of Contents

1.Introduction

This study is based on a project done by Wennberg et al. (2013), on deformation bands in the Upper Maastrichtian to Danian chalk of the Shetland Group in the Oseberg Field area. It has been a challenge to visualize the deformation mechanism (Wennberg et al., 2013), therefore still many questions related to the evolution of deformation mechanism for deformation bands found in chalk. The aim of this master thesis is to improve the knowledge on deformation bands and “hairline fractures” found in chalk. The focus will be on the geometry, microstructures and deformation mechanisms of the deformation bands within chalk, in addition to investigate if hairline fractures could be identified as deformation bands.

1.1 Previous work

Deformation bands were first observed and described in porous sandstone by Aydin (1978), as narrow tabular zones of localized strain. Since then deformation band in porous sandstones have been vastly described both in the field (Aydin and Johnson, 1978, Aydin and Johnson, 1983, Aydin, 1978, Antonellini and Aydin, 1994, Fossen and Hesthammer, 1997, Aydin et al., 2006, Fossen et al., 2007) and in laboratory experiments (Mair et al., 2000, Vajdova et al., 2004). In year 2000, deformation bands were first reported by the use of laboratory experiments in porous carbonate rocks (Baud et al., 2000, Vajdova et al., 2004). In 2006, these deformation bands were for the first time observed in the field (Tondi et al., 2006, Tondi, 2007, Antonellini et al., 2008, Cilona et al., 2012) , and then afterwards came papers on deformation bands in chalk (Wennberg et al., 2013, Gaviglio et al., 2009, Kaminskaite et al., 2015).

The petroleum industry took special interest when it was proven that deformation bands could have potential to be barriers, and/or baffles to fluid flow in a reservoir (Hesthammer and Fossen, 2000). Deformation bands are capable to modify the porosity and permeability relatively to their medium of porous granular host rock (Antonellini and Aydin, 1994). This has also given interest to deformation bands regarding carbon capture and storage (CCS) (Liteanu et al., 2013).

Deformation bands are considered to be important due to providing key information on the evolution of deformation and faulting within porous rocks (Aydin et al., 2006, Fossen et al., 2007, Aydin and Johnson, 1978, Rotevatn et al., 2007). Their features can acts as an imprint on deformation mechanisms that has taken place within the host rock. There are found many similarities between deformation bands in porous sandstones and in porous carbonates, however there are some differences (Rustichelli et al., 2012, Rotevatn et al., in press). Less is known about deformation bands in porous chalk due to the very fine grained sediments of micrite crystals and fragmented coccoliths.

1.2 Objectives

The aim to this study is to address the kinematic and mechanical controls on developing the deformation bands in the Shetland chalk from the Oseberg Field area. More specifically, this study will aim to: i) identify the deformation mechanisms and discuss the kinematic evolution of the deformation bands found in the chalk from the Oseberg Field area, ii) investigate if the "hairline fractures" could be identified as deformation bands and iii) document and describe the structural characteristic and spatial distribution of the deformation bands related to other deformation structures found in the chalk from the Oseberg Field area. The aims are achieved through the following set of objectives:

- Qualitative description of the lithological and structural controls on the distribution patterns.
- Quantitative measurements of the deformation bands frequency and orientations along a scanline on the core from well 30/9-B-46A.
- Analyse of the microstructural and lithological characteristics of the deformation bands relative to the host rock by means of a standard optical microscope and a scanning electron microscope (SEM).

1.3 Background and data

Given data to this study and interpretation of the deformation band provided by Wennberg et al. (2013) is here by presented in the following sections. Three cores from the wells 30/9-B-44B and 30/9-B-46A where provided and their facies presented by (GEUS, 2010) and (GEUS, 2011)

1.3.1 Core

109 m of core from the Shetland Croup chalk were available for this study (Fig.1.1). The cores where taken from two wells: 30/9-B-44B and 30/9-B-46A. Both wells are deviated nearly 60° in the cored interval. See table 1.1 for details.

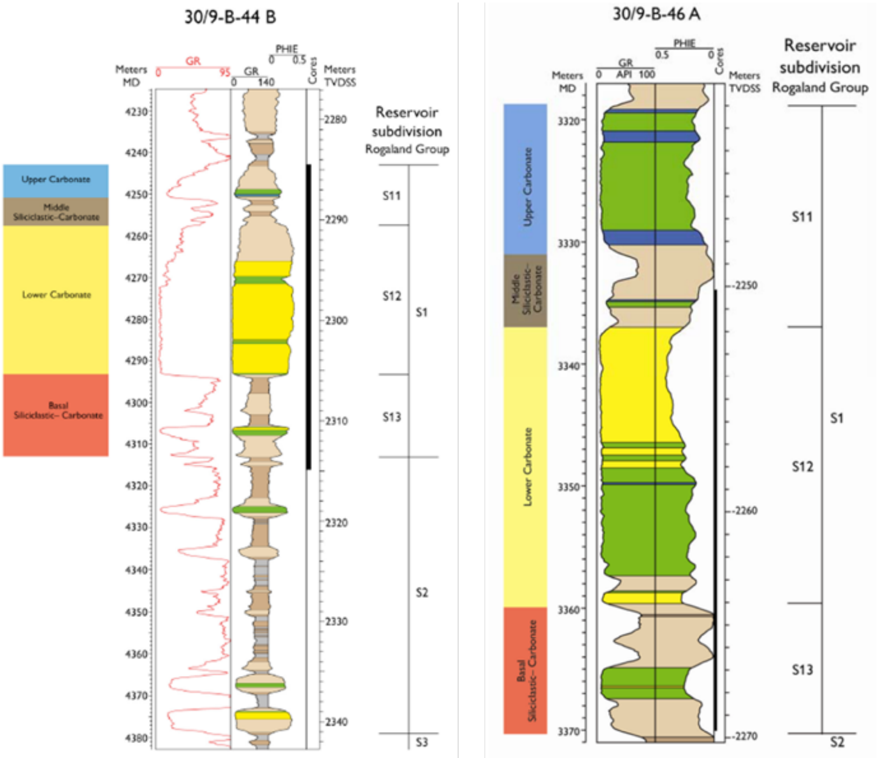

Figure 1.1: Gamma Ray, Sonic and PHIE log data from well 30/9-B-44B to the left and well 30/9-B46A to the right. The cored interval is highlighted by the black line to the right of the logs. The porosity values are based on the log data. Brown shades indicate clay-rich lithology, blue is porosity of 15 % or less, green specifies porosity between 15 and 25 % and yellow is porosity of 25 % or higher. The subdivisions of the uppermost Shetland Group are indicated to the left of the log data to the wells. Modified from GEUS (2011).

Table 1.1: Available cores from the Shetland Group chalk

Well	Number of cores	Depth (m MD)	Well deviation/ hole azimuth
30/9-B 44 B	2	4242.00 to 4315.18	65.5/303
30/9-B 46 A	1	3334.00 to 3369.86	57/048

1.3.2 Facies

The six different facies in the Shetland Group chalk in the Oseberg Field was carried out by GEUS (2010) and (2011) by the use of the A-cut of the cores, and published by Wennberg et al. (2013) (Fig. 1.2 and Table 1.2). All the six facies were recognized in the cores from well 30/9-B-44B, while facies 3 was absent in the core from well 30/9-B-46A. This might be because the facies are missing stratigraphically in well 30/9-B-46A.

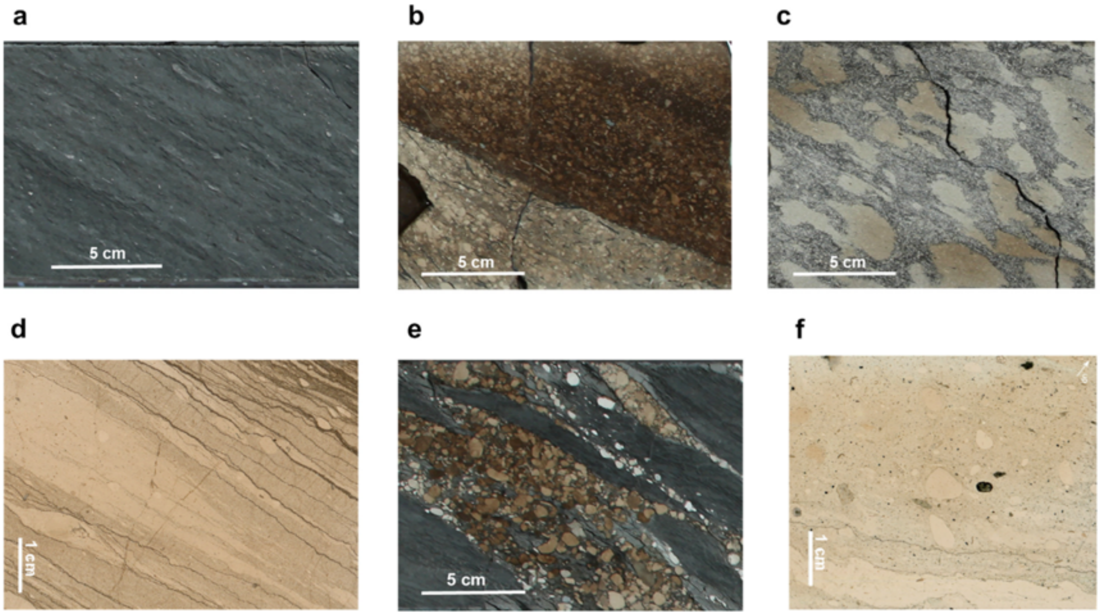

Figure 1.2 : The different facies interpreted by GEUS (2010) and GEUS (2011). a) Facies 1 – hemipelagic marlstone/claystone, b) facies 2 – graded chalk trubidites, c) facies 3 – burrowed bioclastic turbidites, d) facies 4 – shredded, intraclastic chalk, e) facies 5 – interleaved pebbly chalk-shale debrites and f) facies 6 – pebbly chalk debrites. From Wennberg et al. (2013)

Table 1.2: Facies interpretation to the cores, provided by GEUS (2010) and GEUS (2011)

Facies	**Name**	**Description**
1	Hemipelagic marlstone/claystone	Fine grained siliciclastic mud-dominated facies composing calcareous mudstones grading to marlstone, possibly deposited from suspension in a low-energy offshore environment.
2	Graded chalk trubidites	Chalk beds grading from calcarenitic (sand-grade) intraclastic-skeletal packstones-grainstones to wackstone-mudstone of up to about 1 m in stratigraphic thickness. The facies is recorded episodically where the chalk beds of carbonate sand and mud is introduced into siliciclastic-dominated environments by means of sediment gravity flows.
3	Burrowed bioclastic turbidites	Sharp-based grain-rich limestone beds showing marly-speckling. The grainstones and marly packstones consist of sand-sized skeletal fragments. The sharp bases suggest turbidity or storm-induced currents.
4	Shredded, intraclastic chalk, shear deformed mass flows	Chalks ranging from lime mudstones to foraminiferal wackstone that display varying degrees of internal deformation, from laminated and shredded, boudinaged chalks to intraclast-rich pebbly chalks. These chalks are interpreted to have been deposited by mass-flows that underwent internal deformation either during slumping/sliding prior to rafting of chalk slabs in mass flows or during late stage shear of such rafts within decelerating, progressively freezing debris flows.
5	Interleaved pebbly chalk-shale debrites	Sharp-based, disorganised and shale-rich conglomeratic facies deposited from sediment gravity flows.
6	Pebbly chalk debrites	Similar to facies 5, however lacks the siliciclastic mudstone/marlstone rafts and matrix. The pebbly chalk features reflect debris flow processes.

1.3.3 The deformation band interpretation provided by Wennberg et al. 2013

The deformation bands observed by Wennberg et al. (2013) were investigated using thin-section analysis, scanning electron microscope (SEM) and computed tomography (CT). A porosity calculation on a profile over a deformation band reported in facies 4 – intraclastic chalk by Wennberg et al. (2013) showed a reduction in porosity down to 10% compared to the host rock having a porosity of about 30-40 % (Fig. 1.3).

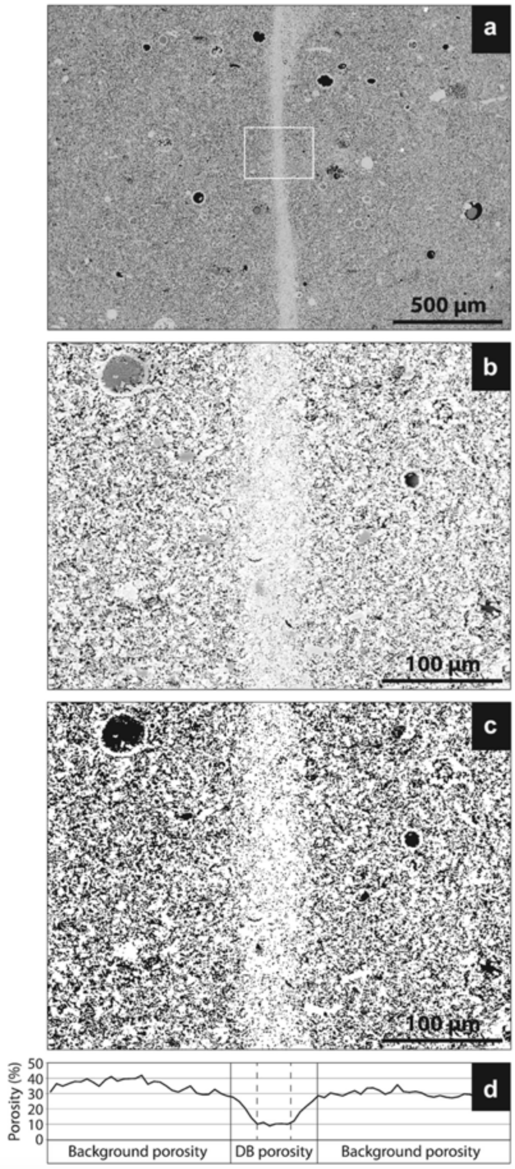

Figure 1.3: A porosity measurement done on a deformation band found in facies 4. This thin section was not provided to this master thesis, and is therefore not included in the following. From Wennberg et al. (2013).

The apperent thickness ranges from less than 0.05-0.5 mm (Fig.1.4), the narrowsness is thought to be the reason why these features have not previously been recognized as deformation band, rather it has been refered to as hairline fractures. No clear indication of shear movement were observed in the bands, however the deformation bands are observed in conjugated patterns which is suggested to indicate a component of shear movement. The deformation bands is therefore been interpreted to be developed as compactional shear bands (Wennberg et al., 2013).

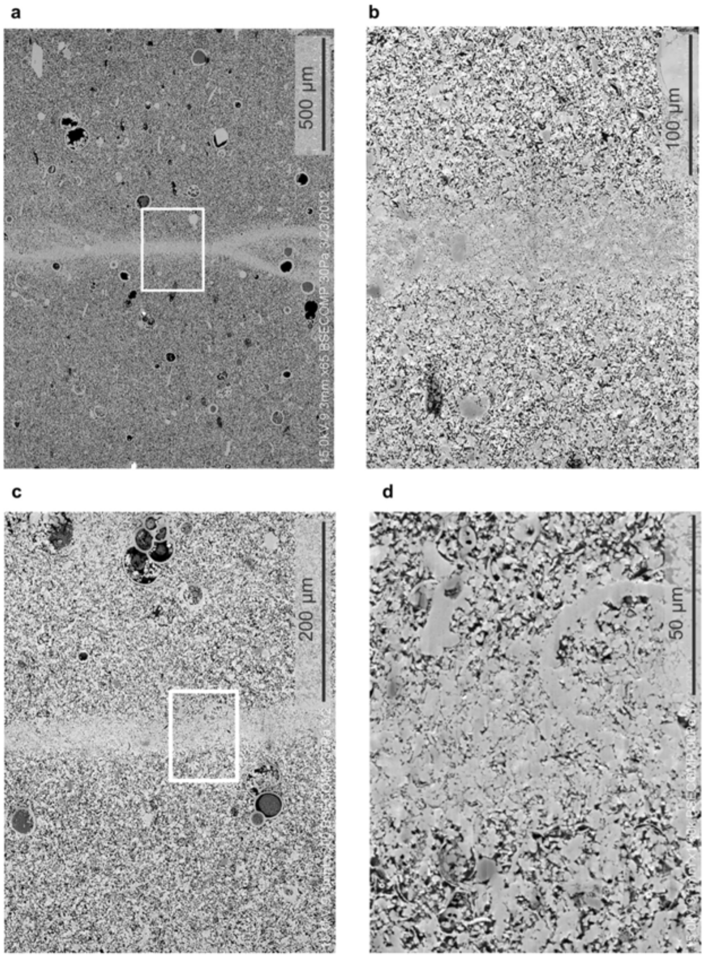

Figure 1.4: Deformation band at different magnification in BSE-SEM image. From well 30/9-B-44B, in facies 2 located at 4305.5 m MD. This thin section was provided for this master thesis and will further be discussed in section 5.

The hairline fractures are observed as dark narrow lines with respect to the host rock, which is in contrast to previous papers on deformation bands found in porous sandstones and carbonates (Tondi et al., 2012). Little is known about the nature of why the different in appearance occur between the different types of rock (Wennberg et al., 2013).

2. Geological setting of the study area

The study area is located in the Oseberg fault block, which is a fault-controlled basin bordered by two main faults, the Brage Fault to the east and the Oseberg Fault towards the west (Færseth and Ravnås, 1998) (see well location in Fig. 2.1). The Oseberg fault block developed during two significant rifting phases. The following chapter will provide an overview of the tectonic evolution of the Viking Graben, with focus on the Oseberg structure in the northern part.

2.1 Regional tectonic framework

2.1.1 Tectonic evolution of the northern North Sea

The Viking Graben shows evidence of a two-phase rifting history, where the early rift phase took place during the Permo-Triassic, and the second phase resumed during the Late Bajocian and lasted to the Berriasian (Badley et al., 1984, Badley et al., 1988, Færseth and Ravnås, 1998, Coward et al., 2003, Færseth et al., 1995).

During Late Permian and Early Triassic, the supercontinent Pangea started to split up (Nystuen et al., 2006). Significant E-W extension occurred along a weakness zone between Greenland and Norway, where the older Iapetus Ocean had closed at the end of Siluran by the making of the Caledonian orogeny developed shear zones. Rift basins were made by N-S trending normal faults and the northern Boreal Sea perforated southwards (Nystuen et al., 2006, Heeremans and Faleide, 2004, Fossen et al., 2008, Steel and Ryseth, 1990), see Fig. 2.1. The faulting during the Triassic was remarkable in the region of the Øygarden Fault Complex close to the Norwegian mainland (Steel and Ryseth, 1990). The Permo-Triassic rift phase was also more significant than the Mid-Jurassic – Early Cretaceous extension (Odinsen et al., 2000a).

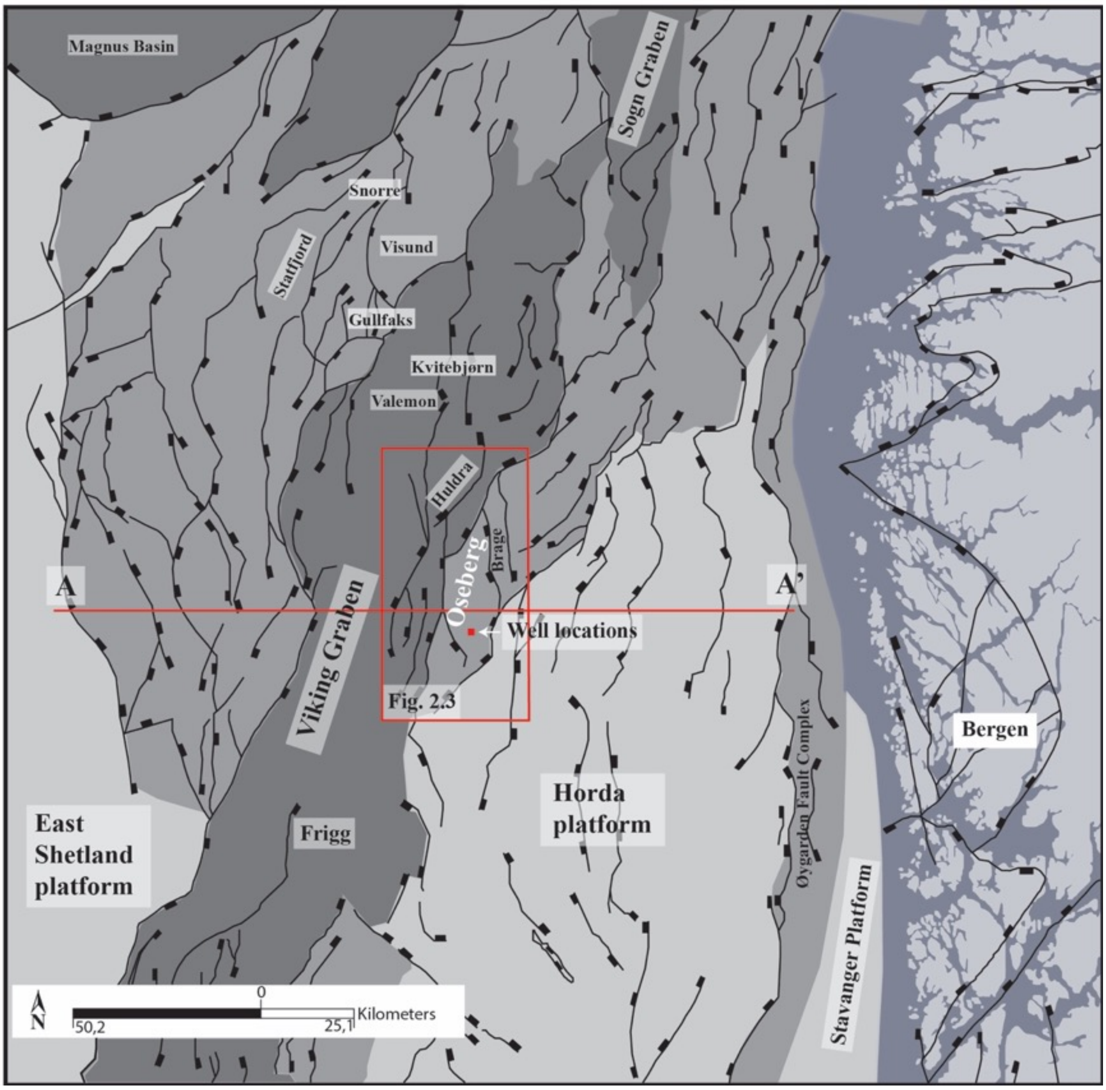

Figure 2.1: Regional map of the South Viking Graben, modified from Færseth and Ravnås (1998) and NPD (2016a). The Oseberg fault block is indicated within the red polygon, and a cross-section is made along the A-A' profile visualized in Fig. 2.2. The colouring background show the different between coastalplain – dark blue, platforms – light grey, grabens and basins – dark grey. The main fault patterns result from Permo-Triassic and Jurassic extensional episodes.

Throughout the Early Jurassic only mild extensional tectonics influenced the basin. The northern North Sea with its Permo-Triassic rift topography underwent thermal subsidence, which led to a north-directed transgression that established a seaway through the Viking Graben (Odinsen et al., 2000a, Odinsen et al., 2000b, Folkestad et al., 2014, Steel, 1993). The Lower Jurassic Statfjord Formation and the Dunlin Group show an overall thickness distribution that can indicate the Early Jurassic Viking Graben was an asymmetric basin (Fig.2.2) (Færseth and Ravnås, 1998). Fault-related subsidence started to accelerate from the Late Bajocian reactivating former Permo-Triassic master faults (Færseth and Ravnås, 1998, Yielding et al., 1992, Færseth, 1996). The Late Bajocian to Bathonian extension was relatively minor, corresponding to the rotational tilting of fault blocks (Helland-Hansen et al., 1992). The most significant rifting phase of the Viking Graben occurred through Late Jurassic. During the Callovian to Early Kimmeridgian; the rifting in the Arctic expanded towards the North Sea. North to north-easterly trending transfer and normal faults with north-westerly trending tear formed in the Viking Graben. In the eastern part of the Viking Graben, the major Øygarden Fault Complex were abandoned as the basin grew further west (Coward et al., 2003, Færseth and Ravnås, 1998, Gabrielsen et al., 2001).

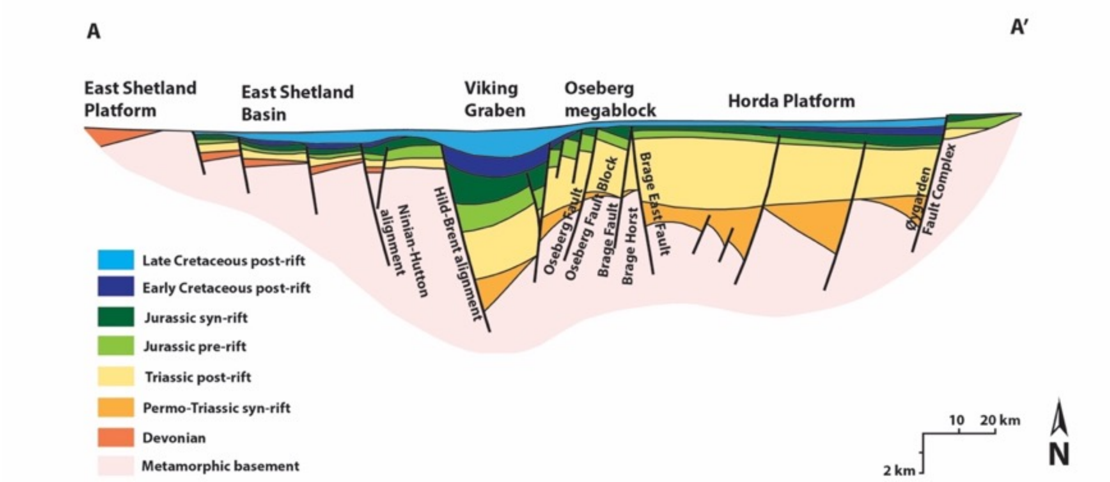

Figure 2.2: Cross-section displaying the Oseberg fault block and the major faults developed during Permo-Triassic and Jurassic extension episodes. Modified from Færseth and Ravnås (1998).

During Early Cretaceous, extension terminated along the central and North Sea and transgressive sediments covered the rift topography, creating the well-known Base Cretaceous Unconformity (BCU). The inherited structural features from the syn-rift basen created by the second rifting phase in Jurassic, had a strong influence on the basin outline and sediment supply during Cretaceous (Gabrielsen et al., 2001). Due to compaction of earlier sediments, several pulses of reactivation of the major faults occurred, however there were relatively little rift activity going on in the North Atlantic throughout the Cretaceous (Gabrielsen et al., 2001, Odinsen et al., 2000a).

The region experienced passive thermal subsidence, which precipitated mass movement of chalk to redeposit in slope and basinal settings in the Central North Sea. Basinal development in the area was also affected by the closing of the Tethys Ocean to the south-east and the opening of the North Atlantic Ocean to the north and west (Coward et al., 2003, Brekke and

Olaussen, 2006). The succession of the area was dominated by carbonates deposited from the ocean in the south and siliciclastic deposits in the north during the transgressive phase between Campanian to Maastrichtian times (Late Cretaceous) (see Fig. 2.3) (Surlyk et al., 2003). During Oligocene, the area was subjected to uplift and erosion of the Cretaceous and the Paleogene sediments occurred (Cowie and Karner, 1990, Ziegler, 1987). The steady subsidence and abundant supply of sediment from the uplifted margins led to massive accumulation of Upper Cenozoic deposits in the North Sea (Coward et al., 2003).

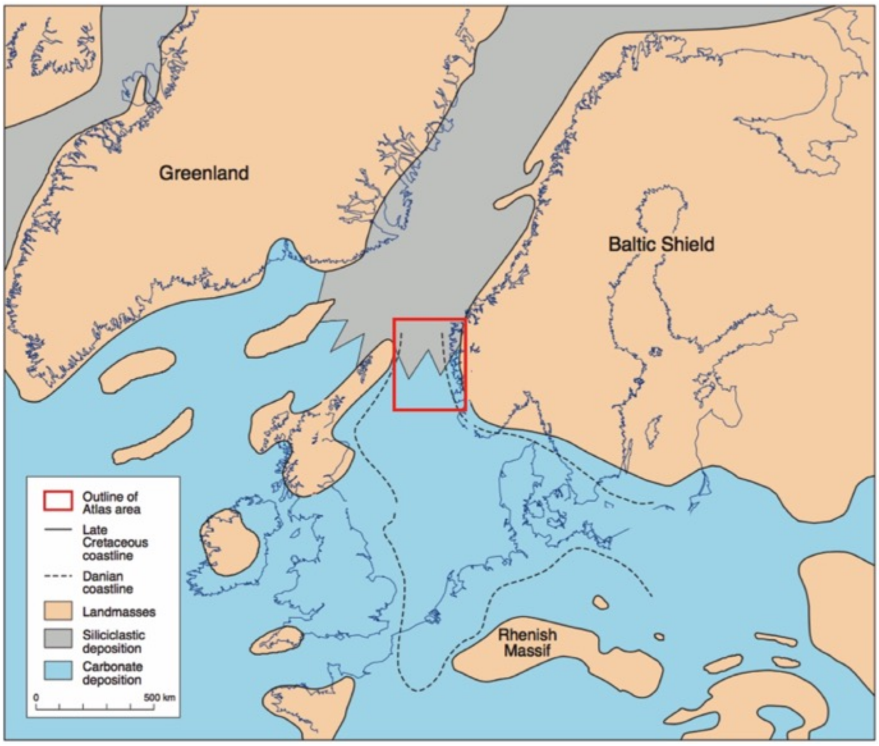

Figure 2.3: The extent of the seas during Campanian to Maastrichtian times (Late Cretaceous). Note the siliciclastic deposits in the north extending towards the carbonate deposits in the south within the red polygon. The red polygon indicates the Fig. 2.1. Modified from (Surlyk et al., 2003)

2.1.2 The Oseberg structure

The Viking Graben in the northern North Sea is a graben made up by E-W extended crust, bordered by the Shetland Platform to the west and the mainland of Norway to the east. The Oseberg fault block is located at the east flank of the Viking Graben, bounded by the Brage and Oseberg faults (Færseth and Ravnås, 1998) (see Fig. 2.2). Throughout the Permo-Triassic extension, the Oseberg fault block was part of a wider and westerly tilted fault-block, boarded by the east-dipping Brage east fault and to the west by Hilde-Brent alignment

(Færseth and Ravnås, 1998, Færseth, 1996) (see Fig. 2.4). The faults towards the western margin of the Viking Graben have a Permo-Triassic origin, whereas the majority of faults to the east are interpreted to result from Jurassic rifting (Færseth, 1996).

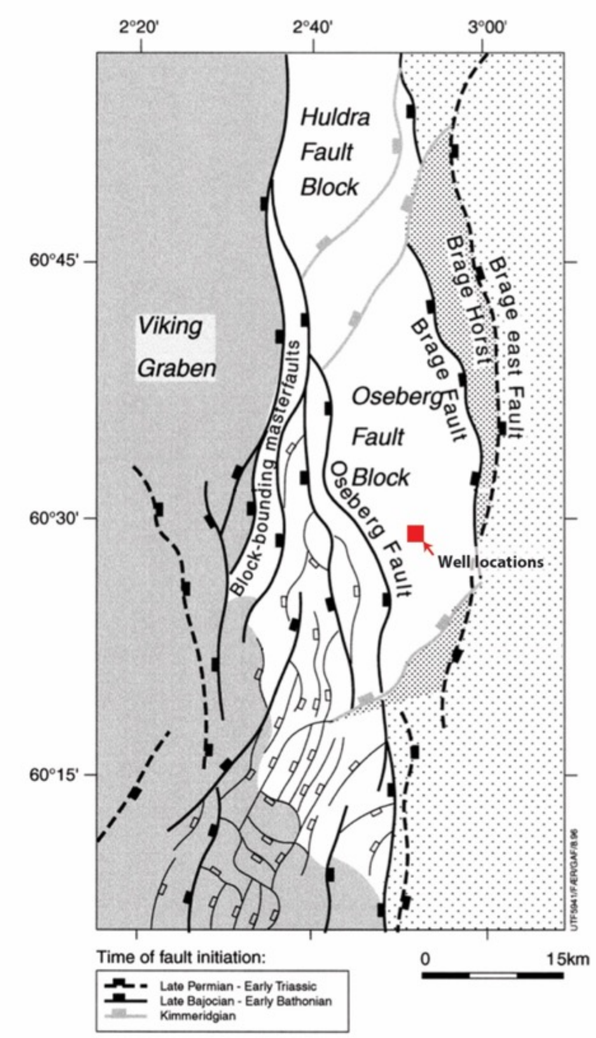

Figure 2.4: The Oseberg fault block with its major faults indicated by their time of initiation. The well locations are indicated by the red square. Modified from Færseth and Ravnås (1998).

During the Pliensbachian and Aalenian (Lower Jurassic), the Oseberg area underwent erosion due to uplift and minor fault-block rotation. The main rift stage in the Oseberg area is marked by an accentuated rotational extensional faulting dated to the Bajocian (Mid-Jurassic) (Helland-Hansen et al., 1992). The Brage fault transected the footwall of the older Brage east fault, developing the Brage Horst structure. West of the Brage fault, several west-dipping faults occurred accompanied with fault-block tilting and footwall uplift. Each fault-block developed a basin for subsidence, while the uplifted crestal area underwent erosion, wedge-shaped stratal packages was deposited on individual fault-blocks. The Brage Fault became significant, and during the Bajocian-Bathonian (Mid-Jurassic) transition, the Oseberg fault block became separated from the Horda Platform (Færseth and Ravnås, 1998).

The Brage Fault reached its peak of activity in the Callovian and the Late Oxfordian-earliest Kimmeridgian (Mid- to Late Jurassic), with a maximum throw of about 700 m. The Brage Fault movement declined during mid-Kimmeridgian-Volgian (Late Jurassic). The main Jurassic extension became concentrated in the Viking Graben, and the Oseberg fault block together with the westernmost Horda platform was subjects to significant uplift. At the same time northeast-southwest trending faults formed, separating the Oseberg og Huldra fault blocks. The combination of north-south and northeast-southwest striking faults bounded rhomb-shaped sub-basins which were separated by a complex array of intra- and inter-basinal highs, that prevented water circulation and enhanced anoxic bottom conditions (Færseth and Ravnås, 1998).

The Oseberg fault block endured as a submarine high after the Jurassic rifting, while Cretaceous sediments accumulated west and southwest over the structure, reaching a thickness of more than 2500 m in the Viking Graben. In the Campanian-Maastrichtian time (Upper Cretaceous), mass movements of sediments eroded the topographic highs of the Oseberg fault block (Færseth and Ravnås, 1998).

2.2 Jurassic-Cretaceous regional stratigraphic framework

The stratigraphy in the Oseberg fault block is presented in Fig. 2.5, and is divided into the early rift phase during Late Permian – Early Triassic and the second rift phase during Mid-Jurassic – Early Cretaceous. Each rift phase is further subdivided into a syn-rift and a post-rift lithostratigraphic units (Færseth and Ravnås, 1998). The stratigraphy comprising the studied cores are part of the post-rift unit of the second rift phase during the Upper Cretaceous.

2.2.1 Early rift phase: Late Permian – Early Triassic

2.2.1.1 Syn-rift

For most of the Triassic Period the studied area was dominated by continental deposition driven by subsidence by the early rift phase during Late Permian and Early Triassic (Vollset and Doré, 1984). The Hegre Group was then deposited as a pre-Rhaetian Triassic rock, consisting of interbedded sandstones, claystones and shale deposited in a terrestrial environment (Hesthammer and Fossen, 1999, Vollset and Doré, 1984).

2.2.1.2 Post-rift

The post-rift stratigraphy deposited after the Permo-Triassic rifting on the Oseberg fault block comprises of the fluvial-dominated Statfjord Formation, the marine-dominated Dunlin Group, the coastal-dominated Oseberg, Rannoch-Etive and Ness Formations of the Brent Group (Fig. 2.5) (Deegan and Scull, 1977). The sea level rose during Late Triassic time, establishing marine environment in the study area (Vollset and Doré, 1984). Statfjord Formation consists of relative massive and clean fluvial sandstones, exhibiting a transition from continental to shallow marine sediments (Vollset and Doré, 1984). Whereas the Amundsen –Burton, Cook and Drake Formations of the Dunlin Group comprises of shallow marine shale, claystones and siltstones. (Hesthammer and Fossen, 1999, Vollset and Doré, 1984, Deegan and Scull, 1977). The post-rift deposits of the Brent Group consist of coastal sediments from the deltaic Oseberg, Rannoch-Etive and Ness Formation (Folkestad et al., 2014).

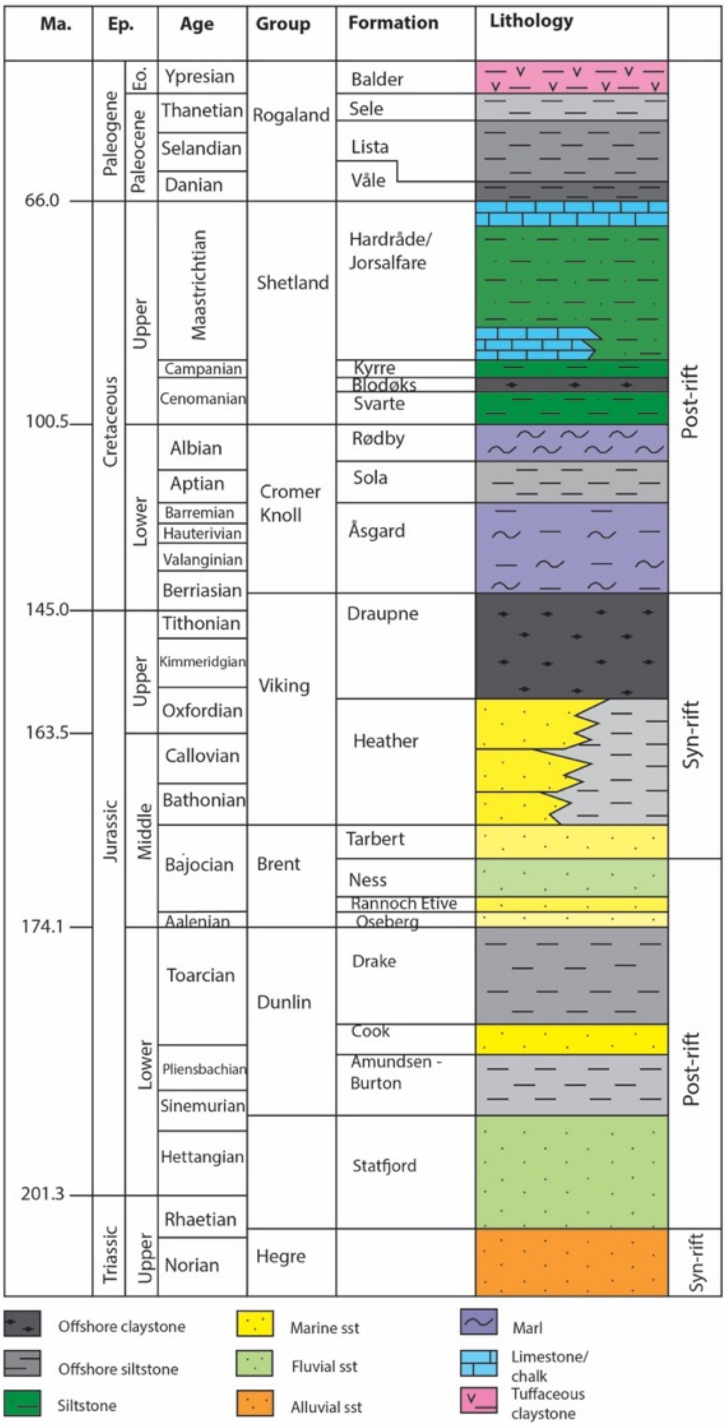

Figure 2.5: Upper Perm and Lower Tertiary stratigraphy of the Oseberg Field area. The relative thickness for each formation are not true and are only for chronological representation. Modified from Isaksen and Tonstad (1989), Vollset and Doré (1984) and Færseth and Ravnås (1998)

2.2.2 Second rift phase: Mid-Jurassic – Early Cretaceous

2.2.2.1 Syn-rift

The Ness Formation is overlain and locally truncated by the Tarbert Formation, both are part of the Brent Group and of medium grained sandstones (Vollset and Doré, 1984). The Tarbert Formation, however, where deposited during the second rifting phase during Middle Jurassic and is the first syn-rift succession of this rift phase. The general rift framework of the early rifting phase from Permo-Triassic where inherited when the second rift phase occurred in Mid-Jurassic (Vollset and Doré, 1984, Ziegler and Maatschappij's-Gravenhage, 1982).The syn-rift stratigraphy deposited during Mid-Jurassic comprises of the shallow marine-dominated Tarbert Formation of the Brent Group, the marine-dominated Heather Formation and the deep marine-dominated Draupne Formation composes the syn-rift stratigraphy of the Oseberg fault block (Deegan and Scull, 1977).

In the Oseberg structure the early syn-rift sediments are recognized either by aggradation to backstepping of shoreline or concentration of offshore mudstones (Færseth and Ravnås, 1998). According to Prosser (1993), are syn-rift deposits are recognized as wedge shaped units that show aggradational to progradational stacking patterns and downlap onto the hangingwall (Gawthorpe and Leeder, 2000, Folkestad et al., 2014). The Middle-Late Jurassic syn-rift infill has an overall upward fining trend from the sand-prone Tarbert Formation through the mud-prone Heather Formation to the clay-prone Draupne Formation. The fining-upward pattern reflects an overall deepening trend of the rift-basin. During the Bathonian to the Volgain the extensional rate varied and caused a strong tectonic control on the depositional infill patterns. The syn-rift deposit is related to a single stretching episode that lasted for approximately 30 Myr, and can be subdivided into infill related to distinct rift-phases lasting around 4-6 Myr. The distinct rift-phases sometimes involved a series of rotational tilt events, and the infill can further be subdivided into several smaller-scale units corresponding to these rotational tilt events lasting around 1-2 Myr. (Færseth and Ravnås, 1998).

2.2.2.2 Post-rift

During the Early Cretaceous the sea level rose and the syn-rift topography was overlain and truncated by transgressive sediments which formed the so-called Base Cretaceous Unconformity (BCU)(Coward et al., 2003), and the post-rift unconformity was onlaped by Cretaceous sequences (Badley et al., 1984). Post-rift deposits are characterized by tabular parallel units that onlap onto the footwall (Prosser, 1993, Folkestad et al., 2014). Calcareous mud-dominated Crommer Knoll Group were deposited on the clay-prone Draupne Formation during the Early Cretaceous. However in the Campanian-Maastrichtian time, mass movements of chalk and mud from the Hardråde Formation in the Shetland Group eroded the topographic highs area of the Oseberg fault block (Færseth and Ravnås, 1998, Deegan and Scull, 1977, NPD, 2015). The Shetland Group has through Paleocene been overlain by mudstones, marls or sandstones of the Rogland Group (Isaksen and Tonstad, 1989).

3. Theoretical background

In this chapter the terminology and theory of the observed deformation structures will be presented. Deformation bands will be emphasized and their relation to other deformation structures discussed. Previous work in carbonate rocks will be reviewed, and petrophysical properties to the deformation structures will be discussed.

3.1 Introduction

Extensional fractures, stylolites and slip surfaces (shear fractures) are known to be developed within low-porosity rocks. In porous granular rocks, on the other hand, grain translation and rotation, grain fracturing, pore volume change and pressure solution are fundamental micromechanical processes that define the failure modes and their structural results under upper crustal conditions (Aydin et al., 2006).

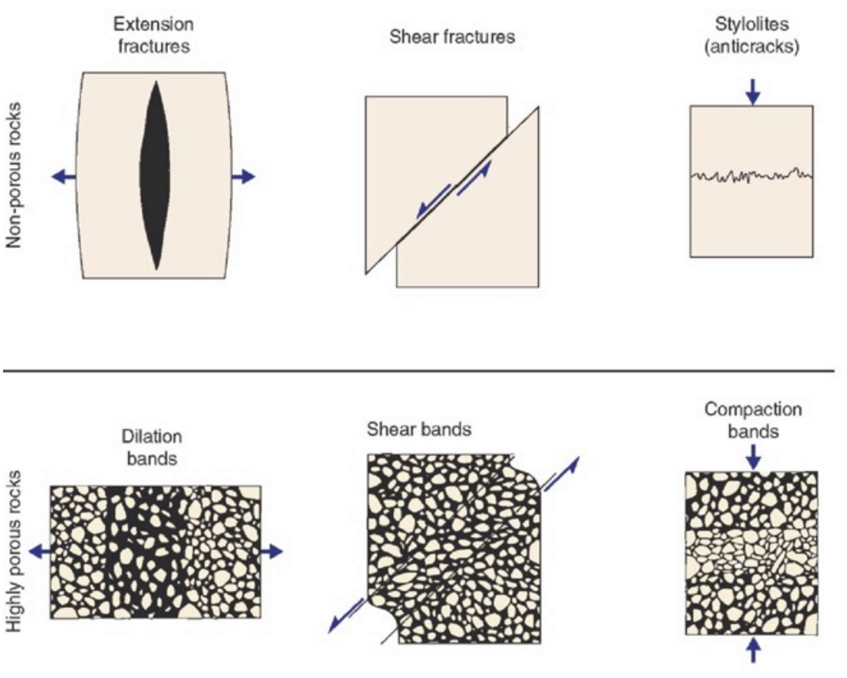

Figure 3.1: Kinematic classification of fractures in low-porosity rocks and their relation to deformation bands in high-porous rocks. Modified from Fossen (2010).

The process of deformation band development requires a certain amount of porosity, in sandstone commonly with porosity over c.15%, to allow grain translation and rotation (Fig. 3.1). Deformation bands can develop due to processes such as i) grain crushing, ii) reorientation of grains, iii) solution and cementation, iv) phyllosilicate smearing and v) dilation. Most of the deformation bands described in the geological literature are compactional shear bands developed by grain reorganization and cataclasis. This results in strain hardening within the bands, while strain softening is the behaviour developing fractures. Cohesion is therefore reduced across fractures, whereas deformation bands mainly maintain or increase cohesion. (Fossen et al., 2007, Aydin et al., 2006). Stylolites are often associated with fracturing structures and occur primarily during chemical compaction after the initial stage of mechanical compaction has reduced the pore space to the rock volume (Flügel, 2004). In addition, porosity and permeability are reduced in stylolites (Tondi, 2007, Fossen et al., 2007) and deformation bands, whereas permeability is increased in fractures and that might influence fluid flow substantially (Fossen et al., 2007).

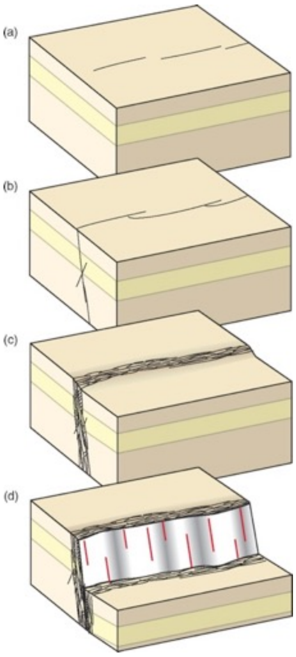

Figure 3.2: Model for illustrating the steps in the formation of a fault in a porous granular rock. a) An array of individual deformation bands, b) linking of the deformation structures, c) the formation of a deformation band zone, and d) the development of a slip surface and displacement of the zone. From Fossen (2010).

When strain accumulate and deformation bands develops in zones, strain hardening occur and the rock becomes more cohesive. When the rock is more cohesive the deformation will begin to favour growth of fractures rather than deformation bands. Microfracture arrays will eventually linking to form continuous slip surfaces and the formation of faults (Fig. 3.2). Once a slip surface has formed, strain localizes on it by frictional sliding (Fossen et al., 2007). The fault anatomy could be simplified and subdivided into a central fault core, a damage zone and a drag zone. The central fault core is where the slip surface occurs surrounded by a damage zone of brittle deformation structures such as deformation bands and smaller fractures, further surrounded by a drag zone comprising of ductile deformation of the host rock (Fossen, 2010). The damage zone is normally characterized by a steep increase in the frequency of deformation band towards a fault surface (Soliva et al., 2016, Schueller et al., 2013, Shipton and Cowie, 2003)

3.2 Fracture

3.2.1 Introduction

In the upper crust the typically deformation is of brittle structures such as fractures, forming in areas where stress has exceeded the local rupture strength in the crust (Fossen, 2010). Whereas stylolites is of ductile deformation and are less understood, they are important features in deformation and compaction of porous sedimentary rocks particularly in carbonates (Fletcher and Pollard, 1981).

3.2.2 Classification

Kinematically fracture or sharp discontinuities can be classified in slip surfaces (shearing), extensional fracture (dilation) and stylolites (pressure solution) (Fig. 3.1) (Aydin et al., 2006).

SlipsSurfaces or shear fractures are planar structures defined by two surfaces in contact and exposed to shearing (Pollard and Segall, 1987, Aydin et al., 2006). A continuous slip surface can construct the core in a fault and is an essential part of the fault anatomy (Fossen et al., 2007).

Extensional fractures or tension fractures are identified by dilational displacement normal to the two surfaces that define them (Aydin et al., 2006). Precipitation from fluids often occur in extension fractures, when they are completely filled with cement to become veins (Bons et al., 2012).

Stylolites or anti-cracks originate as a zone of stress concentration that propagate through the rock by pressure solution (Fletcher and Pollard, 1981). They are compactional structures characterized by their very irregular zone constituted by insoluble and immobile residue from the host rock (Fossen, 2010, Schultz and Fossen, 2008). Stylolites can be subdivided into bedding parallel and tectonic (or transverse) stylolites, depending on the orientation to the maximum compressive stress (σ_1) relatively to the bedding (Passchier and Trouw, 1996). Isolated or swarm-like partings of a stylolite might occur and be called a solution or dissolution seam (Flügel, 2004)

3.2.3 Formation conditions

Natural deformation of granular rocks is always determined by pre-existing elements that may weaken or strengthen the rocks matrix and influence the formation of deformation structures. Since deformation structures tend to develop across pre-existing weaknesses such as sedimentary structures from deposition or inherited structures from earlier deformation events (Aydin et al., 2006).

Microfractures and joints are prone to shear failure and can develop into slip surfaces (Segall and Pollard, 1983). In slip surfaces the mechanism of initiation appears to be slip along a pre-existing weak plane in response to shear stress along the plane (Aydin et al., 2006). The appearance of a slip surface marks the development of a fault in granular rocks. The slip surface in the fault core commonly consists of ultracataclasite (Shipton and Cowie, 2001, Aydin and Johnson, 1978), suggesting that grain crushing is a dominate mechanism in the formation of slip surfaces (Fossen et al., 2007).

Stylolites tend to form perpendicular to maximum compressive stress (σ_1). Bed-parallel stylolites are parallel to bedding, they are prone to being less serrate and thicker than tectonic styloltіes (Andrews and Railsback, 1997). Bed-parallel stylolites are considered to develop during diagenesis and long-time compression, by chemical compaction and can predate or postdate tectonic stylolites. Tectonic stylolites develops transverse to bedding, and the orientation change made by tectonic results in a shorter time of compression then by burial compression (Fig. 3.3). Even though both types of stylolites emerge from different orientation and time of compression, morphologically they grow by the same fundamental patterns (Andrews and Railsback, 1997, Railsback and Andrews, 1995, Bathurst, 1995, Aydin et al., 2006, Ebner et al., 2010). Stylolites have been reported to evolve with continuous pressure solution from microstylolites, to longer stylolites and to finally merge with neighbouring stylolites to form flaser residue seams and decrease in amplitude (Safaricz and Davison, 2005).

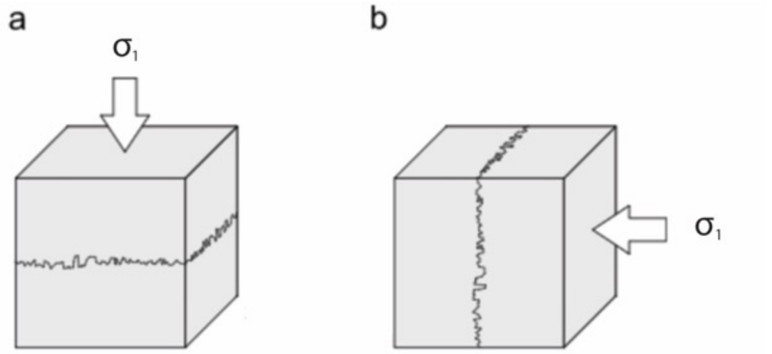

Figure 3.3: Schematic illustration of the formation stress state to a) bedding-parallel stylolites developed in response to burial stress and b) tectonic stylolites accommodating horizontal shortening. The white arrow indicates the orientation of the maximum compressive stress (σ_1). Modified from Ebner et al. (2010).

Pressure solution bears similarities to grain boundary diffusion, however the diffusion during pressure solution develop within a thin film of fluid along the grain boundaries. Therefore, in rocks that hold an intergranular fluid, pressure solution is a prominent deformation mechanism. Dissolution is significant where stress is high, mostly where grains are in contact along a surface perpendicular to σ_1, the minerals are dissolved and the ions are transferred with the fluid to be precipitated where stress is lower. This type of wet diffusion can occur at very low temperatures and is an important mechanism in the deformation of the plastic crust (Fossen, 2010, Passchier and Trouw, 1996). It is also a well-known factor that the occurrence of clay can promote the process of pressure dissolution in sedimentary rocks (De Boer, 1977, Aharonov and Katsman, 2009, Rustichelli et al., 2012).

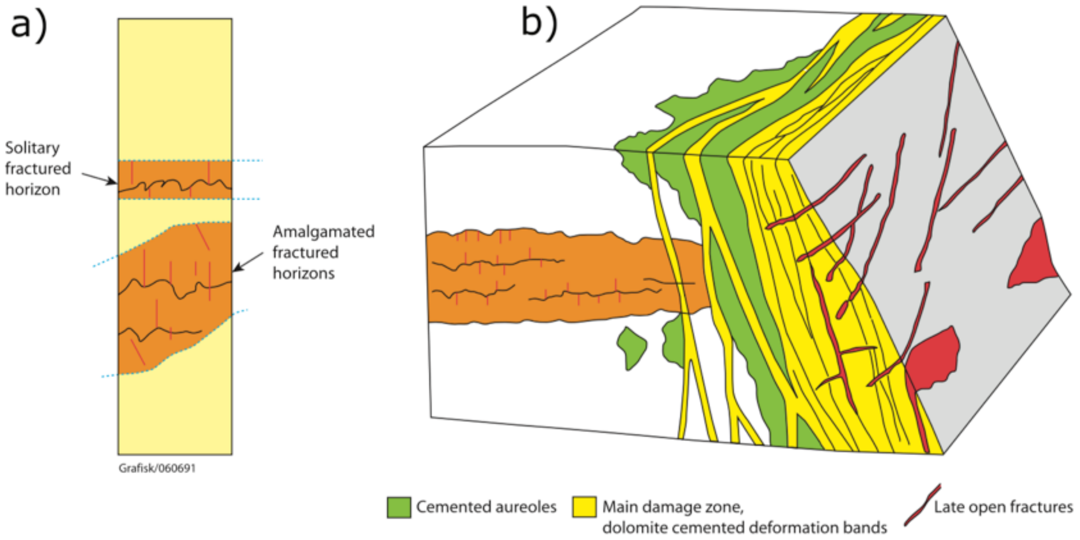

Figure 3.4: Schematic illustration showing a) the occurrence of stylolites and tensional fractures in layers, b) the distribution of stylolites and they related tensional fractures in a fault damage zone. From Wennberg et al. (2008)

Fractures could also form during stylolite formation, as tension fractures or veins. The tension fractures occur perpendicular to the bedding and terminates against the stylolite at one side and into the host rock on the other side. The stylolite-related fractures are mainly short and have their maximum aperture close to the stylolite. Such fractures have been interpreted to occur during burial because cementation made the rock cohesive, then removal of the overburden resulted in thermal contraction which enlarged the tensile stresses (Fig. 3.4) (Wennberg et al., 2008, Perez and Boles, 2005).

3.2.4 Fractures related to stylolite formation in chalk

Ekofisk Field is a well-known naturally fractured chalk reservoir in the central North Sea, consisting of the Maastrichtian Tor and Danian Ekofisk Formations (Byrd, 1975, Surlyk et al., 2003). Whereas extensional fractures are common in the chalk of the Ekofisk Formation, stylolite-associated fractures dominante in the chalk of the Tor Formation (Agarwal et al., 1997). The stylolite-associated fractures can be upto 15 cm long and occure with a density of 1 fracture per 5 cm, they are interpreted as extensional fractures related to the dissolution of the chalk by the formation of stylolites (Surlyk et al., 2003). Stylolite-related fractures has been reported in chalk (Lind, 1993, Toublanc et al., 2005, Feazel, 1988). According to Lind (1993) and Fabricius (2007), stylolites in chalk becomes prominent at depths larger than 800

m. Lind (1993) also suggest that the abundance of stylolites, with lower frequency, however larger amplitude is a function of depth.

Dark brown and white tabular narrow lines with single or anastomosing pattern observed in chalk, has been classified as healed fractures or hairline fractures(Agarwal et al., 1997, Surlyk et al., 2003, Toublanc et al., 2005). Healed fractures are thought to be the first fracture type developing in the chalks, and they are found exclusively in intervals of redeposited chalk (Feazel, 1988). The brown fractures are interpreted as more oil-saturated then the white lines, both appears however to comprise less porosity than the host rock. Observed in the microscope and SEM, the healed fractures show reduction in pore size and porosity. They have been interpreted to evolve by comminution and shearing while the sediments where partially lithified, and healed by diagenetic dissolution and precipitation. The oil staining has been interpreted to be indications of fluid flows of hydrocarbons before the diagenetic event (Feazel, 1988, Agarwal et al., 1997)

These definitions on the hairline fractures are, however, vague, and there has been challenges to observe their microstructural features due to the chalk comprises og very fine grained deposits of broken coccoliths (Wennberg et al., 2013). Some also argue that the "hairline fractures" could potentially be pressure solution seams (Rustichelli et al., 2012, Fletcher and Pollard, 1981). Pressure solution seams has previously been described in the North Sea Chalk to have similarities to stylolites (Safaricz and Davison, 2005). Formation of stylolite in chalk has been reported to mainly be controlled by effective stress (rather than temperatures), total stress or burial depth (Fabricius, 2007). Wennberg et al. (2013), argue that from observation from SEM images that there neither are indications of major pressure solution inside the features, nor any traces of insoluble material which generally accumulate in pressure solution seams.

3.2.5 Petrophysical properties

Extension fractures are known to have significant effect on the fluid flow in hydrocarbon production in the chalk fields of the North Sea, such as controlling the permeability distribution and enhancing permeability (Toublanc et al., 2005, Nelson, 1981). Stylolite-related fractures are also considered to control the permeability, however not as substantial as extension fractures (Toublanc et al., 2005).

In sandstones the quartz dissolution and cementation starts at temperature about 70°C, and increases gradually until 120°C. Above 120 °C, quartz cementation is rapid, leading to an accelerated loss in porosity and permeability in extensional fractures (Walderhaug, 1996). Extensional fractures formed in sandstones at large depths where temperature exceeds 120 °C are therefore unlikely to retain with high permeability over geological time (Wennberg et al., 2008). Whereas chalk undergoes dissolution and cementation at an effective stress of about 5-10 MPa (Fabricius, 2007) or at burial depths > 300 m (Flügel, 2004). Cementation will stiffen the chalk and the rock becomes more prone to tensile failure.

3.3 Deformation bands

3.3.1 Introduction

Deformation bands have been reported in both upper-crustal tectonic and non-tectonic settings. That includes glaciotectonic settings (Hooke and Iverson, 1995), thrust and reverse faults (Cashman and Cashman, 2000), contractional regime (Fossen et al., 2015) and most commonly in extensional regimes (Fisher and Knipe, 2001).

Deformation bands are deformation structures resulting from failure and made by strain localization or volume change in highly porous rocks and sediments (Aydin, 1978, Aydin and Johnson, 1978), through grain reorientation (disaggregation), grain fragmentation (cataclasis), dissolution (pressure solution) and precipitation (cementation) (Fossen et al., 2007). They are millimetre to centimetre thick, narrow tabular zones that can vary in thickness and properties along the band (Aydin et al., 2006). A band can be subdivided into an inner part bounded on both sides by a transition zone where the pore volume is more than within the band and less than the host rock (Antonellini and Aydin, 1994). The bands can appear as individual bands, zones of bands, linked and complex zones of numerous bands or as faulted deformation bands associated with slip surfaces (Fossen et al., 2007, Soliva et al., 2016). The occurrence of shear enhanced deformation bands within a fault damage zone can appear in conjugate sets, where one set is subparallel to the slip surface and the other set is dipping in the opposite direction (Fossen et al., 2005, Antonellini et al., 1994).

As previously mentioned, faults in a granular rock can be generated by propagation of deformation bands. When the rock is subjected to stress, individual deformation bands develops and propagates into cluster of zones comprising several deformation bands. Propagation of these structures can cause strain hardening and result in brittle failure of the deformation band zones developing a slip surface, which generates a faults (Aydin et al., 2006, Fossen et al., 2007, Aydin and Johnson, 1978, Rotevatn et al., 2007). Although a slip surfaces does not represent a deformation band, slip surfaces form by failure of deformation band zones and serve as a more mature stage in the development of faults (Fossen et al., 2007). Deformation bands do not generate great offsets. Even when the bands themselves are 100 m long the offsets are not greater than a few centimetres (Antonellini et al., 1994, Fossen and Hesthammer, 1997). This, among other things, distinguishes deformation bands from faults, where faults host a higher offset (Fossen et al., 2007).

3.3.2 Classification

Deformation bands can be classified by kinematics or by their dominant deformation mechanism. Kinematically, deformation bands may exhibit compaction, shear, dilation or a combination of these (Aydin et al., 2006). This forms the basis for a kinematics-based terminology that is shown in Fig. 3.5; the different types of bands according to this classification scheme are presented in the following.

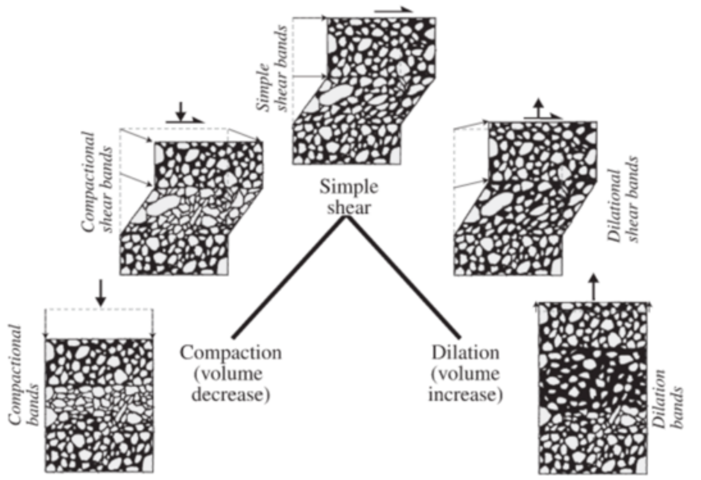

Figure 3.5: Kinematic classification, proposed from Aydin et al. (2006). From Fossen et al. (2007). The arrows indicate the translation of stress.

Compaction bands (Fig. 3.5) are bands that involve volumetric deformation in form of a volume loss, or compaction resulting in a decrease in porosity with respect to the host rock (Aydin et al., 2006, Fossen et al., 2007). They form as anti-cracks under elastic loading using linear elastic fracture mechanics (Sternlof and Pollard, 2001). Pure compaction bands seems to be limited to granular rocks with a porosity of 30% or higher (Fossen et al., 2015, Tondi et al., 2006). These bands exhibit no shear offset. Compaction may be achieved by means of grain reorganization, grain crushing (cataclasis) or dissolution.

Dilation bands (Fig. 3.5) are bands that are characterized by volume gain, or dilation, resulting in an increase in porosity with respect to the host rock, and show no shear offset (Du Bernard et al., 2002, Aydin et al., 2006). The increase in pore space is accomplished primarily through granular flow mechanism in the form of disaggregation (Fossen et al., 2007).

Simple shear bands, or isochoric shear bands (Fig. 3.5) are bands that exhibit shear offsets, which involve no volume gain or loss (Aydin, 1978, Antonellini and Aydin, 1994, Aydin et al., 2006). Perfectly isochoric shear bands are rare in nature, however deformation bands exhibiting kinematics close to simple shear, with minor compactional components, have been reported (Rotevatn et al., 2008).

Shear bands occur commonly as *compactive shear bands* (Fig. 3.5), which are bands that involve shearing combined with pore volume decrease. They are recognized in the field by being more resistant to weathering than the host rock and having noticeable shear displacement parallel to the band (Aydin et al., 2006, Aydin and Johnson, 1978, Aydin, 1978, Antonellini and Aydin, 1994).

Several deformation mechanisms may be at play to accommodate strain within deformation bands, depending on a range of external and internal conditions during deformation, such as stress state, porosity, cementation, grain size, shape, sorting and mineralogy. Classification by dominant deformation mechanism (Fig. 3.6) classifies bands depending on the different properties of deformation mechanism such as; granular flow, cataclasis, phyllosilicate smearing, and solution and cementation (Fossen et al., 2007). This is usually combined with the kinematic classification (Fig. 3.5) to specify and describe the deformation mechanism.

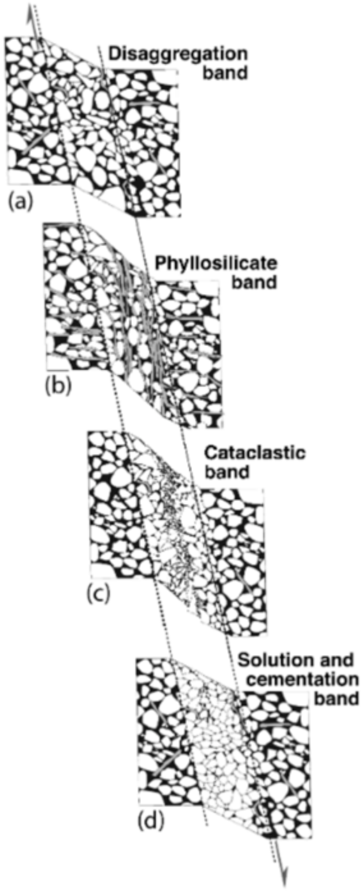

Figure 3.6: Classification based on dominant deformation mechanism. a) Disaggregation band and granular flow, b) phyllosilicate band with phyllosilicate smearing, c) cataclastic band and d) solution and cementation band. From Fossen et al. (2007).

Disaggregation bands (Fig. 3.6) are bands developed by disaggregation of grains, non-cataclastic rigid grain rolling by granular flow mechanisms (Fig. 3.7) (Twiss and Moores, 1992). They are commonly found in poorly consolidated sandstones (Du Bernard et al., 2002), and in sediments that has undergone soft-sediment deformation such as slumping (Twiss and Moores, 1992). Disaggregation of grains is typically the earliest stage when deformation bands develops. In the field they are almost invisible, however they can be identified where they cross and offset sedimentary structures such as laminae (Fossen et al., 2007). The amount of shear and compaction depends on the properties of the rock. Some compacted sandstones have been documented to show dilation as the initial stage before shearing and cataclasis (Antonellini and Pollard, 1995, Lothe et al., 2002).

Phyllosilicate bands (Fig. 3.6) are a special type of disaggregation bands that develop in porous rocks where the content of phyllosilicate minerals, such as clay, comprise between 10-40% (Knipe et al., 1997). Similar to disaggregation bands, the phyllosilicate bands develop by non-cataclastic granular flow where the platy minerals promote frictional grain boundary sliding instead of grain fracturing (Fig. 3.7) (Fossen et al., 2007). The bands are fine-grained, with clay smearing and low porosity (Antonellini et al., 1994). If the clay content in the smear is higher than 40 %, than the structure becomes a continuous zone of clay and is called a clay smear (Fisher and Knipe, 2001). Striations have been observed on many clay smearing surfaces, indicating that they act as slip surfaces rather than as deformation bands (Johansen and Fossen, 2008). The platy minerals are rotated into parallelism within the band, and due to the smearing, phyllosilicate bands are the deformation bands that can gain the most offsets. With their unique dark colour and aligned fabric due to the clay minerals, they are easily detected (Fossen et al., 2007).

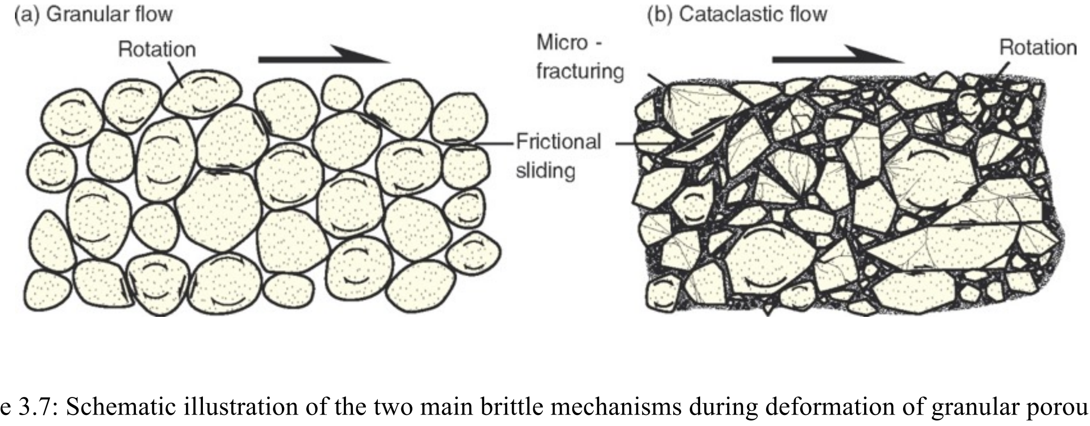

Figure 3.7: Schematic illustration of the two main brittle mechanisms during deformation of granular porous rocks, a) granular flow, b) cataclastic flow. From Fossen (2010).

Cataclastic bands (Fig. 3.6) are generally shear-related bands developed by cataclastis, i.e. fracturing, flanking and crushing of grains (Fig 3.7) (Aydin et al., 2006, Fossen et al., 2007, Borg et al., 1960). When the rock is subjected to stress and the stresses at grain contacts surpasses the tensile strength to the grains or the rock in general, the grains breaks and fragments to smaller angular grains (Aydin et al., 2006). In addition, rocks tend to weaken under high pore fluid pressure rocks (Hubbert and Rubey, 1959) and the rock is then more prone to cataclastis. The cataclastic grain crushing leads to high angularity, promoting grain interlocking and high frictional resistance, thus leading to strain hardening of the bands (Aydin, 1978). This strain hardening behaviour is responsible for the fact that cataclastic bands develop smaller displacement compared to disaggregation bands of similar lengths (Fossen et al., 2007). The core of the band consists of poorly sorted angular grains. The porosity is reduced within the core, respectively to the host rock that can show some compaction due to granular flow by the burial compression (Fossen et al., 2007).

Solution and cementation bands (Fig. 3.6) are bands that showing evidence of pressure solution or/and cementation coating around grains by diagenetic minerals (Fossen et al., 2007, Gibson, 1998). Cementation bands are promoted where there has occurred a fresh and cataclastic surface. Solution and cementation bands typically consist of tightly packed and sutured grains that are smaller in size than the matrix (Fossen et al., 2007) and common in carbonate rocks (Tondi et al., 2006, Cilona et al., 2012). Solution compaction bands can occur during chemical compaction and show similarities to stylolites, hence they are kinematically comparable (Tondi et al., 2006, Flügel, 2004).

3.3.3 Conditions favouring formation of deformation bands

A number of factors are important regarding formation conditions of deformation bands, such as deviatoric stress (tectonic environment), confining pressure (burial depth), pore fluid pressure and host rock properties, such as sorting, grain size, grain shape, mineralogy and degree of lithification. Factors such as stress state, confining pressure, cementation, permeability and porosity might change with time. Deformation structures reflects physical changes during burial, lithification and uplift and are therefore important as geological signatures to recognize these changes (Fossen et al., 2007).

Disaggregation bands form at low confining pressure and are therefore the earliest forming bands in sandstones (Fig. 3.8), whereas phyllosilicate bands may form at different depths as long as c.15% or more phyllosilicates are present (Fossen et al., 2007). Commonly, cataclastic bands are observed in rocks that has been buried to depths of >1 km. It is therefore assumed that cataclastic bands develop at depths with higher confining pressure than disaggregation bands (Fig. 3.8) (Fossen et al., 2007), hence shallow cataclastic bands can develop in poorly consolidated sand where well-rounded and well-sorted grains lead to high grain contact stress (Cashman and Cashman, 2000, Lucas and Moore, 1986, Karig and Lundberg, 1990, Ujiie et al., 2004). The intensity of cataclasis will afterwards increase with depth (Fossen et al., 2007). It has been observed that when a cataclastic bands enter a more fine-grained and poorly sorted sandstone, the bands changes into a disaggregation bands. This indicates that porosity, mineralogy and grain size are influential factors (Schultz and Fossen, 2002).

Dissolution or cementation can occur along a deformation band during its formation, or after the deformation (Fossen et al., 2007). As already mentioned in section 3.3.5, quartz dissolution and cementation starts at temperature about 70°C, and increases gradually until 120°C (Walderhaug, 1996). Whereas calcite reaches dissolution and cementation at an effective stress of about 5-10 MPa (Fabricius, 2007) or at burial depths > 300 m (Flügel, 2004). Generally, dissolution is dependent on the pressure generated during burial by the overburden and is more abundant in carbonate rocks due to the dissolution at shallower depths than for sandstones (Flügel, 2004, Fabricius, 2007).

When porosity is reduced and the rock is subjected to strain hardening by the development of deformation bands, the rock becomes cohesive, and deformation tend to propagate by fracturing rather than collapse in pore space. Deformation bands therefore tends to predate fractures (Fig. 3.8) (Fossen et al., 2007, Johansen et al., 2005). As already mentioned, it has been reported that with increasing strain, the number of deformation bands increases (Mair et al., 2000). Notably, deformation bands tend to accumulate in the damage zone to the fault, and it has been documented that larger fault tend to have wider damage zones than smaller faults (Shipton and Cowie, 2003).

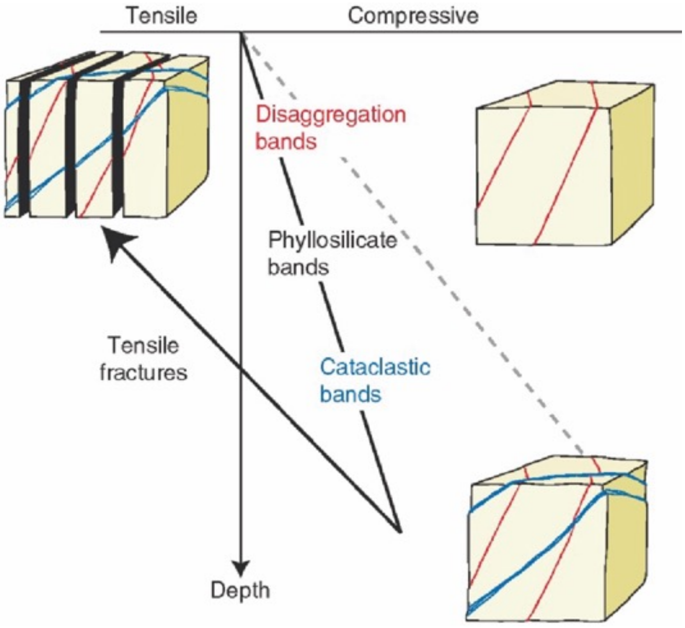

Figure 3.8: Schematic illustration of the formation of different types of deformation bands during burial, and how tensile or extension fractures form during uplift. Modified from Fossen (2010).

3.3.4 Deformation bands in carbonate rocks in general and chalk specifically

As mentioned in section 1.1, deformation bands in porous carbonate rocks was first reported in laboratory experiments (Baud et al., 2000, Vajdova et al., 2004). Then in 2006 natural occurrence of these bands was reported (Marchegiani et al., 2006, Micarelli et al., 2006, Tondi et al., 2006). Since then, deformation bands in carbonate grainstones have been documented in the field (Tondi, 2007, Agosta et al., 2010, Antonellini et al., 2008, Cilona et al., 2012, Rustichelli et al., 2012, Tondi et al., 2012, Antonellini et al., 2014b, Rotevatn et al., in press), and recently also in chalk (Wennberg et al., 2013, Kaminskaite et al., 2015, Gaviglio et al., 2009).

Many similarities have been reported between deformation bands in carbonate rocks compared to its counterparts in sandstone. This includes i) strain hardening behaviour (Cilona et al., 2012), ii) porosity and permeability reduction (Rotevatn et al., in press , Antonellini et al., 2014a), iii) granular flow (Tondi et al., 2006), iv) cataclasis (Rustichelli et al., 2012, Rotevatn et al., in press).

However there are some differences: whereas the main mechanism for formation of deformation bands in porous sandstone is disaggregation and cataclasis (Antonellini et al., 1994, Fossen et al., 2007), solution and cementation (pressure solution) appears to play an important role in compaction and shear deformation at shallower depths in carbonate rocks (Tondi et al., 2006, Cilona et al., 2012, Tondi et al., 2012, Rotevatn et al., in press). Therefore in carbonate rocks the main deformation mechanism has been reported to be pressure solution and disaggregation, cataclastic may also occur (Tondi et al., 2006, Cilona et al., 2012, Antonellini et al., 2014b, Rustichelli et al., 2012, Rotevatn et al., in press). There has been documented non-cataclastic and cataclastic deformation bands in porous carbonate rocks where proof for pressure solution processes are absent (Rath et al., 2011). It appears to be common in carbonate rocks that deformation by brittle cataclasis occurs at shallow burial depths (Micarelli et al., 2006, Antonellini et al., 2014a, Tondi et al., 2012). Antonellini et al. (2014b) reports soft plastic deformation and subsequent smearing of peloids in soft micrite as a micromechanism of deformation in carbonate rocks. The plastic smearing is interpreted to develop due to the intragranular microporosity present in the peloids (Antonellini et al., 2014b).

Previously it has only been reported pure compaction bands related to i) burial compaction ii) contraction (Fossen et al., 2011). Rotevatn et al. (in press), reports a tectonic control on pure compaction bands in carbonate rocks in extensional setting. Tondi et al. 2006 argue that pressure solution and subsequent shearing of stylolites grain size reduction is achieved in compactive shear bands. Band-parallel stylolites has been suggested to promote discrete shear localization in carbonate rocks (Tondi, 2007). Rotevatn et al. (in press), found compactive shear bands without evidence of stylolite shearing being responsible for brittle grain size reduction through cataclasis. Instead, the bands exhibit brittle cataclasis similar to the process seen in deformation bands in sandstone (Antonellini et al., 1994).

Cilona et al. (2012), argue that in contractional settings, shearing within deformation bands in carbonates might develop without significant grain crushing, and that the deformation exhibit a more ductile behaviour than seen in experiments due to pressure solution. However, Rotevatn et al. (in press) argue that the pressure solution mechanism is less important to facilitate cataclasis in an extensional tectonic setting. Pressure solution might be more abundant in contractional tectonic settings, where it can develop by burial compression (Rotevatn et al., in press). Stylolites has been observed within previously formed deformation bands in carbonates, and Tondi et al. (2006) argue this transition between mechanical behaviour of deformation band processes to pressure solution to be possible since they are kinematically compatible. Other isolate stylolites in the same study, showed deflection when they crossed pre-existing deformation bands. The stylolites became subparallel to the band for a short distance before diverging and and resuming their original orientation (Tondi et al., 2006).

Kaminskaite et al. (2015) analysed deformation bands found in the chalk from Pegwell Bay in Kent. The CT-scans indicated decrease in porosity within the bands compared to the host rock, however the permeability did not show any significant change. It was suggested that the microstructural analysis showed reduction in porosity due to collapse of fossils, which contained macro-intraporosity within the spherical fossil chambers and this porosity were not connected. However, the samples containing deformation bands seemed to have smaller pore throats and higher threshold pressures than the samples of undeformed chalk (Kaminskaite et al., 2015). Gaviglio et al. (2009) argue that their findings of dissolution and cementation features composed with a reduction of pore space could be explained by massive fluid flows and that the faulting occurred by ductile shearing.

Wennberg et al. (2013) suggest that the deformation bands found in the Shetland Chalk in the Oseberg Field to have been formed as compactional shear bands during vertical compaction. The deformation bands terminates and are truncated by stylolites, indicating that these deformation bands are constrained by its relationship to the stylolites and predates the main phase of stylolitization (Wennberg et al., 2013)

3.3.5 Petrophysical properties

Disaggregation bands can show an increase or reduction in porosity within the band, depending on whether they contain dilational or compactional component. Pure dilational disaggregation bands represent an increase in porosity, however mostly this is only transient before the pore space is cemented or infilled by clay (Du Bernard et al., 2002). Compactional disaggregation bands show reduction in porosity, and a reduction of permeability up to 1 order of magnitude have been observed in sandstones containing phyllosilicates (Fisher and

Knipe, 2001). Usually the porosity and permeability contrasts are relatively low, and commonly diaggregation bands have little influence on the permeability of granular rocks (Fossen et al., 2007). Shear-dominated bands comprises a significantly lower permeability compared to compaction-dominated bands (Ballas et al., 2015). Phyllosilicate bands may reduce the permeability depending on the amount of phyllosilicate minerals, the type of phyllosilicate, the distribution of phyllosilicates, the displacement along the band and the grain size. The reduction in permeability is around 2 to 5 orders of magnitude compared to the host rock (Fisher and Knipe, 2001). Due to the grain crushing and change in grain size distribution, cataclastic bands can accommodate a reduction in porosity of 1 order of magnitude (Fisher and Knipe, 2001, Fossen et al., 2007). Permeability reduction in cataclastic bands has been reported to be in a range as wide as 1-6 order of magnitude, with most studies reporting 1-3 orders of magnitude permeability reduction (Fisher and Knipe, 2001, Antonellini and Aydin, 1994).

Cementation reduce the porosity and increase the cohesion of the rock, making it more prone to tensile failure and development of fractures (Fossen et al., 2007, Aydin et al., 2006). Deformation bands dominated by pressure solution and cataclasis in carbonate rocks, may have an reduction in permeability by 1-4 order of magnitude event at shallow burial depths (Rath et al., 2011, Antonellini et al., 2014a). In contrast, poorly consolidated sandstones at the same depth, the deformation is dominated by granular flow and the bands would have little influence on permeability (Fossen et al., 2007, Fisher and Knipe, 2001).

Regarding petrophysical properties for single-phase flow (i.e. oil flowing in oil-saturated rock, or water flowing in water-saturated rock) it is the permeability and thickness of the deformation band zone that controls the fluid flow (Darcy flow) (Matthäi et al., 1998, Walsh et al., 1998). For two-phased flow (i.e. oil flowing through water-saturated rock) it is the capillary pressure that becomes important. How much migration that occurs within a hydrocarbon reservoir sealed by a fault, is determent by the capillary threshold pressure of the fault rock (Fossen et al., 2007). It is predicted by calculations that deformation bands cannot hold much more than 20 m (Harper and Lundin, 1997) or a 75 m high column of hydrocarbons (Gibson, 1998). Therefore the continuity or variation in thickness and permeability in three dimensions in the deformation bands are critical. If the deformation bands have a preferred orientation they might influence and change the flow pattern and channelize the fluids in the host rock (Fossen et al., 2007). As previously mentioned, the deformation bands in a fault damage zone tend to orientate with one set being subparallel to the slip surface and the other set dipping the opposite direction (Fossen et al., 2005). Therefore it is expected that the fluids flow parallel to the strike of these conjugated bands (Fossen et al., 2007).

4. Methods

This chapter provides an overview of the data involved and the principles of the methods and instruments used in order to collect and analysed the data to this study.

4.1 Stratigraphic overview

109 m of core from the Hardråde/Jorsalfare Formation in the Shetland Group chalk were available for this study. The cores where taken from two wells: 30/9-B 44 B and 30/9-B 46 A. Both wells are deviated nearly 60° in the cored interval, see table 1.1 for details. The recovery of the cores in the two deviated wells are of good quality. The core description was conducted on the half-core or A-cut according to the Norwegian Petroleum Directorate standard for core preservation (Wennberg et al., 2013). The A-cut provides a surface through the centre of the core in addition to the outside of the half core.

When sampling a core out of a drilled well, induced fractures can occur dependent on the in situ stress state existing in the rock, prior to the drilling. They can occur perpendicular to the drilling orientation, with an angle to or subparallel to the direction of drilling (Li and Schmitt, 1998). This can also occur when taking out plug samples from the half-core, and have to be taken in to consideration when analysing fractures in the core.

4.2 Scanline

A scanline was collected along 4 m (3342-3346 m MD) of cores from well 30/9-B 46 A, restricted to the middle of the core to best represent the “hairline discontinuity” sets present. The scanline method involves laying out a line on the area of interest for measuring attributes such as frequency (features per measured length), orientation, length and spacing of the structures intersecting the line (Priest and Hudson, 1981). The scanline measurements where done by measuring the deformation structures visible on a line, and therefore limited by the area bisecting the line and to the resolution of the naked eye.

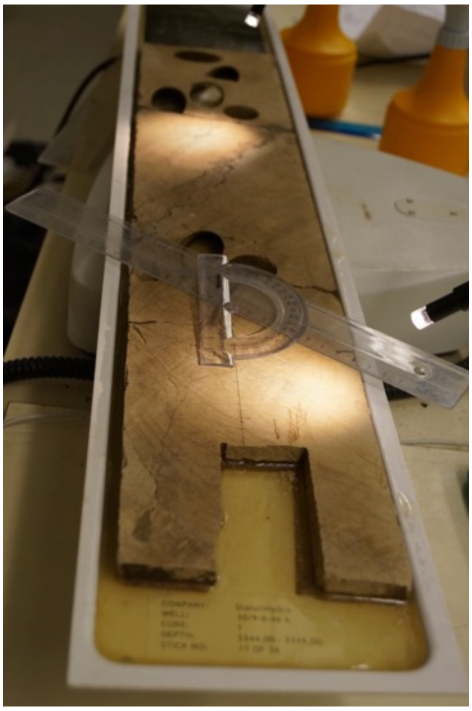

Figure 4.1: The set up for pursuing the scanline. A protractor was used to measure the dip of the deformation structures relative to the scanline along the core.

4.3 Microscopic analysis

It was given permission to take 15 plugs from the core in well 30/9-B-46 A, and one new thin section from each of the plugs where made. In total 23 thin section where used in this study, 22 from the core in well 30/9-B-46 A and 1 from the deepest core in well 30/9-B-44 B. Preparation of the thin section was done at Statoil in Bergen, where they were stained with blue epoxy and polished to a thickness of 30 μm using ultra fine aluminium oxide. The blue epoxy is stained on to enhance the imaging of 2D porosity by the blue colour compared to the grains of different colours. They were all prepared without coating for the use of scanning electron microscope (SEM) imaging as well as optical polarizing light microscope for microstructural analysing of the deformation structures, the host rock and the internal pore-system. When making a thin section, polish tools can leave straight polish marks on the surface to the thin section, they are visible in SE-SEM images, see Fig. 4.2 below.

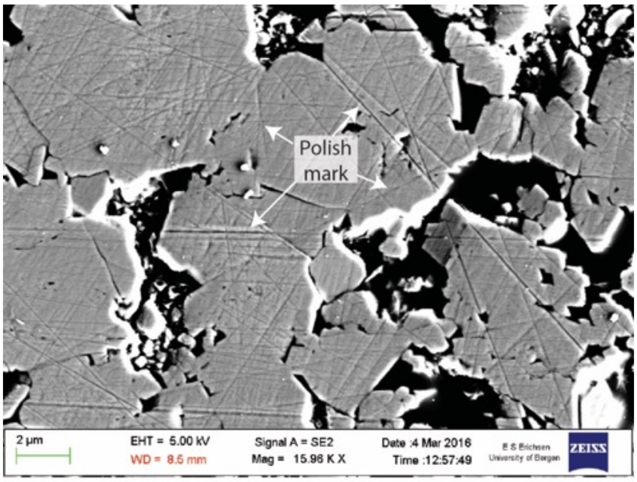

Figure 4.2: The lineation shown in the SE image are polish marks, indicated by the white arrows.

The lithofacies of the host rock have been determined according to Dunham (1962) and Folk (1962), based on the classification scheme for carbonate rocks (Fig. 4.3). Classification of carbonate rocks is based on the depositional texture and composition, such as the relative amount of matrix and grains. Nevertheless, this classification does not distinguish different types carbonate grains nor if the rock is heterogeneous.

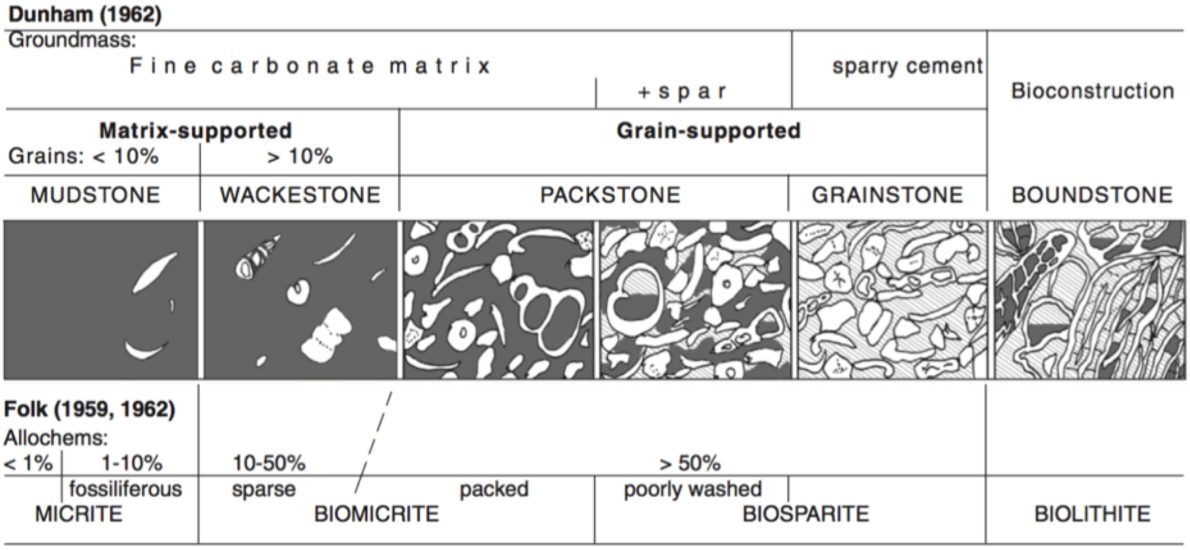

Figure 4.3: Dunham and Folk classification schemes of carbonate rocks, used to classify the host rock in the studied cores. From Flügel (2004).

The pore types within the chalk was determined by the classification on pore types by Choquette and Pray (1970). The pore type classification separates depositional or post-depositional controlled fabric (fabric-selective) and processes that bisects the fabric to the rock (non-fabric-selective) (Fig. 4.4) (Flügel, 2004).

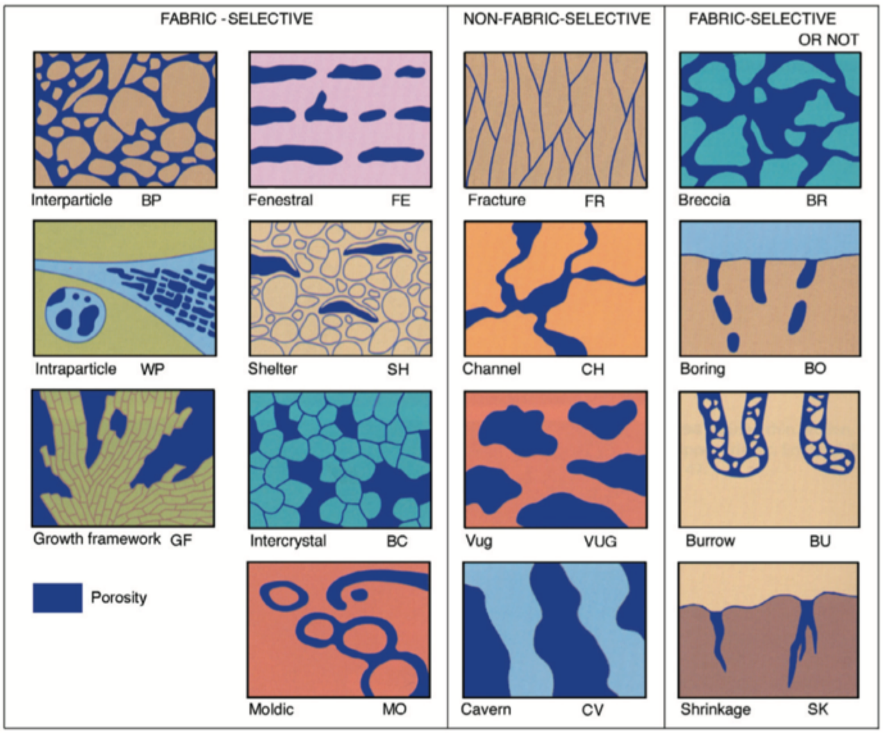

Figure 4.4: Choquett and Pray classification scheme of pore types within granular rocks. From Flügel (2004).

The different grain contacts observed in thin section can be used to indicate different stages of compaction of the rock. Point contact indicate initial compaction, tangential contacts increasing compaction and sutured and concavo-convex contacts point to effects of pressure solution at grain contacts (Fig. 4.5).

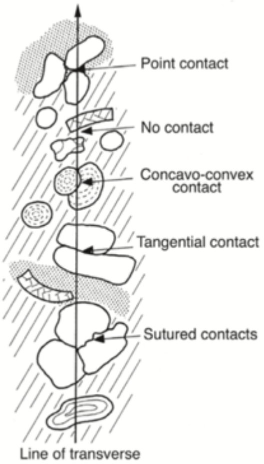

Figure 4.5: Schematic illustration of different grain contact types according to Taylor (1950). From Flügel (2004).

4.3.1 Light microscopy

A standard optical light microscope of the type Nikon Eclipse 400 POL were used together with a digital microscope camera, Nikon Digital Sight DS-U3, to take plane polarize light (PPL) microscopic images of the thin section at different magnifications (2X, 4X, 10X and 20X).

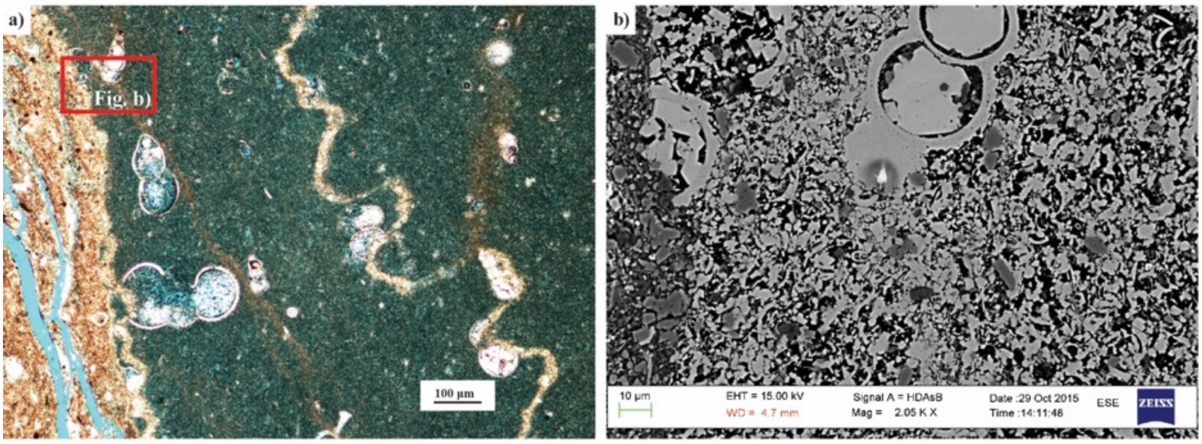

Figure 4.6. For comparison of a) PPL images 10X, indicating in the red polygon b) BSE-SEM image.

The grain and pore size of the undeformed coccolith matrix are typically 1-10 μm, which is less than the thickness of thin-section. This causes the cloudy and bluish appearance of the host rock, see Fig. 4.6. Standard optical microscopes are therefore not appropriate for estimation of porosity in fine-grained rocks, such as this chalk.

4.3.2 Scanning electron microscopy (SEM)

Scanning electron microscope (SEM) was used to improve the imaging of the deformation structures and to provide images for porosity estimation by image analysis. Backscattered electron (BSE) and secondary electron (SE) images were acquired using a ZEISS Supra 55VP Field Emission Scanning Electron Microscope.

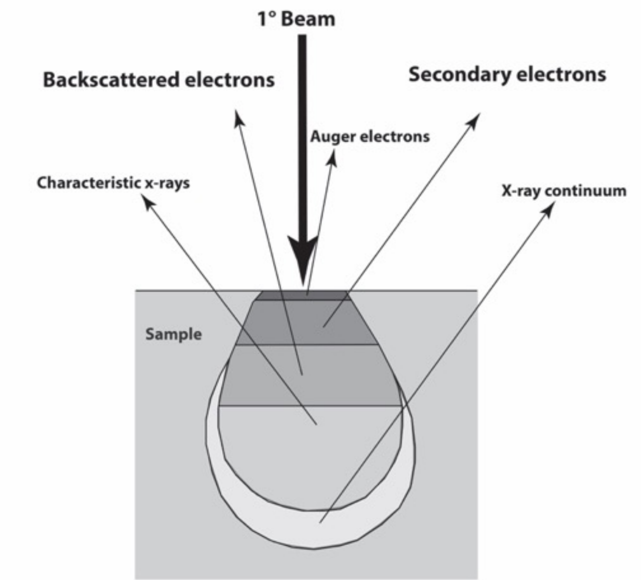

Figure 4.7 : Modified from Zhou et al. (2006). Illustration of several signals generated by the electron beam-specimen interaction in the scanning electron microscope and the regions from which the signals can be detected.

SEM produces images depending on the signals yielded from the interaction between the electron beam and the sample (Fig. 4.7). Backscattered electrons (BSE) are electrons that are elastically scattered through an angle of more than 90° after the beam electron collide with the sample, enduring negligible energy loss and escape from the sample surface with an energy greater than 50 eV. BSE provide both compositional and topographic information in the SEM. Elements with higher atomic numbers have more positive charges on the nucleus, as a result, more electrons are backscattered and causing the resulting backscattered signal to be higher. This will provide atomic number contrast in the SEM images. A BSE signal resolution of the surface is limited to 1.0 μm, however it has a relatively large width of escape depth and can transfer information about features that are deeper beneath the surface (Zhou et al., 2006).

Secondary electrons (SE) are created when the beam electron collides with the sample surface and causing ionization to the sample atoms loosely bound electrons which are then emitted as secondary electrons. SE are defined as having lower energy than BSE (< 50 eV), and can therefore only escape from an area within a few nanometers of the sample surface. The electrons are inelastically scattered back with a close angle to the beam, which gives a good resolution of the topography to the sample. SE signals can resolve surface topography down to the order for 10 nm or better, this highly dependents on the amount of the secondary electrons reaching the detector. For summary, SE image can have higher lateral resolution (10 nm) than BSE image (1.0 μm), while BSE image can transfer information deeper beneath the sample surface (Zhou et al., 2006).

Both SE and BSE signals can produce images, however there are also other signals produced when a beam electron collides with the sample, such as emission of characteristic x-rays. Characteristic x-rays can provide chemical information and can be used as an microanalytical technique to analyse the sample (Zhou et al., 2006).

4.4 Image-based porosity analysis

The software ImageJ 1.50r (Ferreira and Rasb, 2012) where used to do digital image analysis of SE-SEM images to quantify the 2D porosity. Image J 1.50r can calculate area and pixel values statistics for selected area within the image, and when calibrated it can measure distances in the image (Ferreira and Rasb, 2012). SE-SEM images were used since SE captured images can resolve surface topography better than BSE (as described in previous section 4.3.2), and giving the clearest view of the 2D porosity occurring at the surface of the thin section. For not missing any important pixel data, TIF format files of the SE-SEM images were used and converted to 8-bit greyscale image. The digital image analysis could then be pursuit by image segmentation, applied through manually editing the threshold area, separating the features of interest such as (in this case) the pore space from the grains (Fig. 4.8). The pixels within the threshold area, the red polygon, represent the pore space and are highlighted by red. When satisfied by the election of pore space with the threshold, the image is converted to a binary image where the pore space is indicated by black and the grains by the white colour. Counting the black pixels in the binary image permit measurements of the 2D porosity within the image.

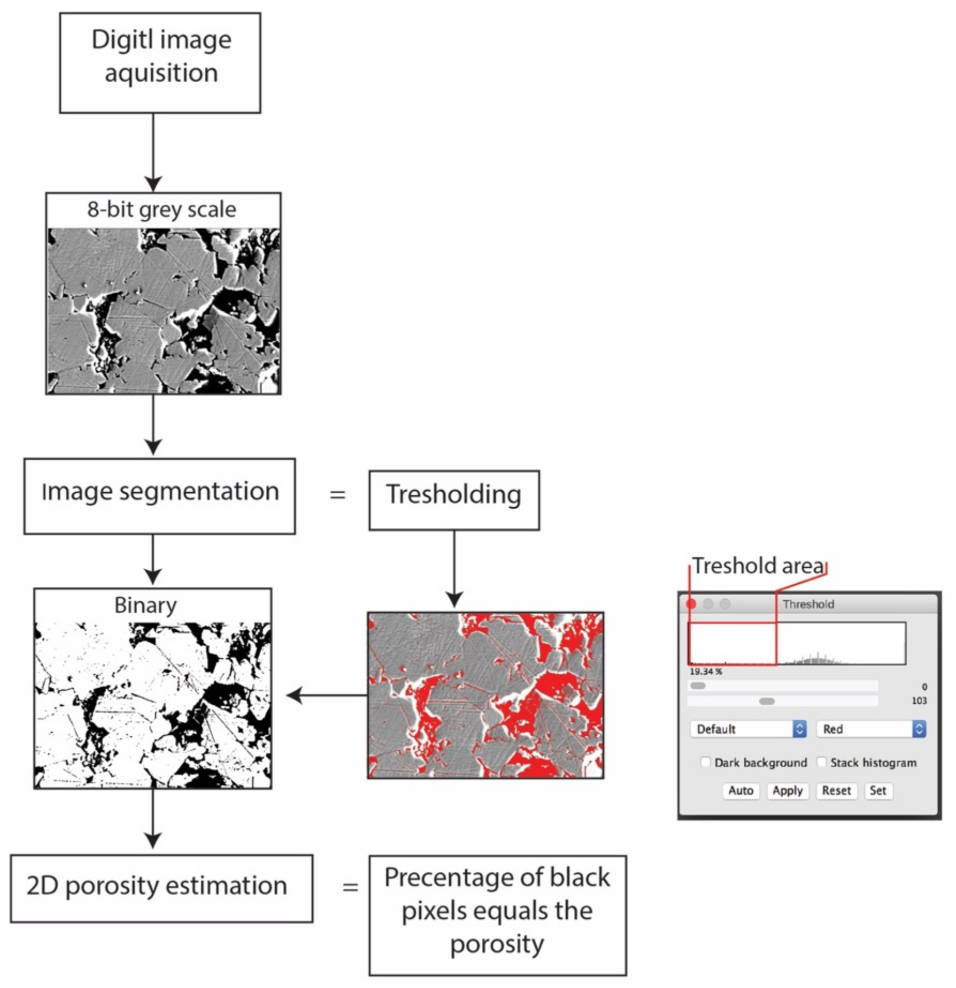

Figure 4.8: Schematic flow chart of the different steps in the 2D porosity estimation by the software ImageJ from a SE-SEM image. The percentage of black pixels in the binary image is the equivalent for the 2D microporosity measured.

With the use of this method it is assumed that the 2D porosity within the SE-SEM image is roughly the same as 3D porosity (Johansen et al., 2005). That would however only measure the porosity at the top of the thin section, which might not be the true porosity for the hole sample due to variations of grain organization in 3D. In addition, the threshold is predicted manually and human error by this prediction might occur as a complication.

5. Results

In this chapter the results of structural analysis of the cores will be presented, first qualitatively and quantitatively, then through microscopic analyses of the microstructures and porosity measurements.

5.1 Geology of the study area

5.1.1 Structural framework

The studied area is part of the Oseberg fault block located at the east flank of the Viking Graben in the North Sea (Fig. 5.1). The Oseberg fault block structure is bordered by the two main faults, the Brage fault to the east and the Oseberg fault towards the west (Færseth and Ravnås, 1998). The producing Oseberg Field is located in the fault block, with its main reservoir in the Middle Jurassic sandstone of Oseberg and Tarbert Formation (NPD, 2016b). The cores selected for this study are taken south of the Oseberg B facilitiy (Fig. 5.2), from the uppermost Shetland Group part of the Upper Cretaceous carbonates (Fig. 5.3). The two main faults bordering the Oseberg fault bock, offset the Jurassic syn-rift succession, while the Cretaceous carbonates postdates the Late Jurassic rift phase.

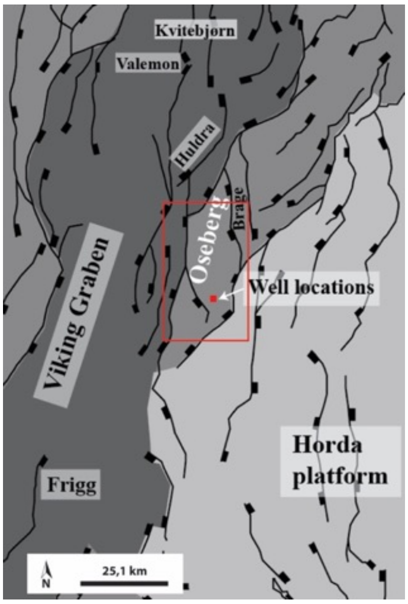

Figure 5.1: The study area is located in the Oseberg fault block and the well locations are indicated by the red square. Red polygon indicates the Oseberg fault block and Fig. 5.2.

The structural depth map, see Fig. 5.2, shows that the Cretaceous succession outlines an open anticlinal structure over the Oseberg fault block. This is thought to have been developed due to differential compaction of the Cretaceous marine shales deposited over the Oseberg fault block (Wennberg et al., 2013). Differential compaction can occur in basins where a sedimentary sequence is undergoes different degrees of compaction in different parts of the basin due to variation in thickness, e.g. over a fault scarp (e.g., Fossen, 2010).

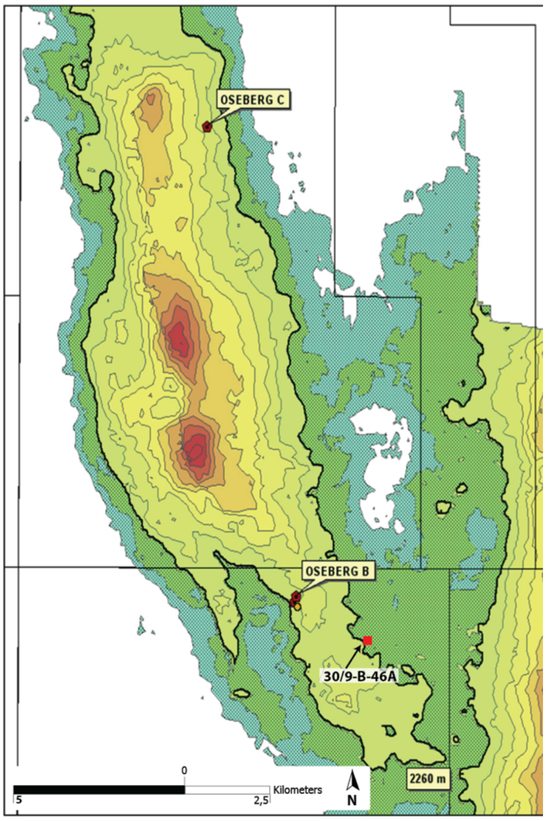

Figure 5.2: Structural depth map of the top Cretaceous over the Oseberg fault block, modified from Wennberg et al. (2013). The black contour line indicates 2260 m depth, and the red dot indicates the location of the well 30/9-B-46A. Contour interval are not included in this map due to confidentiality, however the outlined contour indicates that the light green is areas where the Cretaceous succession is thinnest and the dark red is where the succession is at its thickest. The area is outlined by the red polygon in Fig. 5.1.

When sediments are deposited and buried in a basin, the mechanical compaction by the weight of the overburden is the first process to deform the sediments by the pressure (Flügel, 2004). During differential compaction the degree of compactions will differ and be greatest where the sedimentary column is thickest and reduced where it is thinner. Therefore, this anticline of Cretaceous carbonates (Fig. 5.2) over the Oseberg Field area may have developed due to differential compaction. The Jurassic and Cretaceous successions must have undergone more compaction in the middle of the fault-controlled basin as compared to the successions pinching out towards the Oseberg fault scarp. Following mechanical compaction, sediments may be subjected to chemical compaction such as pressure solution (Flügel, 2004).

5.1.3 Stratigraphic framework

The cores used in this study are from well 30/9-B-44B and 30/9-B-46A composing the uppermost Shetland Group, of the interbedded limestones and mudstones of Hardråde and Jorsalfare Formation (see Fig. 5.3) (Isaksen and Tonstad, 1989). The studied area is located in a transitional area between a mudstone-dominated succession to the north and chalk-dominated successions to the south, deposited during a transgressive phase in the Upper Cretaceous time (Surlyk et al., 2003) (see section 2.1.1).

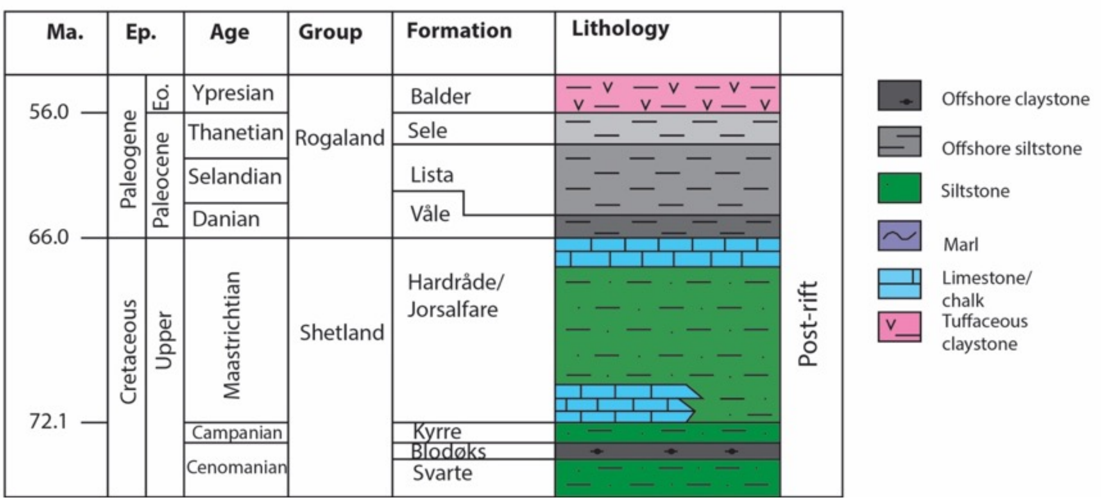

Figure 5.3: Stratigraphic diagram of the Cretaceous and Lower Paleogene of the Oseberg Field area. Modified from Isaksen and Tonstad (1989) and Wennberg et al. (2013).

5.2 General core description

5.2.1 Well core 30/9-B-44 B

Well 30/9-B-44B consist of two cores between 4242.00-4315.18 m MD (see Tab. 1.1). Six facies has been interpreted in these cores by GEUS (2011) (see section 1.3.2), where facies 4 is the major facies of shredded, intraclastic chalk (Fig. 5.4).

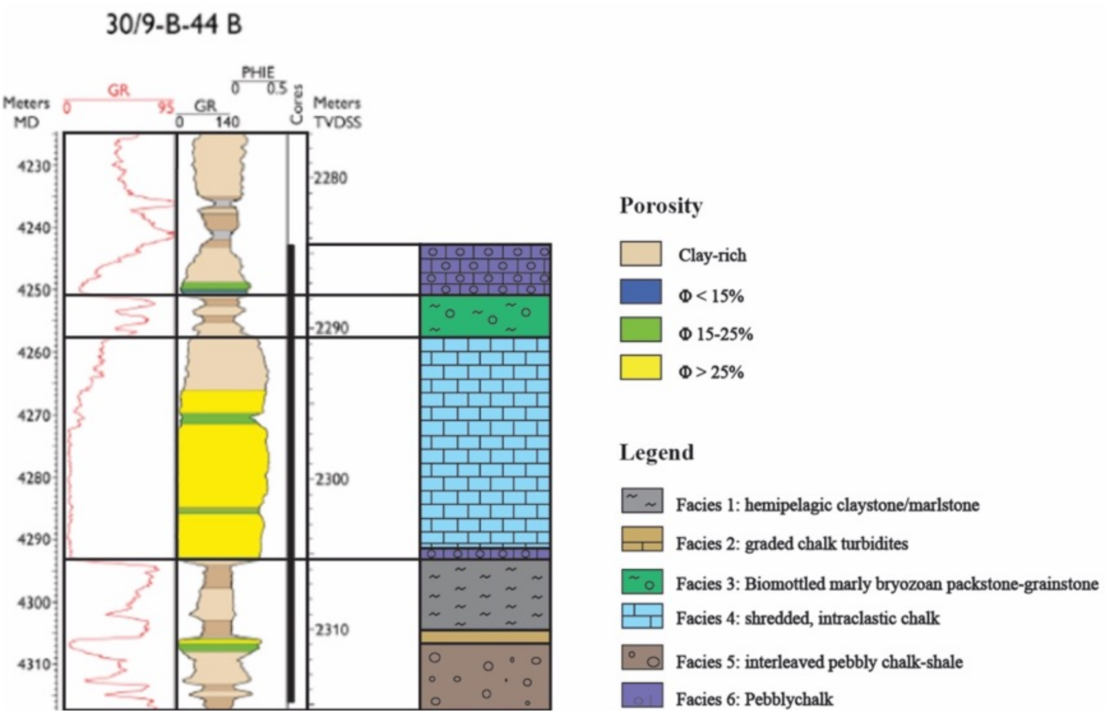

Figure 5.4: Gamma Ray, Sonic and PHIE log data at the cored interval in well 30/9-B-44B. The porosity values are based on the log data. Brown shades indicate clay-rich lithology, blue is porosity of 15 % or less, green specifies porosity between 15 and 25 % and yellow is porosity of 25 % or higher. The cored interval is marked by a thick black line, and the associated facies are indicated to the right. Modified from GEUS (2011).

Wennberg et al. (2013) analysed a deformation band in the second core from well 30/9-B-44 B (see section 1.3.3), located in a c. 2 m thick chalk stratum of a facies 2 – graded chalk turbidite, overlain by a c. 15 m thick claystone at 4305.50 m MD; see Fig. 5.4. The chalk is visually oil saturated and the deformation structures within show two main directions; one is subparallel to bedding and the other is in a conjugated set and at high angles to the bedding (Fig. 5.5). No stylolites have been identified in this chalk stratum.

Figure 5.5: The sampling location in well 30/9-B- 44B for thin section H215 at 4305.50 m MD. This thin section contains the deformation band studied by Wennberg et al. (2013). Notice discontinuities subparallel to and with high angles to the bedding, named "hairline discontinuities", also referred to as "hairline fractures" in the literature (Feazel, 1988). The arrow indicate the orientation to the bedding relative to the direction up towards the sea floor.

5.2.2 Well core 30/9-B-46 A

Well 30/9-B-46A has a cored interval from 3334.00-3369.86 m MD (see Table 1.1). Only four out of the six facies found in the cores from well 30/9-B-44B where recognized in this core (see section 1.3.2). The missing facies are facies 3 – biomottled marly bryozoan packstone-grainstone and facies 6 – pebbly chalk. Similar to the cores from well 30/9-B-44 B, facies 4 is the major facies in this core (Fig. 5.6).

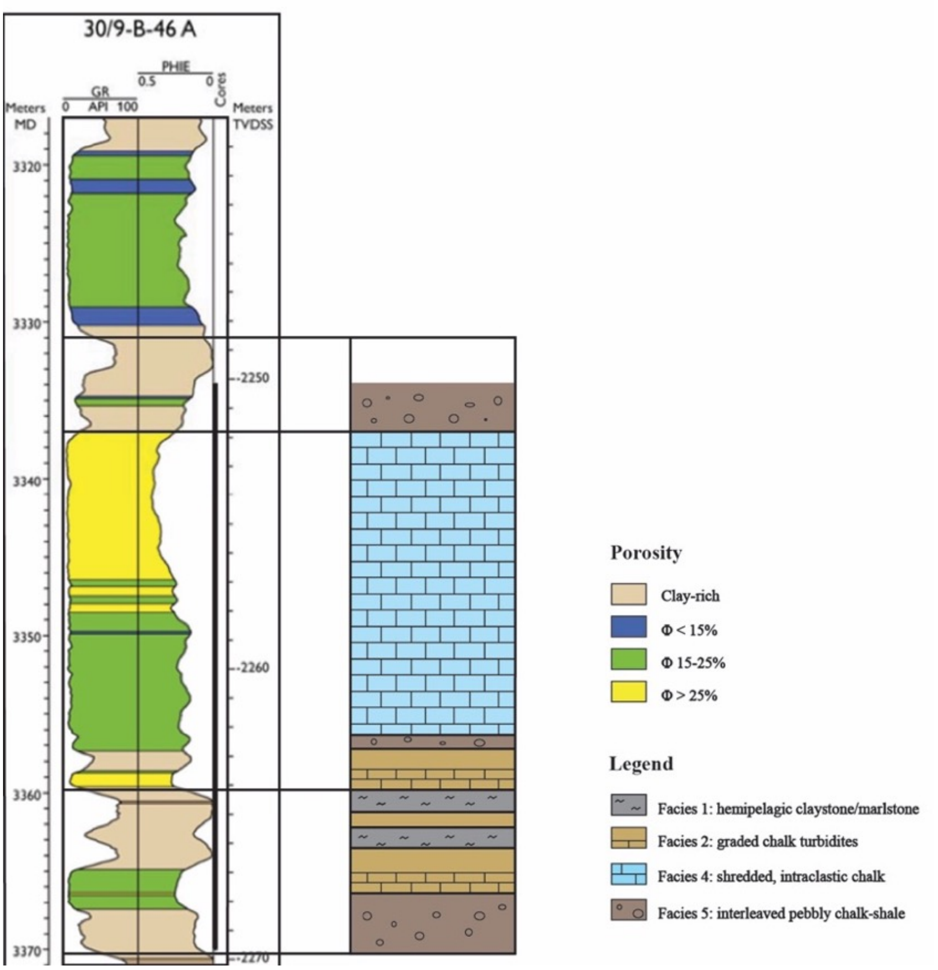

Figure 5.6: Log data of Gamma Ray, Sonic and PHIE at the cored interval in well 30/9-B-46-A. The black thicker line represents the cored interval, with the corresponding facies indicated to the right. The porosity is indicated, based on the log data. Brown shades indicate clay-rich lithology, blue is porosity of 15 % or less, green specifies porosity between 15 and 25 % and yellow is porosity of 25 % or higher. Modified from GEUS (2010).

The core interval 3348-3349 m MD, (see Fig. 5.7a), consists of very-fine grained chalk, at this scale it looks almost entirely homogenous with few chalk clast and impurities of clay highlighted within the stylolite structures. It is therefore interpreted to be intraclastic chalk of facies 4 described by GEUS (2010) (Tab.1.2). The presence of chalk intraclasts may indicate that the chalk has been re-depositioned (Fabricius, 2007). Very fine discontinuities or “hairline fractures” are observed with high angles to the bedding. Due to their very fine thickness it is difficult to distinguish their kinematics by the naked eye and is therefore presented as hairline discontinuities in this study. Hairline discontinuities are vastly present in the cored interval; some merge or diverge from each other, while others terminate against stylolites that are subparallel to the bedding (see Fig. 5.7c)

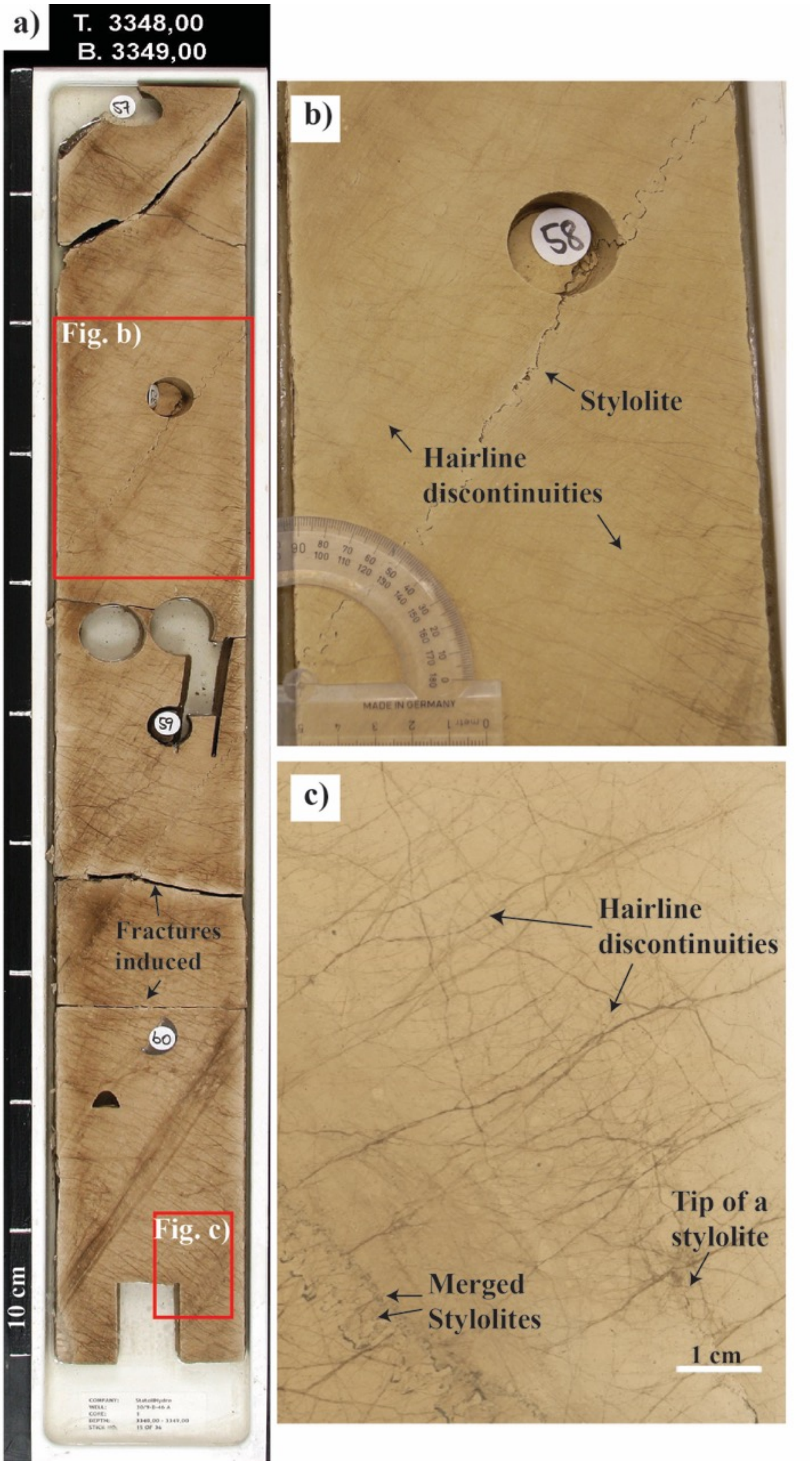

Figure 5.7: Core photos giving an overview of the different deformation structures visible in the cores. a) The A-cut of the core interval 3348-3349 m MD, b) a network of hairline discontinuities terminating into a single stylolite, c) close up of the deformation structures that are visible for the naked eye. Image from GEUS (2010) and might have been taken from the half-core hence the image is mirrored relative to the core photo a). The fractures induced by drilling are indicated by arrows in a).

5.3 Description of the density of the hairline discontinuities

Similar to the image in Fig. 5.7c and with the same orientation to the core, the images are provided from GEUS (2010). In Fig. 5.8a hairline discontinuities are hardly visible, whereas in Fig. 5.8b they orient in a network with a high angle to the bedding. The hairline discontinuities in Fig. 5.8c show two main orientations; one set of conjugating hairline discontinuities terminate with a high angle against hairline discontinuities that are subparallel to the bedding.

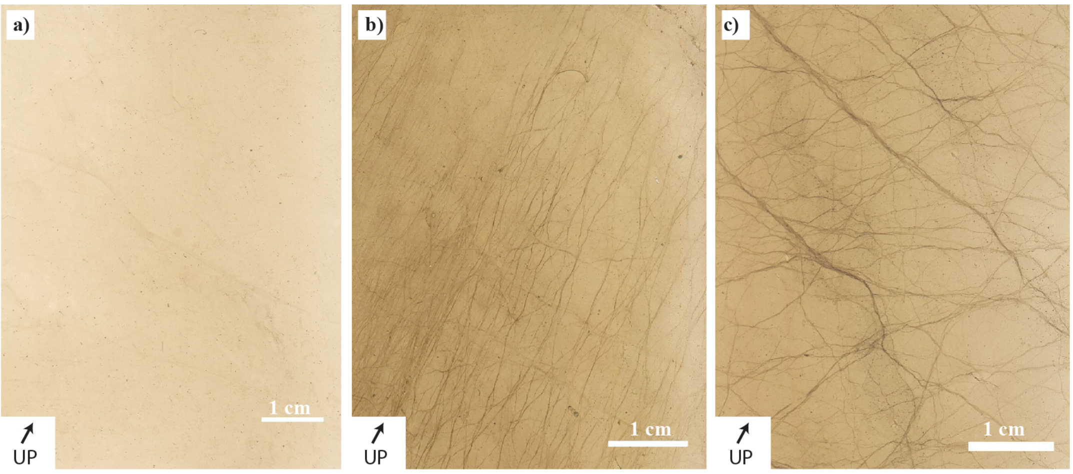

Figure 5.8: The images are provided by GEUS (2010) in RGB colours from the core from well 30/9-B-46 A, taken at a) 3342.95 m MD, b) 3343.95 m MD and c) 3344.95 m MD. All the images are taken where the host rock is of facie 4 with a porosity of 35% (GEUS, 2010). The vertical direction up for the bedding is indicated by the arrows.

The images were colour adjusted in ArcMap 10.3 by applying a standard deviation to the RGB band distribution, giving the RGB bands more values (Nixon, 2016) (Fig. 5.9).

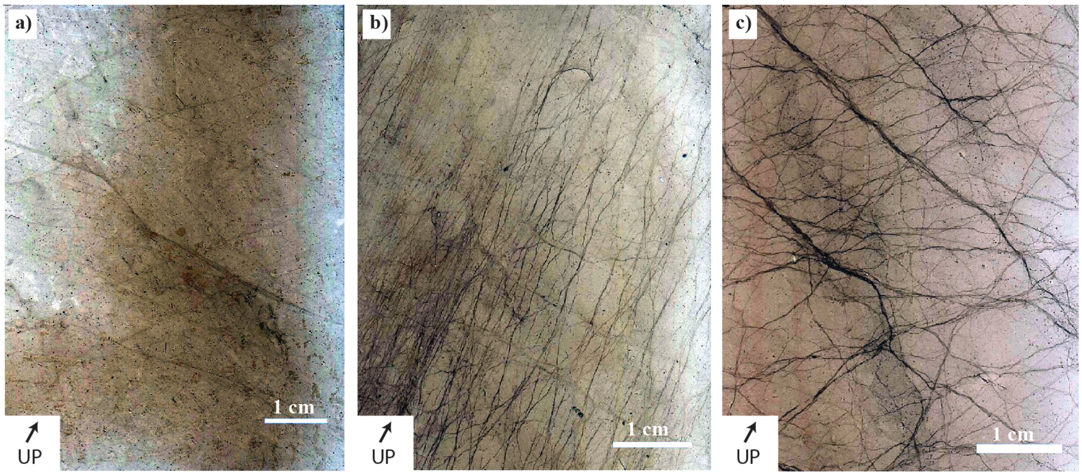

Figure 5.9: The images from Figure 5.8 manipulated by applying a standard deviation to the RGB band distribution, thus giving the RGB bands more values (Nixon, 2016). The vertical direction up for the bedding is indicated by the arrows.

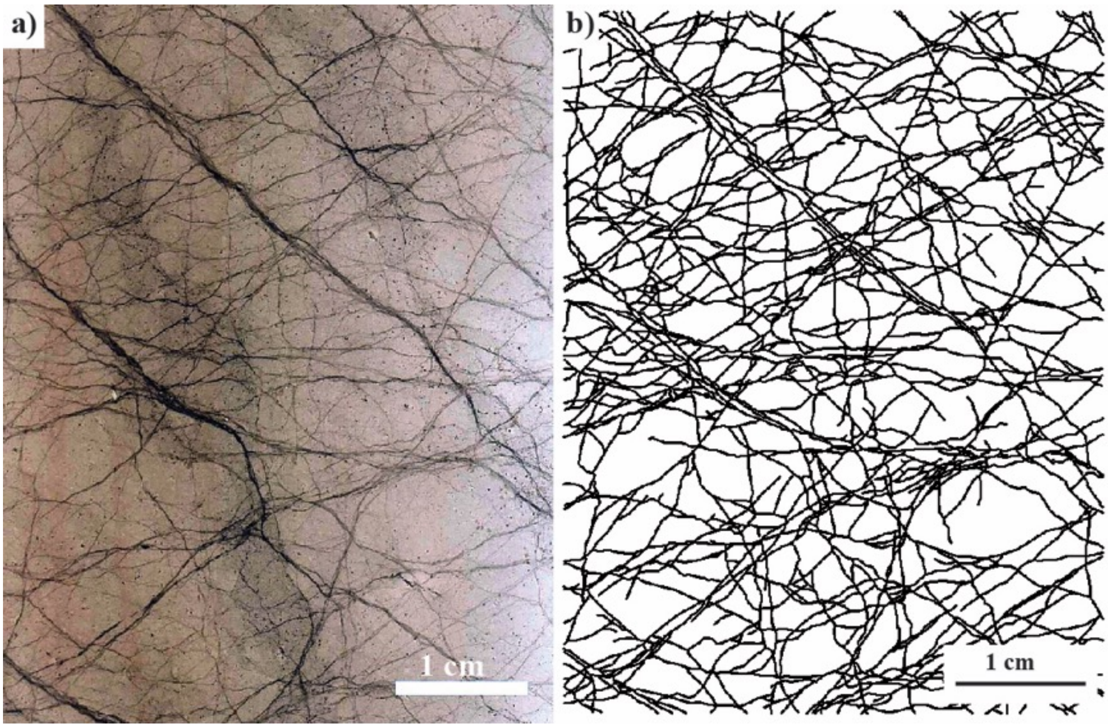

Figure 5.10: a) show the image from Fig. 5.9c), with a line drawing of the hairline discontinuities network illustrated in b).

The conjugated pattern exhibited in figure 5.8c is further highlighted in images 5.10 a) and b). Both images show a highly connective network of the deformation structures, in Fig.5.10b the lines that has been detected is visualized with the same thickness. Overall the pattern shows two main orientations of the hairline discontinuities, one orientation is defined by two conjugating sets terminating against a zone of discontinuities subparallel to the bedding. The two conjugate sets in Fig. 5.10, show curvature when linking. This behaviour of several narrow tabular band structures close together in zones are typical for deformation bands (see section 3.3.1). There has not been observed any offsets of the structures due to lack of markers.

5.3.1 Qualitative measurement of the density of the hairline discontinuities

To get a rough overview of the amount of hairline discontinuities through the whole core from well 30/9-B-46A, a qualitative measure was made out of the visible hairline discontinuities (Fig. 5.12). The core was subdivided into zones of different degrees of density of hairline discontinuities, as illustrated in Fig.5.11; degree 0 – being non visible hairline discontinuities, degree 1 – some single hairline discontinuities visible, degree 2 – some hairline discontinuities visibly connecting, degree 3 – network of visible hairline discontinuities and some stylolites interacting, degree 4 – intense network of visible hairline discontinuities interacting with merged stylolites.

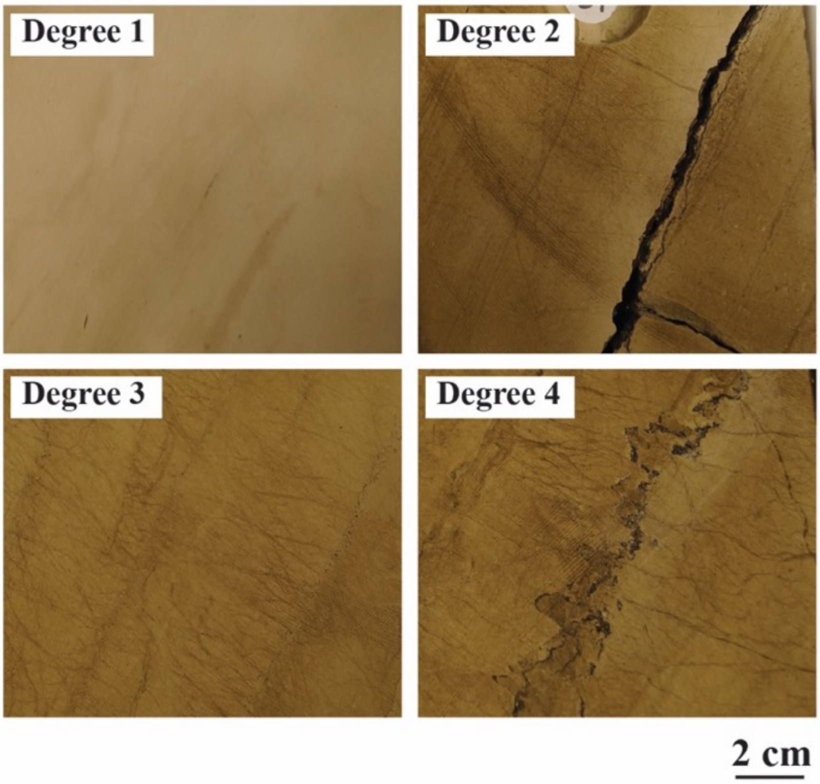

Figure 5.11: Core photos of the density degree of the hairline discontinuities (Hd) deformation structures. Degree 1 – barely any visible single Hd, degree 2 – some visible Hd, degree 3 – network of visible Hd with some related stylolites, degree 4 – the most intense network of visible Hd associated with merged stylolites.

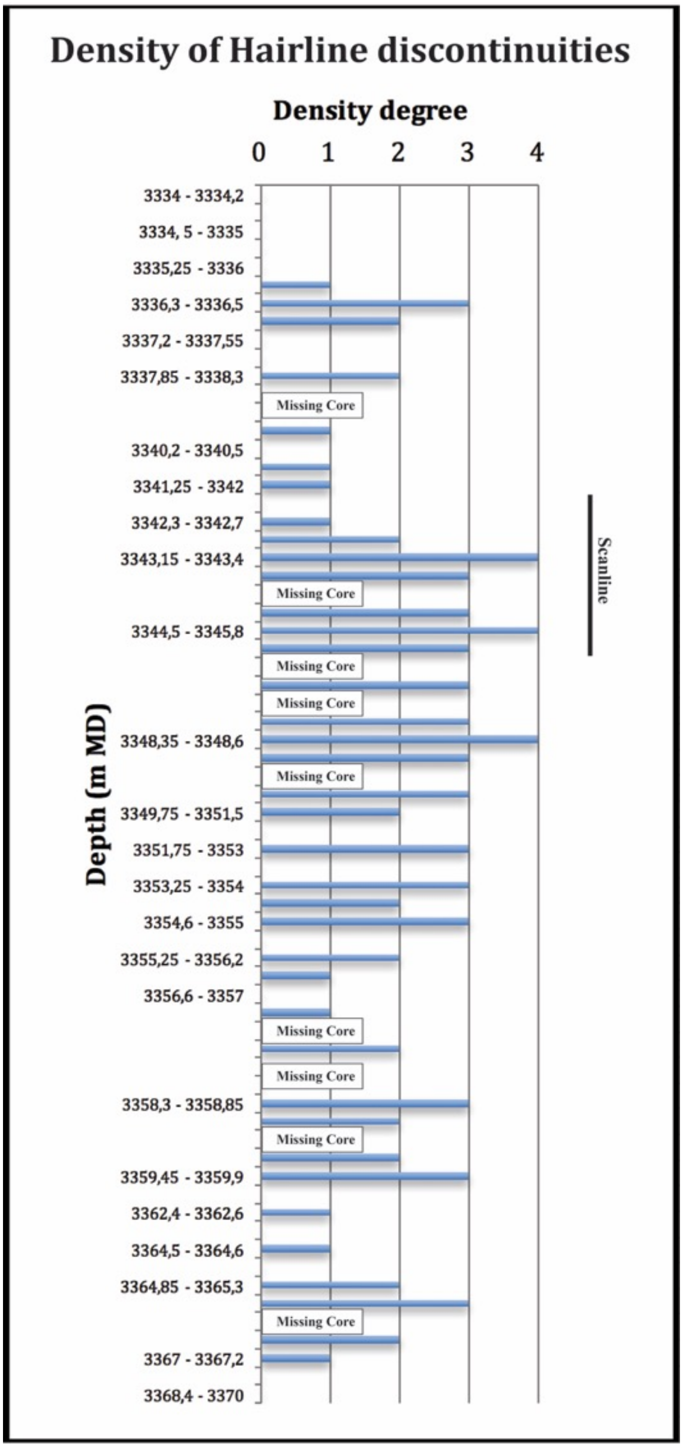

Figure 5.12: Graph illustrating the density of hairline discontinuities within the core from well 30/9-B-46 A. The density was highest in the interval between 3343 – 3348.6 m MD.

The density of hairline discontinuities was with the highest degrees of 3 to 4 between 3343 – 3348.6 m MD, compared to the rest of the core. The 4 m long scanline study was therefore focused on the 3342 – 3346 m MD core interval in well 30/9-B-46 A, to include the transition from density degree 0 to degree 4 (Fig. 5.12).

5.4 Intensity variations of structures

5.4.1 Scanline frequency curve

A 4 m scanline on of cores was picked out by the qualitative measurements of the density of the hairline discontinuities (see previous section 5.3.1). Based on the frequency of deformation structures per 0,2 m, a frequency curve was made (Fig. 5.13). Both in the density graph (Fig. 5.12) and in the frequency curve (Fig. 5.13) the frequency of hairline discontinuities increased to 38 around 3343.7 m MD and 34 at about 3345. m MD, the increase seems to occur after a large discontinuity.

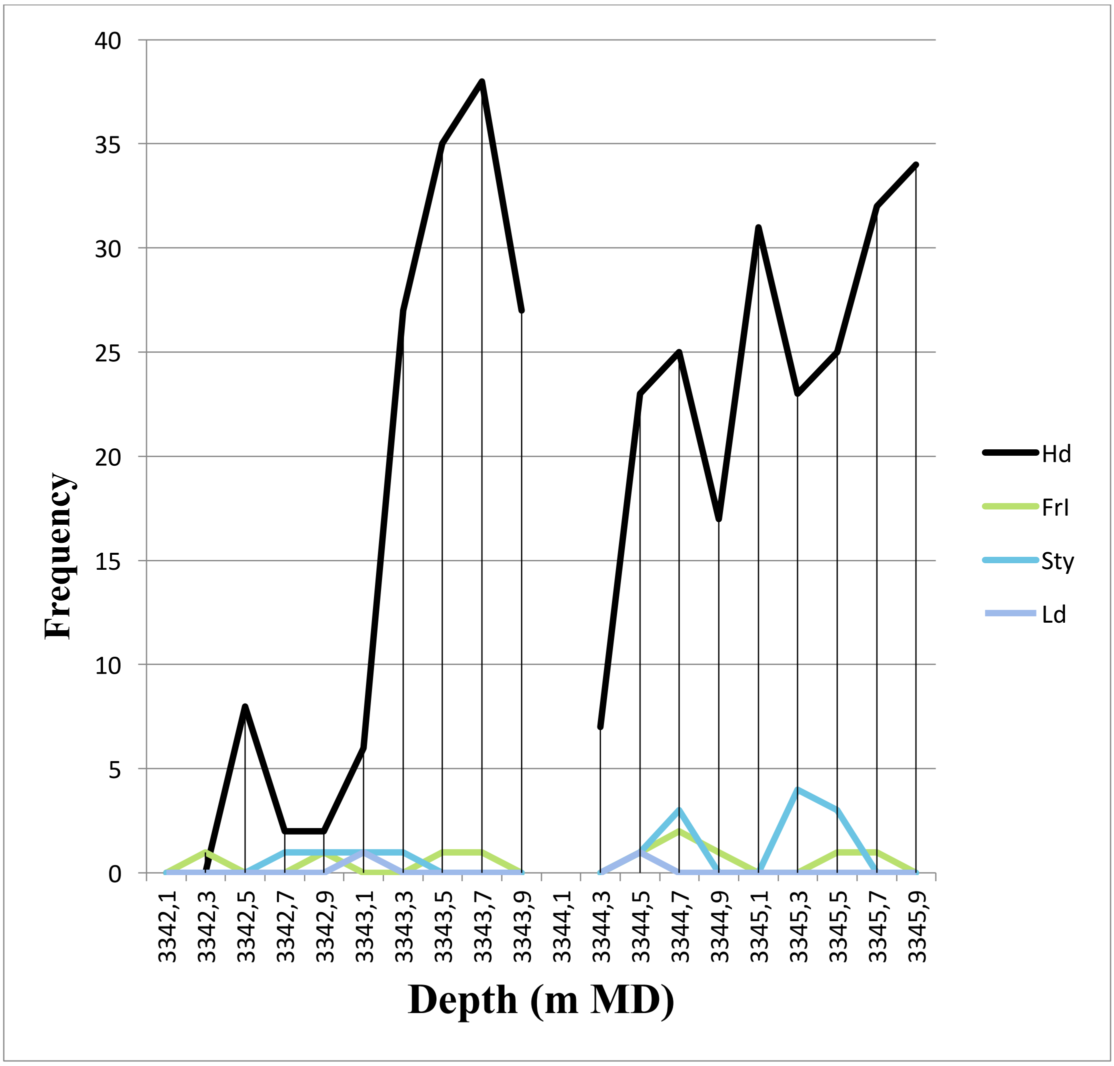

Figure 5.13: The number of hairline discontinuities (Hd), including fractures induced (FrI), stylolites (Sty) and larger discontinuities (Ld) per 0,2 m, measured along the scanline between 3342-3346 m MD on the core from well 30/9-B-46 A. The core was significantly missing between 3344 – 3344,337 m MD.

5.4.2 Cumulative curve

A cumulative curve (Fig. 5.14) was also made after the frequency of hairline discontinuities from the scanline data. The cumulative curve highlights the changes in frequency and can visualize the increase in hairline discontinuities by depth. The uniform distribution line illustrates the ideal linear distribution of hairline discontinuities from zero to the maximum amount of hairline discontinuities measured. The hairline discontinuities show notably increase in frequency around 3343,2 m MD and 3344,5 m MD, which confirms the peaks in the density graph, Fig. 5.12, and the frequency curve, Fig. 5.13.

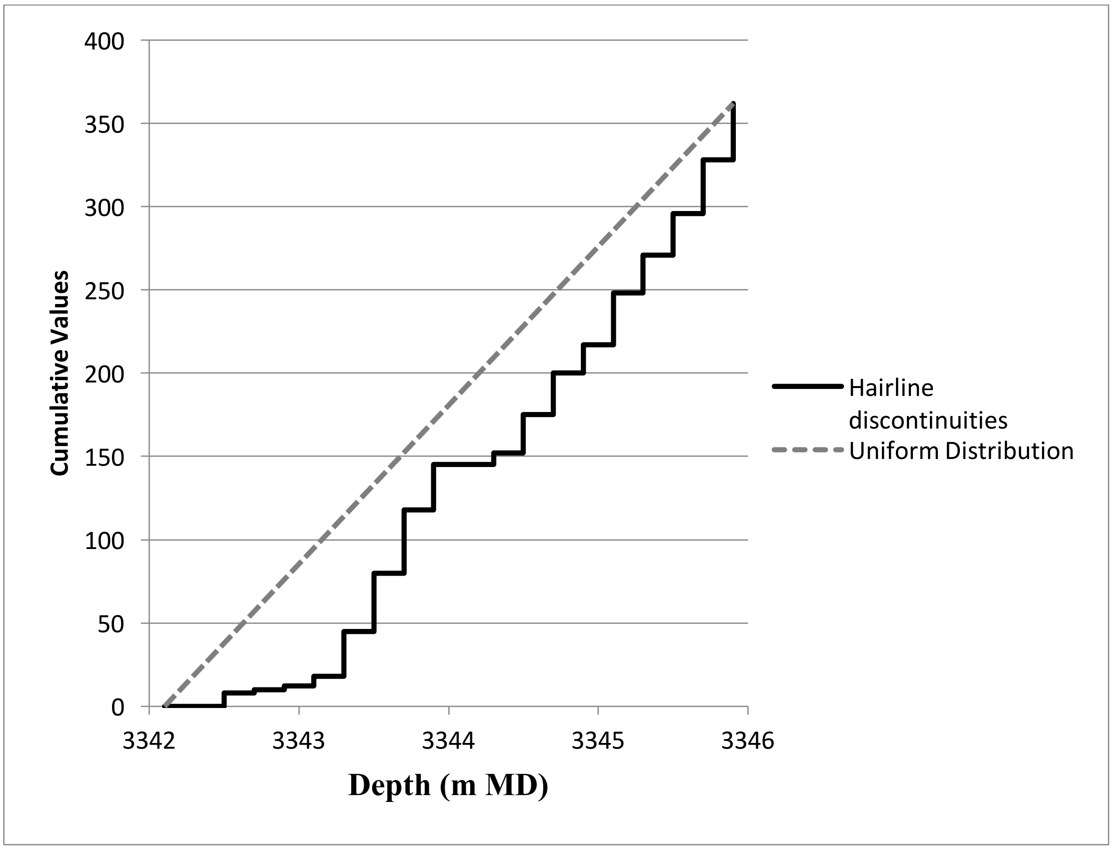

Figure 5.14: Cumulative curve of the frequency of hairline discontinuities measured on the scanline.

5.4.3 Orientation analysis

The orientation of the macroscopic deformation structures bisecting the line was measured during the scanline, and by adding the deviation to the bedding (c. 60°, see Tab. 1.1) the rose diagrams in Fig. 5.15 were made. The stylolites are notably oriented subparallel to the bedding and the hairline discontinuities are at high angle to the bedding (Fig. 5.15). The larger discontinuities (Ld) could be tectonic fractures (sensu Foster and Rattey, 1993, Toublanc et al., 2005), however, due to lack of markers it is difficult to distinguish and this structure will not be further investigated in this study.

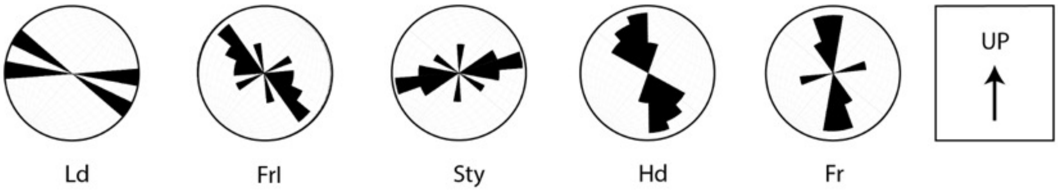

Figure 5.15: The rose diagrams shows the different orientations of the diverse deformation structures measured on the scanline; Ld – Larger discontinuities, FrI – Fractures induced, Sty – Stylolites, Hd – Hairline discontinuities and Fr – mineral filled fractures. The arrow indicating up indicates roughly the perpendicular orientation to bedding of the facies 4 strata, relatively to the orientation of the measured data illustrated in the rose diagrams.

5.5 Host rock characterization

A chemical analysis of the host rock was done at the SEM (see section 4.3.2 for details), see Fig. 5.16 and 5.17. The image used was a BSE image. The host rock is shown as a mainly homogeneous and very fine-grained chalk with some minor impurities, such as grains of quartz and clay. The chemical analysis (Fig.5.17) confirms that the main mineral content of the host rock is of calcite with some impurities of clay and quartz grains. At this scale the intragranular pore space within the round foraminifera chambers are visible, and a calcite cemented foraminifera (Fig. 5.16).

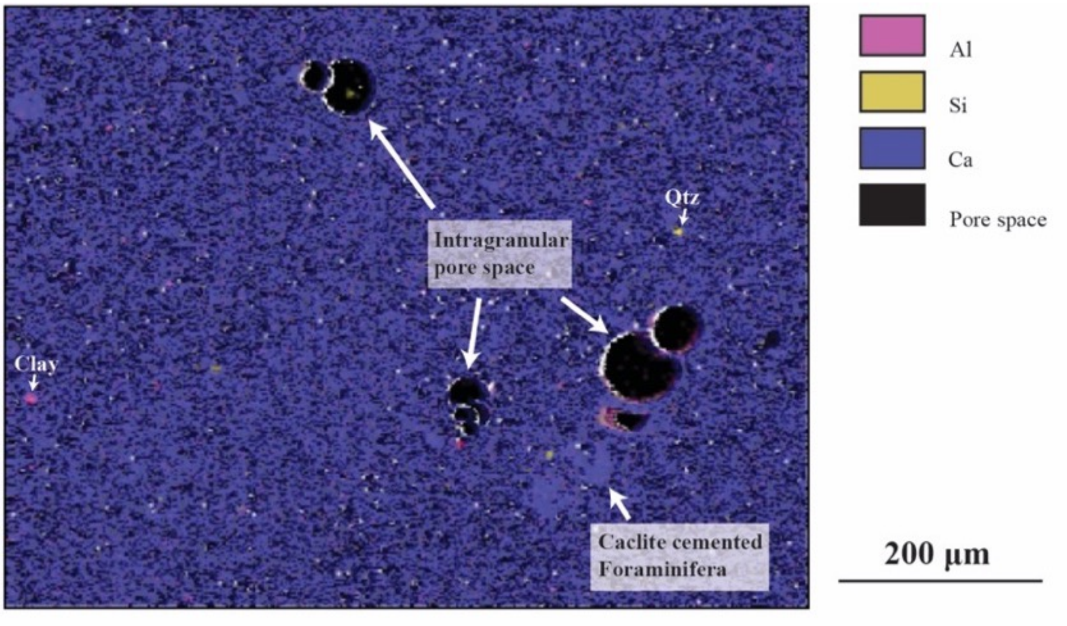

Figure 5.16: Chemical analysis of an BSE image of the host rock, done by the x-ray characteristic by the SEM. The sample BSE image is from thin section 4 at 3340.72 m MD in well 30/9-B-46 A.

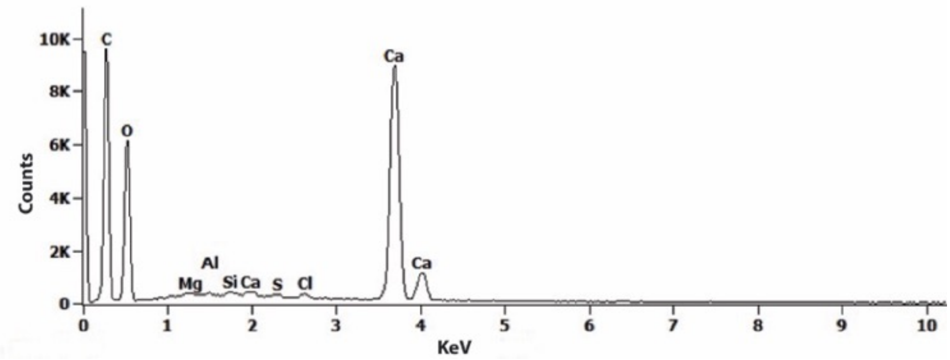

Figure 5.17: An Energy Dispersive X-Ray Spectrum showing the elemental analysis and chemical characterization of the host rock of facies 4. The C peak are due to the proxy coating on the sample. The Ca peaks corresponds to $CaCO_3$ according to Welton (1984).

At the scale of Fig. 5.16, intragranular pore space within the foraminifera chambers are visible, however, the grains to the host rock are barely distinguished. Hence a SE image was done on 12 K high magnification to fully see the grains and the intergranular pore space (Fig. 5.18) (Choquette and Pray, 1970). The grains are angular and represent broken coccoliths and rhombic micrite crystals. Cementation is not clear, however, there are some visible impurities of clays between the coccolith grains. The average grain size of the host rock is c. 2 µm, where the smallest grain size is c 0.4 µm and the largest grain size c. 12 µm. Whereas the foraminiferas and the intragranular pore space are of silt size, while the intergranular pores are around 1-10 µm in diameter. The intergranular microporosity seen in Fig. 5.18 is as high as 30%. As observed in Fig. 5.16, calcite cementation occurs within some of the hollow foraminiferal chambers. Notice that the calcite crystal of the cement is significantly larger (c. 60 μm) than the host rock grains; the calcite crystals must have grown within the hollow foraminifera in optical continuity. The intergranular pore space must have been too small to let intergranular cementation occur. The poorly preservation of whole coccospheres may indicate that extensive compaction has occurred (Welton, 1984). The host rock composes therefore mainly of coccolithic matrix with some dispersed foraminiferal skeletal grains, making it a chalk mudstone to a chalk wackstone. The grains in the host rock show partly sutured and dissolved grain boundaries, with some grains being clustered, indicating chemical compaction (Flügel, 2004) (see section 4.3).

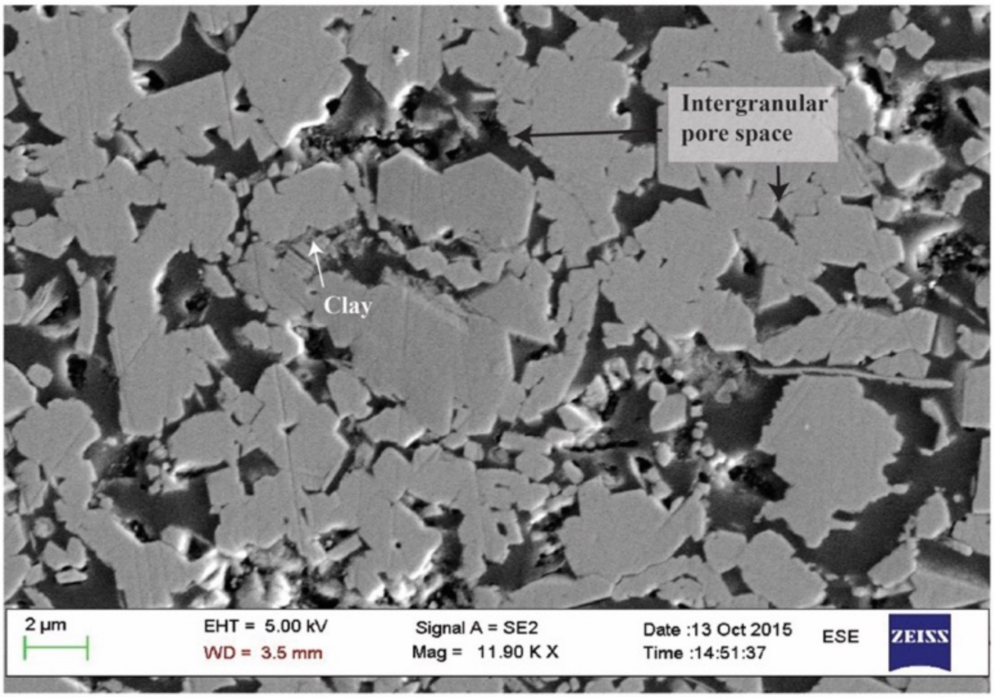

Figure 5.18: SE-SEM image of the host rock at 12 K magnification to show the grains. At this scale the intergranular pore space and the microporosity between the broken coccoliths and the micrite crystals are well represented. This sample SE-SEM image is from thin section 6 at 3343.17 m MD in well 30/9-B-46 A.

5.6 Microstructural analysis

23 thin sections, 1 from well 30/9-B-44 B and 22 from well 30/9-B-46 A were analysed in this study. A description of the different types of deformation structures observed, such as stylolites, fractures and deformation band will be presented below.

5.6.1 Stylolites and fractures

5.6.1.1 Stylolites

As seen from the rose diagram for stylolites (Fig. 5.15) the majority of the stylolites are subparallel to traces of bedding and it is therefore assumed to be a parallelism between the two. Three different types of bedding-parallel stylolites where observed in the core to the well 30/9-B-46 A, see Fig. 5.19. Following Safaricz and Davison (2005) (see section 3.2.3), the stylolites in Fig.5.19 could be classified as; b) single stylolites, c) several stylolites close together, some which have merged, and c) multiple stylolites merged together to form a flaser residue seams.

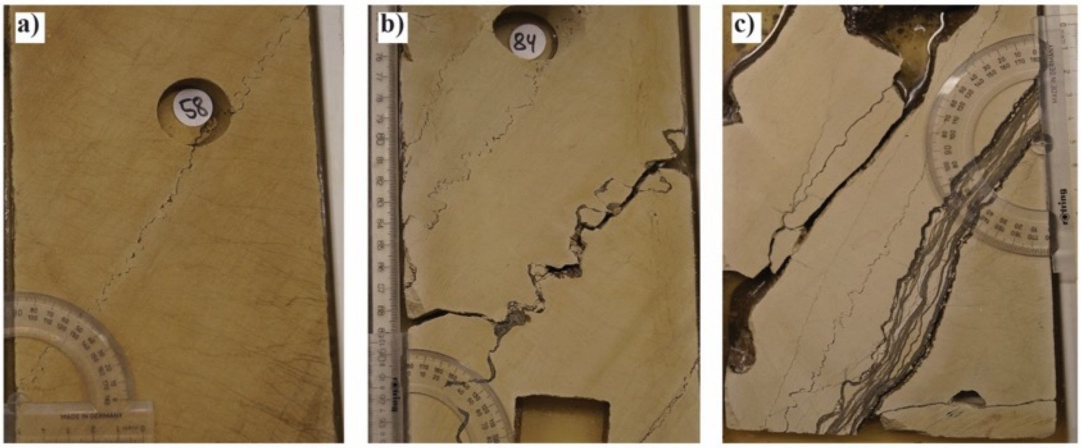

Figure 5.19: Display the different stylolites found in the core to well 30/9-B-46 A.

The chemical analysis displayed in Fig. 5.20 show that the serrated structure outlining the stylolite contain a major amount of clay and silica minerals, compared to the host rock comprising mainly of clean chalk. Extensional fractures terminate at high angle against the stylolite in Fig. 5.20, and an undulating fracture is following the serrated pattern to the stylolite.

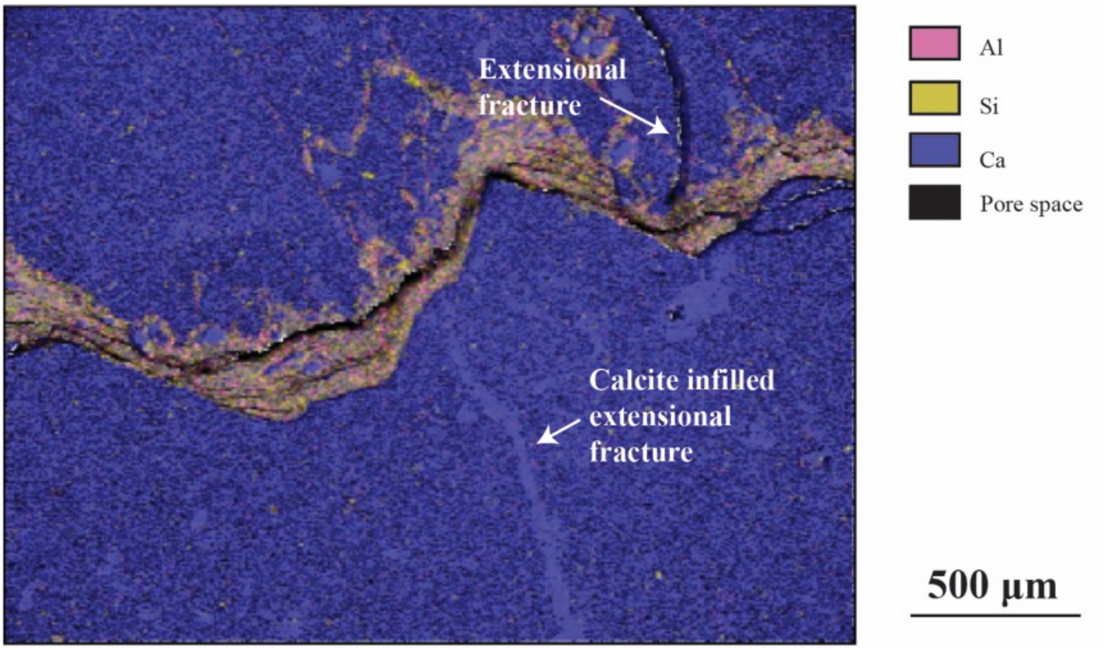

Figure 5.20: Chemical analysis of a SE-BSE image of a stylolite, in thin section 9 at 3354.55 m MD in well 30/9-B-46A, done by the x-ray characteristic by the SEM. The stylolite contains significant amount of clay and silica minerals, compared to the host rock. Notice the fracture following the stylolite's serrated pattern and the extensional fractures with high angle to the stylolite.

The stylolite in Fig. 5.21 was sampled from the core in well 30/9-B-46A at 3344.51 m MD, it is a bed-parallel stylolite (see section 3.2.3) and is longer than the thin section and terminates laterally against a pyrite within a longer discontinuity and the core wall. The amplitude to the stylolite is c. 200 µm with its apparent thickness being c. 300 µm.

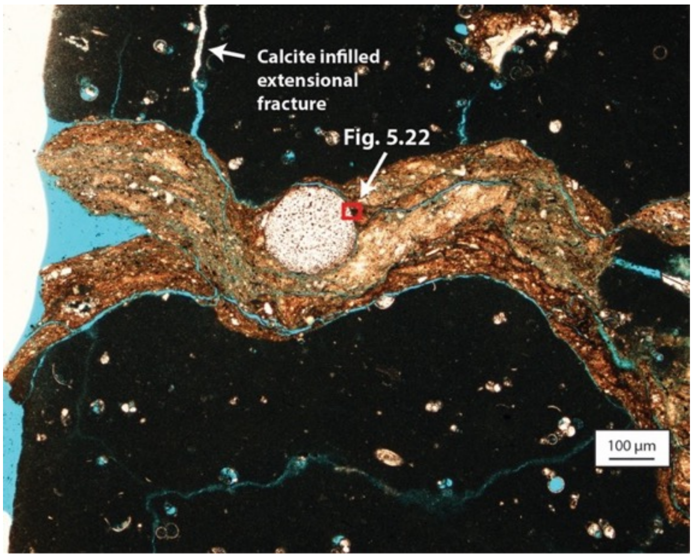

Figure 5.21: A PPL image of a stylolite in thin section 7 at 3344.51 in well 30/9-B-46 A. Fig. 5.22 is located within the red polygon.

Within the stylolite in Fig. 5.21, the grains are less angular than the host rock with evidence of dissolved grain boundaries, see Fig. 5.22. The clay minerals are dominant and aligned perpendicular to the maximum stress of pressure dissolution following the serrated zone defining the stylolite. The fractures are c. 3 µm in apparent thickness and have followed the grain boundary to the larger grain to the left and developed parallel to the clay minerals to the right (see Fig. 5.22).

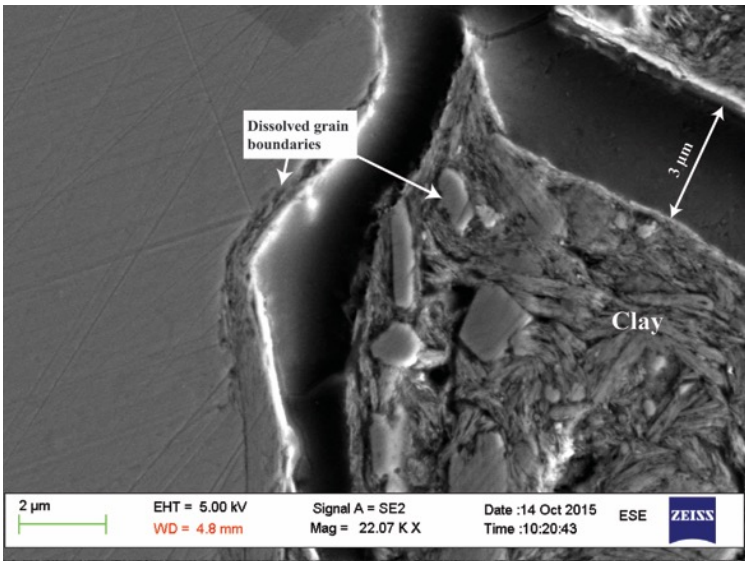

Figure 5.22: SE-SEM image within the stylolite in Fig. 5.21 showing chalk particles with dissolved grain boundaries and aligned clay minerals.

Based on the orientation measured to the stylolites done in section 5.5 (see Fig. 5.15) indicates that most of the stylolites are bed-parallel, and therefore they are morphologically related. Chemical analysis show that the serrate zone of the stylolites contain partly dissolved insoluble residue such as clay minerals and quartz grains. The clay minerals within the stylolite zone show alignment, and are parallel to the zone and the bedding. This alignment of clay minerals tends to develop the preferred weakness zone for fracturing, as seen by the anastomosing fracture pattern within the stylolite in Fig. 5.21. Extensional fractures seem to occur perpendicular to the orientation of the bed-parallel stylolites. Some of the extension fractures are also infilled with calcite crystals, so called veins, which indicates that fluids have passed through the area and precipitated. For instance, in Fig. 5.20, the extension fracture above is not infilled by calcit,e such as the extension fracture below the stylolite. This can indicate that the stylolite act as a baffle for fluid flow in this area. No deformation bands were identified in the PPL image of thin-section 7, however, these fractures are interpreted to be stylolite-related fractures (see section 3.2.3)

5.6.1.2 Extension fractures

As observed in both Fig. 5.20 and 5.21 extension fractures are present with high angle against the stylolites. Some of the extensional fractures are filled with calcite, the calcite crystals are significantly larger than the micrite crystals and the broken coccoliths composing the host rock (Fig. 5.23). The infilled extensional fracture contains some amount of intergranular pore space.

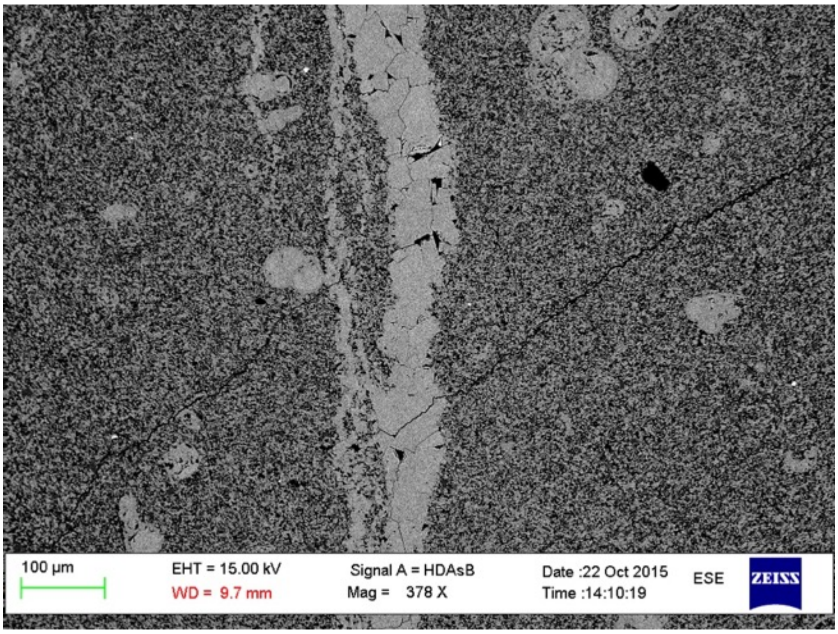

Figure 5.23: A calcite infilled extensional fracture, or also called a calcite vein, in thin section 9 at 3354.55 m MD in well 30/9-B-46 A.

In Fig. 5.26, an extensional fracture with high angle against the stylolites is observed within a dark discontinuity band (see Fig. 5.24). The fractures do not cross-cut by, rather terminates against the stylolites. The fractures seem therefore related to the stylolite, and are therefore interpreted to be stylolite-related fractures (see section 3.2.3 for theoretical details).

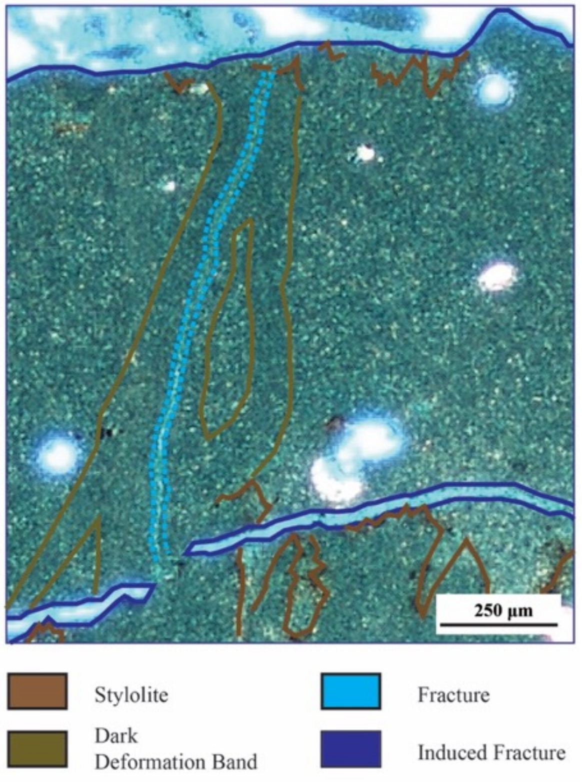

Figure 5.24: Fracture within a dark discontinuous band terminating at both ends with high angle towards the stylolites. The sample is from thin section 4 at 3340.72 m MD in the core to well 30/9-B-46 A, and is located in a red polygon in Fig. 5.26a.

5.6.1.3 Irregular fractures

The irregular fractures shown in Fig. 5.25 have a tortuous pattern, and are infilled by significantly larger calcite crystals than the micrite crystals and the coccolith fragments constituting the host rock. The contact between the infilled fractures and the host rock is therefore sharp. No apparent deformation band and stylolites are recognized in thin section H44. Some intergranular pore space are present within the irregular fracture. Orientation to bedding is not known for the irregular fracture in Fig. 5.25 due to lack of markers. The irregular fractures are subparallel to each other, and smaller fractures are terminating against the irregular fractures with high angle (see Fig. 5.25b). When looking at the thin section through normal light, faint hairline discontinuities structures are observed subparallel with the veins, however, they are not shown in the optical microscope. Nevertheless, the faint discontinuities could indicate the orientation to the irregular fractures being at high angle to the bedding. The apperent thickness to the irregular fracture varies from 0.45 mm to 0.07 mm, and the smaller fractures terminating against the irregular fractures have a thickness of about 0.02 mm and do not contain any calcite crystals.

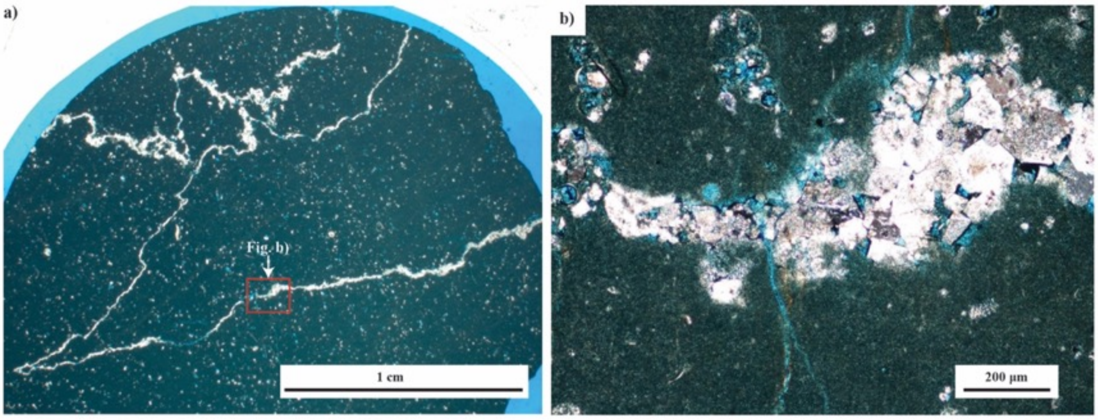

Figure 5.25: Displaying irregular calcite veins located at 3344.75 m MD in well 30/9-B-46 A in thin section H44.

Commonly, these types of fractures have been classified as irregular fractures, occurring in chalk. Often seen related to the tectonic trend (Toublanc et al., 2005). They are an irregular version of extension fractures infilled with calcite, and will therefore be classified as irregular calcite vein and stylolite-related fractures (see section 3.2.3).

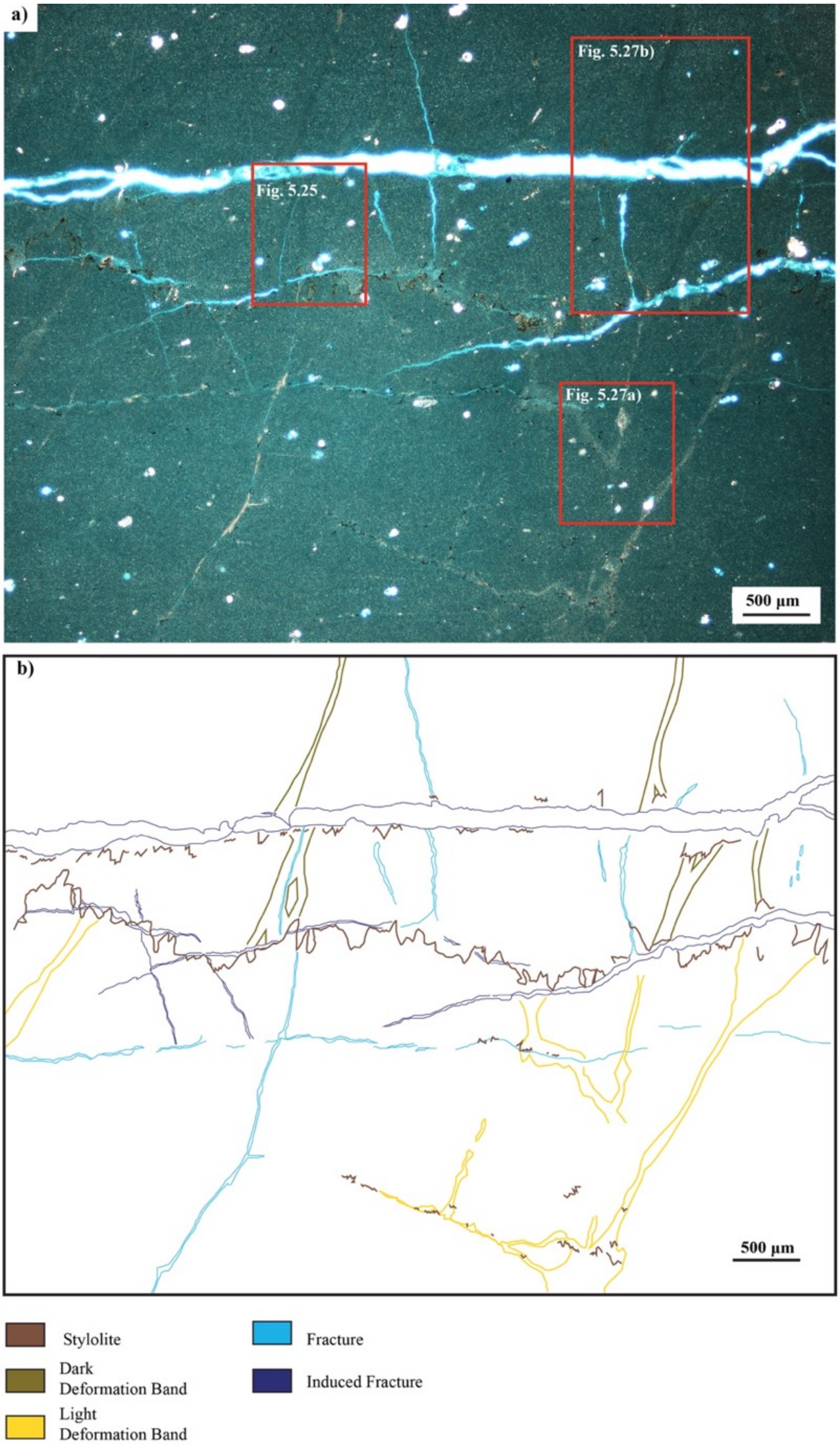

Figure 5.26: The microscopic deformation structures present in the core from well 30/9-B-46 A are here present and displayed in a PPL image from thin section 4 at 3340.72 m MD.

In Fig. 5.26, the stylolites and smaller dissolution seams present at this scale are indicated by brown serrated lines. The stylolites present are most likely subparallel to bedding, however due to lack of markers for orientation of bedding it is difficult to define the right way up. The fractures induced by drilling the plug have developed along the two prominent stylolites (see section 4.1 for details on drilling induced fractures). An array of fractures with same orientation as the fractures induced show patches of calcite infill and is thereby interpreted to be of natural origin and not fractures induced. The dark discontinuity band observed in Fig. 5.24 (see section 5.6.1.2) contain an extensional fracture at high angle to the stylolites could indicate a zone of localized strain such as a deformation band. The fracture show parallelism with the dark discontinuity, and in theory the dark discontinuity could have predated the fracture (see section 3.3.3 for theoretical details).

5.6.2 Structures interpreted as deformation bands

The discontinuities are observed as narrow tabular zones, with a different colour than the host rock (see Fig. 5.26 and 5.27). Most of them are at high angle to the bedding and can therefore not be lamellas within the host rock. The tabular zones diverge before terminating against the stylolites (see Fig. 5.26 and 5.27b). Therefore, the zones may indicate strain such as deformation bands.

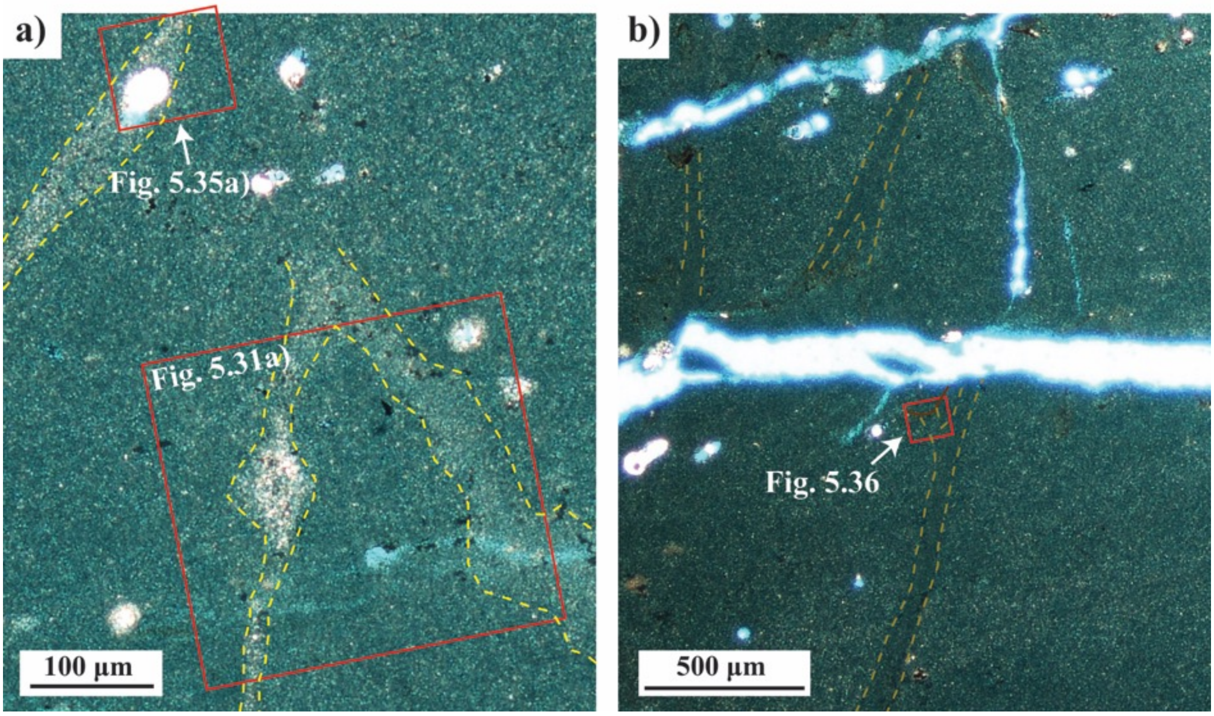

Figure 5.27: a) presents light deformation bands, whereas b) display dark deformation bands, both present in Fig. 5.26. Notice how the dark deformation band diverge into two before it terminates against the stylolite. The images are flipped 180° to match the following SEM images. The location to Fig. 5.35a), Fig. 5.31a) and Fig. 5.36 are indicated by the red polygons.

5.6.2.1 Porosity measurements of the deformation bands

Porosity measurements where done by using the ImageJ 1.50f software (see section 4.4 for details) on all the observed deformation bands captured in SE-SEM images (Fig. 5.30). A porosity measurement is illustrated in Fig. 5.28 for a “light” deformation band profile and in Fig. 5.29 for a “dark” deformation band profile. The results from the porosity calculations are presented in the graph in Fig. 5.30.

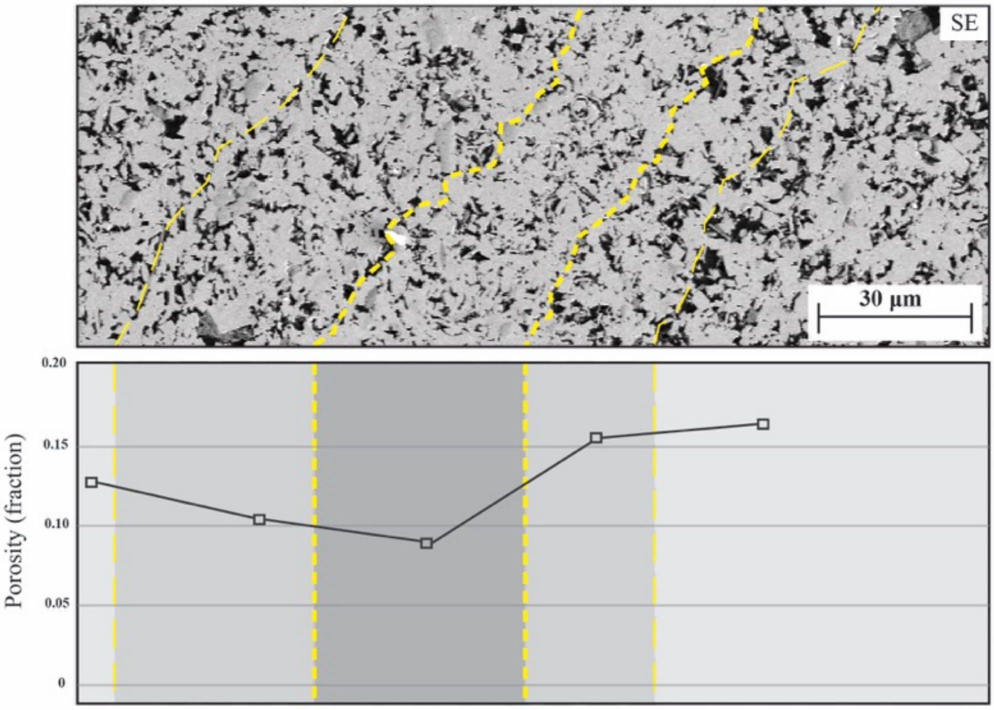

Figure 5.28: A porosity measurement by ImageJ 1.50f on a light deformation band in thin section 1 at 3335.76 m MD in well 30/9-B-46 A. The deformation band is highlighted by the yellow stippled line and subdivided into the area with the most porosity reduction as the band and the zones of slightly porosity reduction as the transition zones.

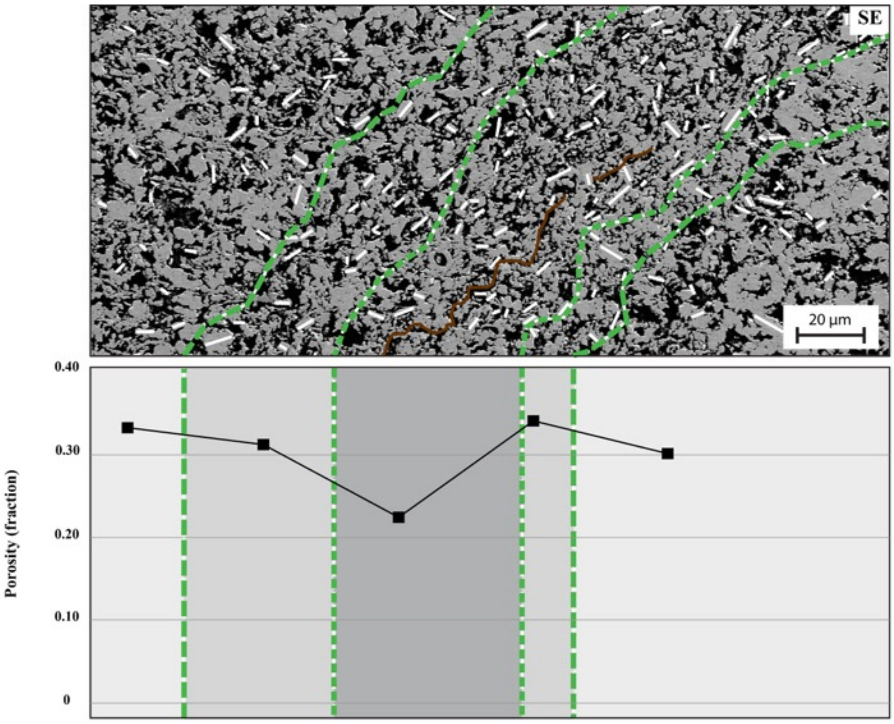

Figure 5.29: A porosity measurement by ImageJ 1.50f on a dark deformation band in thin section 4 at 3340.72 m MD in well 30/9-B-46 A. Notice the intergranular fracture subparallel to the orientation of the deformation band, highlighted as a brown dotted line. The white lines are to indicate the alignment of the grains and to help

visualize the deformation band. Whereas the green dotted line highlights the inner part of the band and the transition zone.

Both Fig. 5.28 and 5.29 show a significant reduction in porosity within the band relative to the host rock, with transition zones of gradually increase in porosity on both sides of the band. Whereas in Fig. 5.29 the transition zone to the right show a slightly increase in porosity compared to the host rock. The calculated porosity (Fig. 5.30) within the deformation bands show that the porosity is reduced with c. 10 % porosity within the band compared to the host rock, with a slightly porosity reduction within the transition zone. The reduction in porosity indicate that strain hardening and compaction could have occurred within the bands, which helps to confirm that these narrow zones are of deformation bands structures.

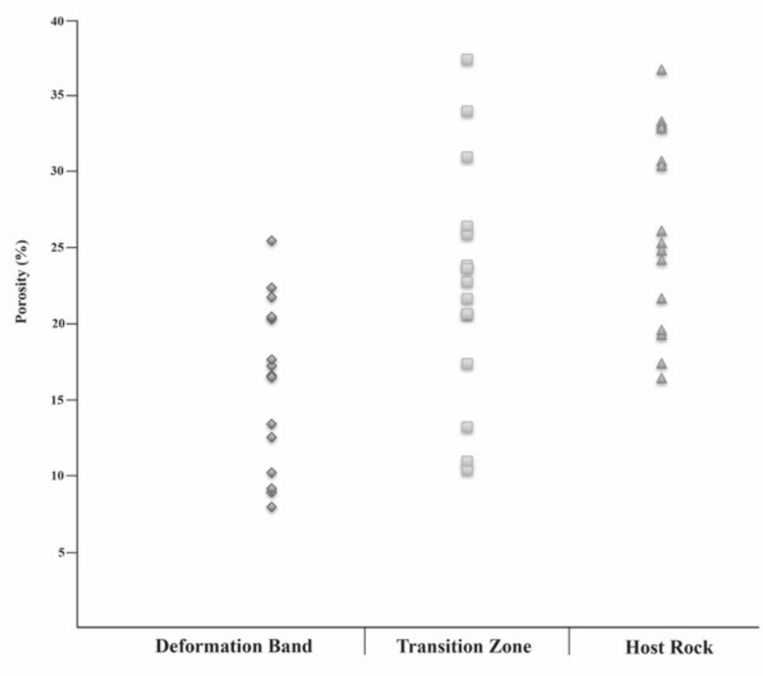

Figure 5.30: Porosities measured for observed deformation bands, transition zones and the surrounding host rock by the usage of ImageJ on SE-SEM images. The measurements show that the intergranular pore space in the deformation bands are significantly reduced relative to the host rock.

As predicted by Fossen et al. (2007) and Rotevatn et al. (in press), no deformation bands were observed in the bioturbated parts of the studied cores, however they are generally abundant in the non-bioturbated chalk dominated parts.

Through the optical microscope three different types of strain localized tabular discontinuities where mainly observed and interpreted as deformation bands. Two where oriented at high angle to the bedding, one off-white in colour noted as light deformation band (Fig. 5.27a) (5.6.2.2) and the other being darker green than the host rock, thus the designation dark deformation band (Fig. 5.27b) (5.6.2.3). The third type of deformation bands were oriented parallel with the bedding and darker in colour than the host rock (5.6.2.4). These three different deformation bands will be further outlined and described with respect to their microstructural features:

- “Light” deformation bands at high angles to bedding
- “Dark” deformation bands at high angles to bedding
- Deformation bands subparallel to bedding

5.6.2.2 “Light” deformation bands at high angles to bedding

The light deformation bands in Fig. 5.31 are visible in both BSE and SE images. The deformation bands have a mainly planar geometry, however, the thickness of the deformation bands can vary, as illustrated in Fig. 5.31a where the thinnest part of the deformation band is 32 μm and the thickest up to 100 μm in apparent thickness. The contact between the deformation bands and the host rock are gradual, as shown also in Fig. 5.27a, notably the section in Fig. 5.31b show a sharper part of the deformation band due to a cluster of larger grains, where the largest grains are c. 4 μm.

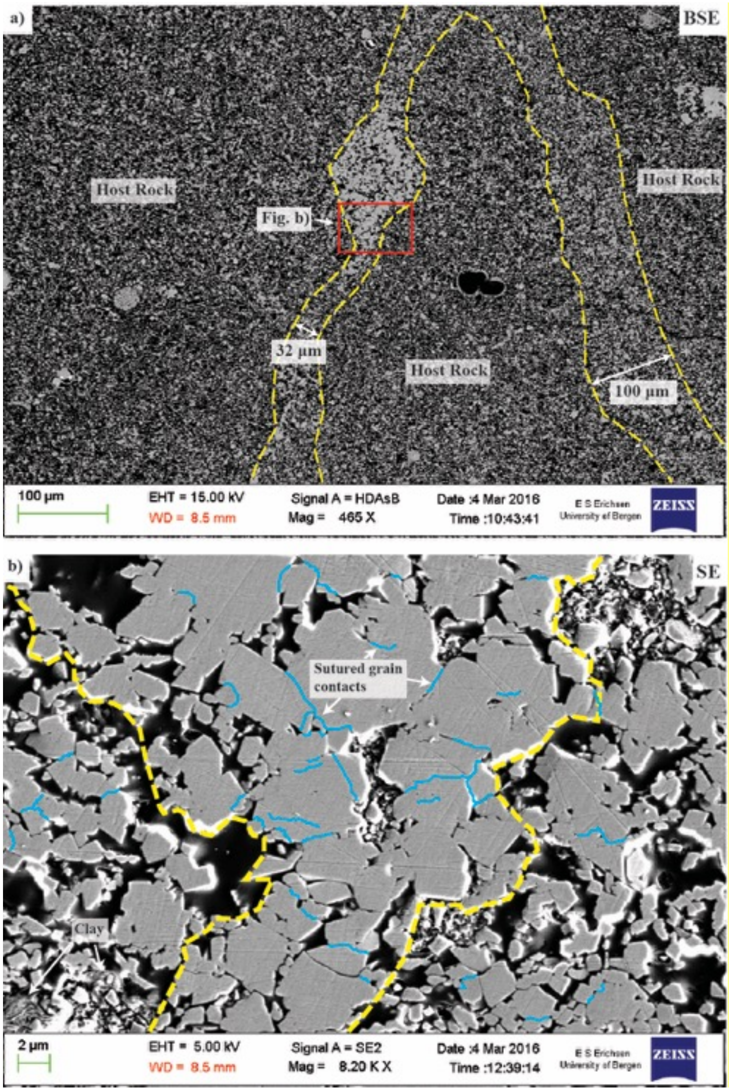

Figure 5.31: A light deformation band branch, a) showing variation in thickness along the deformation band, b) sutured grain boundaries within the deformation band are dominant.

The band show reduction in intergranular pore space due to the clustering of grains, which may be the reason the bands are highlighted in the SEM images. Tangential contact between the clustered grains occur, however sutured grain boundaries are the most prominent feature and indicating chemical compaction (see section 4.3). The clustered grains have primarily high sphericity and lack a prominent elongation to indicate alignment and orientation. Nevertheless, an orientation analysis was done (see Fig. 5.32) which implied that the grains within the deformation band are aligned along the band. The transition zone was measured to be around 2 µm and the band itself to be c. 3.75 µm (Fig. 5.32).

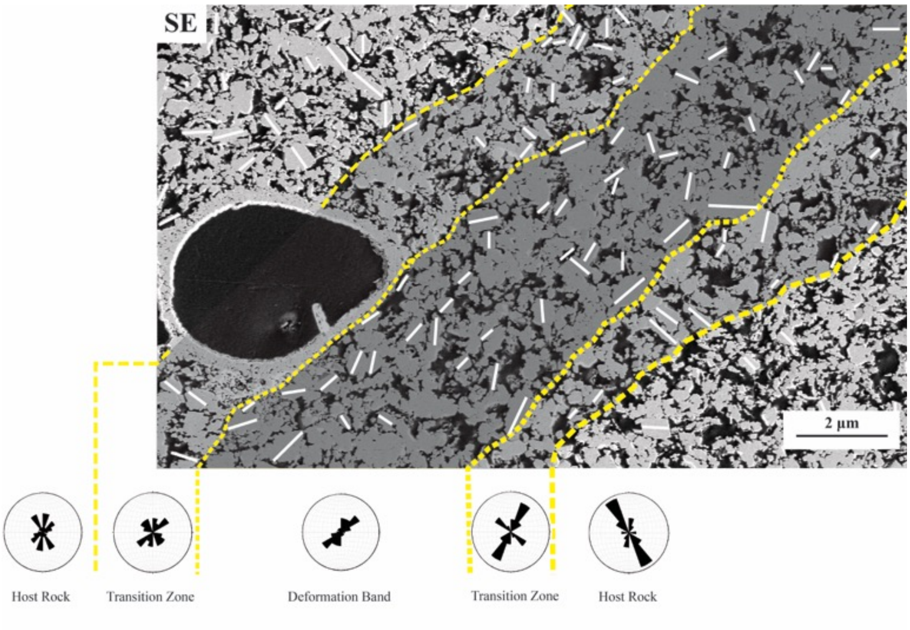

Figure 5.32: The deformation band is highlighted by a yellow stippled line and a grey coating that is coloured on to illustrate the zones building up the deformation band, and to highlight the alignment of grains are indicated by the white lines in this SE-SEM image. The rose diagrams bellow was made to further highlight the orientation to the alignment of the grains.

The "light" deformation band observed and analysed by Wennberg et al. (2013) (see section 1.3.3) in Fig. 5.33, shows that the deformation band is at high angle to the bedding, by the specification that the elongated grains to the fossils indicates the orientation to bedding.

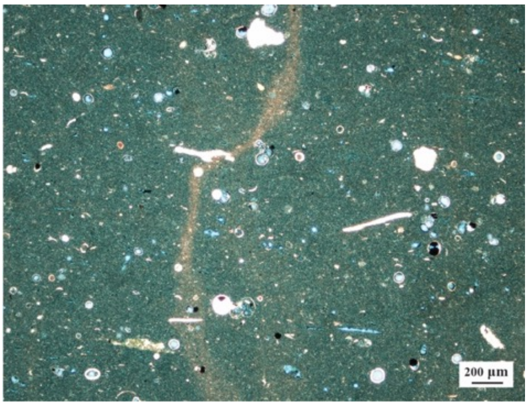

Figure 5.33: The deformation band analysed by Wennberg et al. (2013) in thin section H215 at 4305.50 m MD from Well 30/9-B-44B.

The light deformation band found in thin section H 215 at 4305.50 m MD from well 30/9-B-44B, displayed in Fig. 5.33 and Fig. 5.34, shows a significant reduction in intergranular pore space within the band compared to the host rock. However, the grains and the grain boundaries are not easy to recognize in the SE-SEM image due to poor quality (Fig. 5.34b). It is therefore difficult to analyse the microstructures of this band. The average grain size within the band is 3.2 μm, the largest is 13.1 μm and the tiniest grain size is 0.7 μm. The apparent thickness of the deformation band varies between about 80-220 μm.

When seen through the optical microscope, the band is distinguished by its light yellowish colour compared to the darker green colour of the host rock, and the contact between the band and the host rock is gradual. The grains and the host rock to this band is of facies 2, however it appears similar to the host rock analysed in Fig. 5.16 and Fig. 5.18 of facies 4. Both facies are of chalk succession origin, and show evidence of re-deposition (see Tab. 1.2). The light deformation band in well 30/9-B-44 B could therefore be of same nature as the light deformation bands found in well 30/9-B-46 A, see Fig. 5.35.

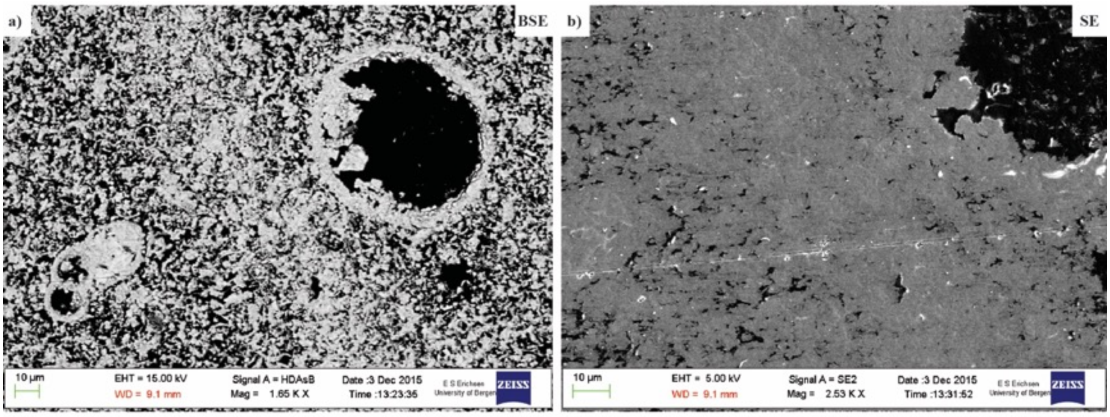

Figure 5.34: The light deformation found in well 30/9-B-44B. a) BSE-SEM image and b) SE-SEM image for comparison. The sample is of poor quality in the scale of more than 2 K magnification, as seen in b).

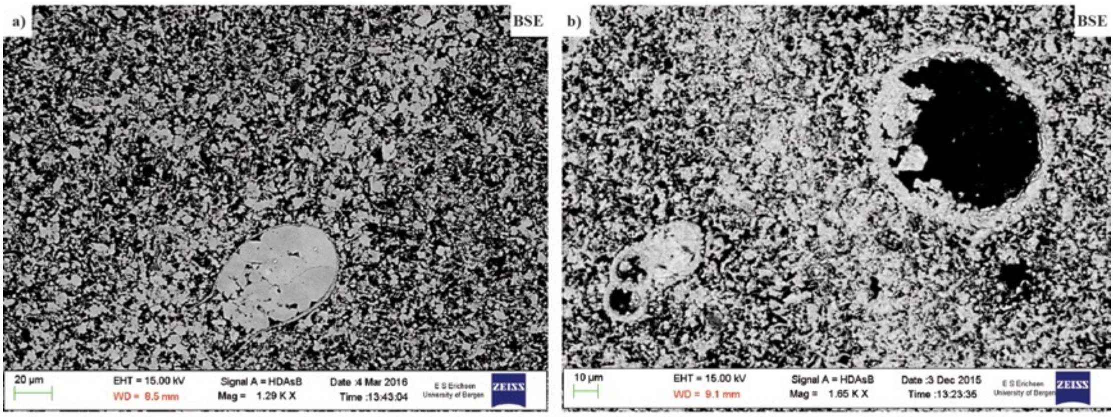

5.35: The light deformation band found at 4305.50 in well 30/9-B-44B could be compared with the light deformation bands found in well 30/9-B- 46A. Here the light deformation band found in thin section 4 at 3340.72 m MD in well 30/9-B46A, also seen in Fig. 5.27a), is shown in a). The deformation band in b) is tough more prominent than the deformation band in a).

The light deformation bands found in the cores are mainly at high angles to the bedding, the grains are aggregated by sutured grain boundaries. The aggregation of grains reduces the intergranular porosities within the band compared to the host rock. The kinematic and mechanism behind the aggregation of grains could be due to compaction of grains and pressure solution at the grain boundaries. Due to lack of markers, no shear movement is indicated, however, the alignment of grains and the orientation of the band being at high angle to the bedding, could indicate shear. These deformation bands could therefore be classified as solution compactive shear bands.

5.6.2.3 "Dark" deformation bands at high angle to bedding

Most of the "dark" deformation band located in PPL images where difficult to distinguish in both BSE and SE images. PPL images had to be used as references to locate the "dark" deformation bands in SEM images. The "dark" deformation band in Fig. 5.36 where possible to recognize due to the alignment of the grains. The "dark" deformation band in Fig. 5.36 has been highlighted by a grey tint of colour to distinguish the deformation band, the transition zone and the host rock. The core of the deformation band was interpreted to be the area with the highest density of aligned grains with high angle towards the stylolite. The deformation band is c. 62 µm in apparent thickness, and the transition towards the host rock is diffused. The average grain size is 4 µm, the smallest grain is 0,6 µm and the clay mineral is 24 µm. The deformation band have a planar geometry and the grains are angular, consists of both elongated with low sphericity and rounded grains with high sphericity. There are still 17 % intergranular porosity present in the deformation band. As shown in Fig. 5.27b, the deformation band in Fig. 5.36 is one of the diverging arm of the deformation band before its terminating against the stylolite

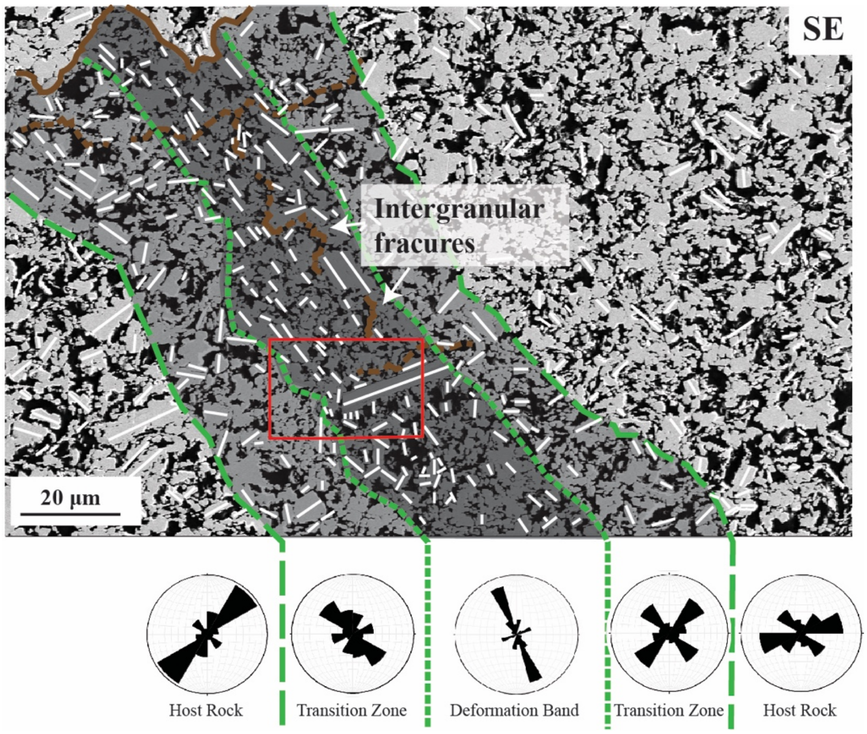

Figure 5.36: The alignment and the orientation to the grains are highlighted with white lines, and a grey coating is coloured on to illustrate the dark deformation band in this SE image. The deformation band is terminating against a stylolite indicated by the brown serrating line. The different zoning of the band is highlighted by the green stippled line. Rose diagrams were made to further display the division between the host rock, transition zone and the core of the deformation band, and illustrating that the orientation to the grain within the deformation band is at high angle to the orientation of the grains within the host rock.

The blue lines indicate sutured grain contacts (see section 4.3), suggesting chemical compaction and that intergranular pressure solution is present between the grain boundaries. This is especially visible around the clay mineral that is oriented perpendicular to the band, which is shown in Fig. 5.37b covered in micrite crystals and coccolith grains. Notice the rupture occurring on top of the clay minerals, highlighted by the red arrows, and the slight shear movement by the clusters of chalk grains, indicated by the red half arrows. Intergranular fractures were also observed within the deformation band, both subparallel and transvers to the deformation band (se Fig. 5.37a).

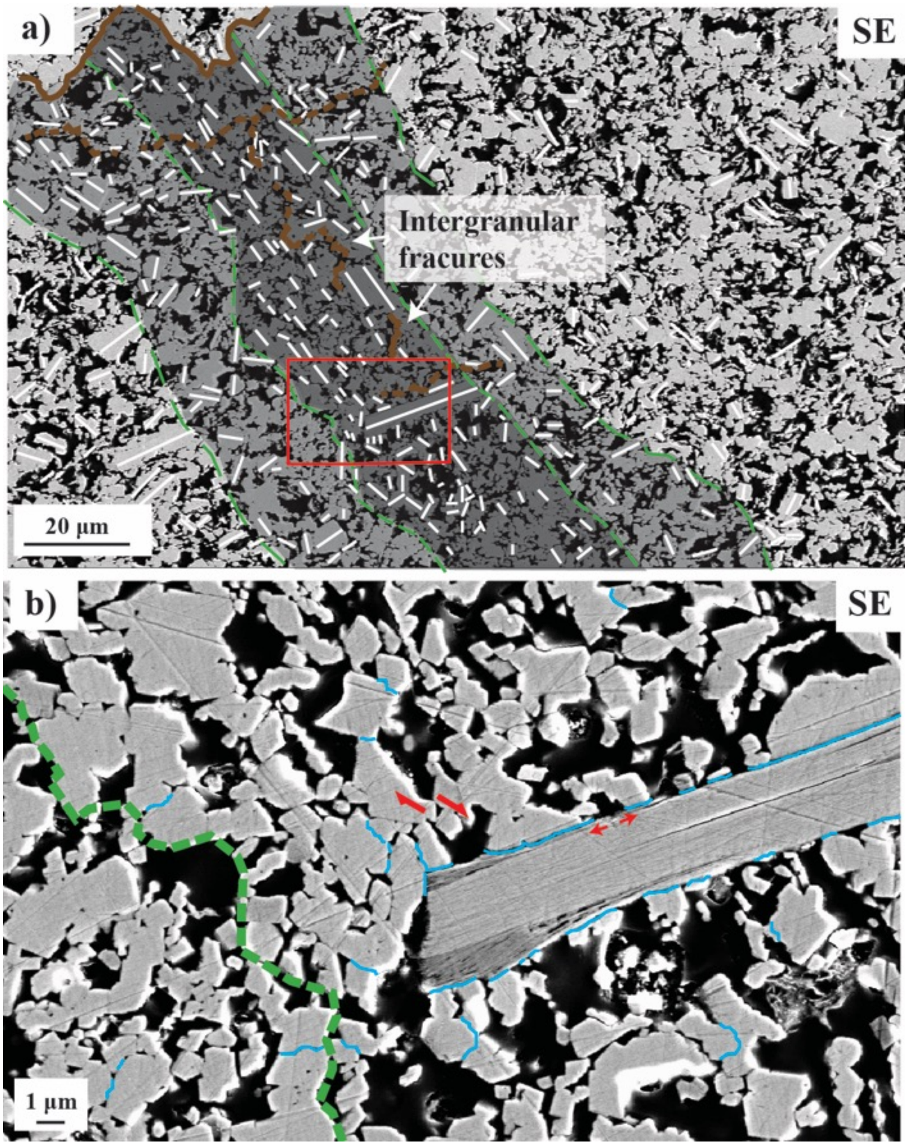

Figure 5.37: a) Intergranular fractures are seen within the deformation band in two orientations one subparallel to the stylolite the other subparallel to the deformation band, highlighted with spotted brown line. b) Several of the grains are sutured by the grain boundaries, especially the clay mineral is covered by chalk particles sutured to its boundary.

The thin section 12 at 3346.64 m MD in well 30/9-B-46A lack markers for the true way up, hence foraminiferas show parallelism and could indicate the orientation to bedding (Fig. 5.38). The deformation band is therefore interpreted to be orientated at a high angle to the bedding. The foraminiferas do not seem to be affected by the deformation band (Fig. 5.38), and the deformation band show no indication of cataclasis. This could be due to the solid shell framework and spherical geometry of the foraminiferas makes them less prone to crushing. Whereas more angular grains could be more affected by cataclasis (Rotevatn et al., in press). Since most of the coccoliths comprising the host rock might already have been broken up to the significant extent due to re-deposition and long-time compaction, it is difficult to use the coccoliths fragments and the micrite crystals as indicators for cataclasis.

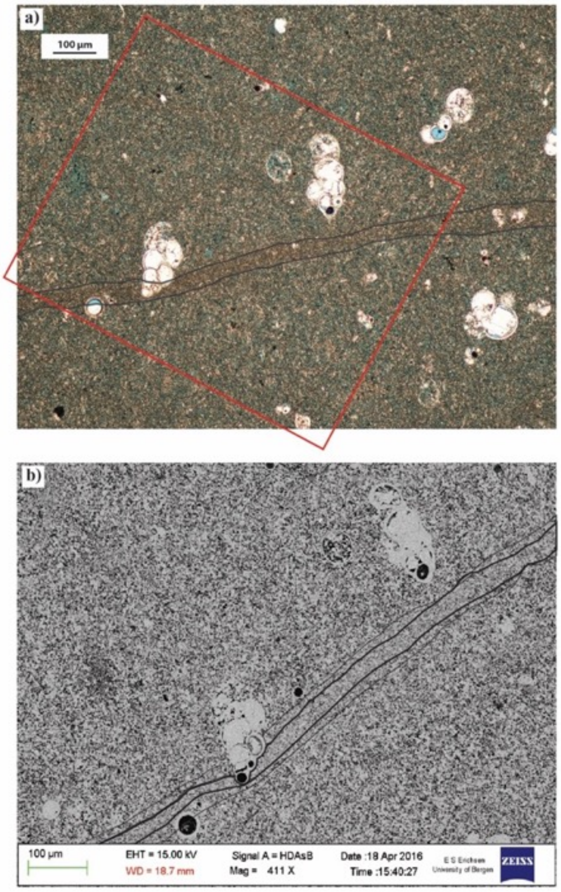

Figure 5.38: A dark deformation band shown in a) as a dark brown discontinuity in PPL image and in b) as a discontinuity with intergranular pore size reduction.

The “dark” and the “light” deformation bands with high angle to the bedding showed some similarities in both kinematic and mechanism. Both the “dark” and the “light” deformation bands where at high angle to the bedding and showed alignment of grains within the band and some minor indicator of shear movement was detected in Fig. 5.37. However, less grains are sutured or aggregated within the “dark” deformation band relative to the “light” deformation bands. Hence, cementation might be the reason for the aggregation in the “light” deformation band. Nevertheless, both the “light” and “dark” deformation bands appear to be of the same kinematic and mechanism, and they are therefore both classified as solution compactive shear bands.

5.6.2.4 Deformation band subparallel to bedding

The deformation bands in Fig. 5.39 show two main orientations, one being at high angle and the other is subparallel to bedding. The deformation band with high angle (60-70°) to the bedding terminates against the deformation bands subparallel to the bedding. The bed-parallel deformation band is featured in Fig. 5.39 c) and d). In Fig. 5.39d a tail of grain-size reduction is displayed. The average grain size is 2 μm, ranging from 0,2 μm to 7,27 μm. Aligned clay minerals are present within this tail and are indicated by the yellow lines. The deformation bands subparallel to the bedding has an apparent thickness of about 35-214 μm and the deformation bands with higher angle to the bedding varies in thicknesses between 50-285 μm. The contact between the deformation bands and the host rock, shown in Fig. 5.39b, is faint. Fig. 5.39a show two sets of zones of deformation bands subparallel to the bedding, separated by a distance of 1.1 cm, whereas the distance between the deformation bands with high angle to bedding is as small as c. 1.5 mm. Due to lack of markers or indication of shear, no offsets between the deformation bands has been detected. The bed-parallel deformation bands can be distinguished from the host rock by the darker brown colour relative to the greenish colour of host rock seen in PPL images. The deformation bands are otherwise hard to point out in both BSE and SE images.

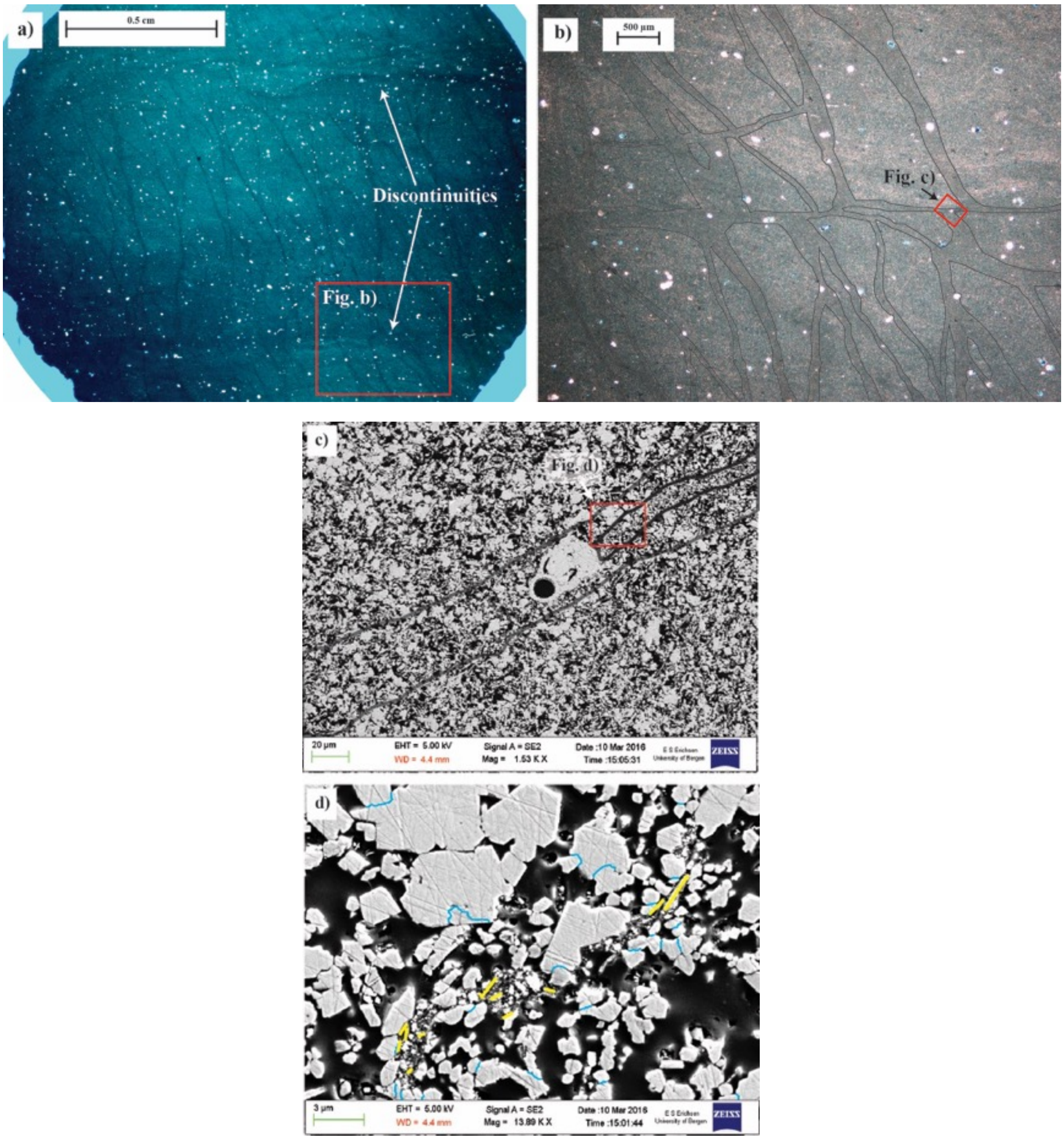

Figure 5.39: A dark deformation band subparallel to the bedding, shown and highlighted by dark lines in b) from thin section H32 at 3341.75 m MD in well 30/9-B-46A. At the location for c), a tail of smaller grains and aligned clay minerals are present highlighted by yellow lines in d). The grains surrounding and within the grain-size reduced tail show sutured grain boundaries indicated by the blue lines. The perpendicular dark deformation band highlighted in b) is not recognized in c) and is therefore not outlined.

The tail of grain size reduction observed resemble dissolution seam, due to the abundant of clay minerals and the sutured grain boundaries. The bed-parallel deformation bands are difficult to observe in SEM-images (see Fig. 5.39c), PPL-images can detect them as zones of strain similar to the solution compactive shear bands (see section 5.6.2.2 and 5.6.2.3). They are subparallel to the bedding and the stylolites, and due to the dissolution seems it could therefore be argued if these bed-parallel deformation bands could be kinematically related to the stylolites formation. The bed-parallel deformation bands are therefore classified as compaction bands. The classification and the interpretation of the deformation bands, will further be presented in the first part of Chapter 6 – Discussion.

6. Discussion

The main aim of this study has been to understand the kinematic and mechanical controls on developing the deformation bands in the Shetland chalk in the Oseberg Field. In the first section of this chapter will present the interpretations and classifications of the deformation bands described in section 5.6.2., whereas the second part will focus on the micromechanisms and kinematic evolution of the bands. Finally, the studied deformation bands will be set into to the larger-scale structural setting of the study area.

6.1 Interpretation and classification

The study of deformation bands in porous sandstones has been a field of research for several decades (e.g., Aydin, 1978, Aydin and Johnson, 1978, Aydin et al., 2006, Antonellini et al., 1994, Fossen et al., 2007, Rotevatn et al., 2007), deformation bands in carbonate rocks (Baud et al., 2000, Vajdova et al., 2004, Marchegiani et al., 2006, Micarelli et al., 2006, Tondi et al., 2006, Antonellini et al., 2008, Cilona et al., 2012, Rustichelli et al., 2012, Rotevatn et al., in press) and in particularly in chalk have only recently become a field of active research (Gaviglio et al., 2009, Kaminskaite et al., 2015, Wennberg et al., 2013). According to the latter, deformation bands in carbonates form due to pressure solution and disaggregation (e.g. granular flow), and cataclasis may occur as well.

Considering that the Shetland chalk is a post-rift unit deposited after the last major rift phase in the Mid to Late Jurassic (see section 2.2.2). It is debatable whether the deformation bands were formed in association with faulting, or by gravitational instabilities related to burial loading over pre-existing structures. The measured reduction in porosity within the studied deformation bands (see section 5.6.2.1) indicates that there has been compaction involved during their formation. Observation show that the maximum principal axis (σ_1) must have been oriented vertical to the bedding during the formation of the bands, therefore it could be argued that the stylolites developed simultaneously with the deformation bands. Extension fractures may have been developed afterwards during an uplift event, after the host rock became more cohesive (see section 3.2.3).

Based on the reduction in porosity, the kinematic (sensu Aydin et al., 2006) and the dominant deformation mechanisms (sensu Fossen et al., 2007), two different types of deformation bands are distinguished in this study (see section 5.6.2) and classified below.

6.1.1 Compaction band (CB)

The bed-parallel deformation bands (Fig. 5.39) are classified as compaction bands (CB) based on their orientation parallel to bedding, their reduction in porosity due to dissolution seams, and the fact that there is no evidence of shearing along the bands. The occurrence of dissolution seams could indicate kinematic relations to development of stylolites.

6.1.2 Solution compactive shear band (SCSB)

The deformation bands at high angles to the bedding are classified as solution compactive shear bands (SCSB) based on their orientation to the bedding and their abundance of sutured grain boundaries relative to the host rock. Indications of shear was difficult to detect due to lack of markers, however the grains show alignment parallel to the band and that could indicate shear movement has taken place.

6.2 Deformation mechanisms and kinematic evolution of the microstructures

Deformation bands have not been observed to cross-cut the stylolites, as suggested by Wennberg et al. (2013) (see section 3.3.4). The deformation bands rather show association to the stylolites by the bands diverging when they terminate against the stylolites (see section 5.6.2). In addition to the deformation bands, extension fractures where also observed in relation to stylolites (see section 5.6.1.1), similar to the stylolite-associated fractures found in the Tor Formation (see section 3.2.4). Fractures where identified as extension fractures or as irregular tortuous calcite veins terminating against the stylolites (Fig. 6.1). Stylolite where observed as potential baffle for fluid flow in Fig. 5.20 (see section 5.6.1.1).

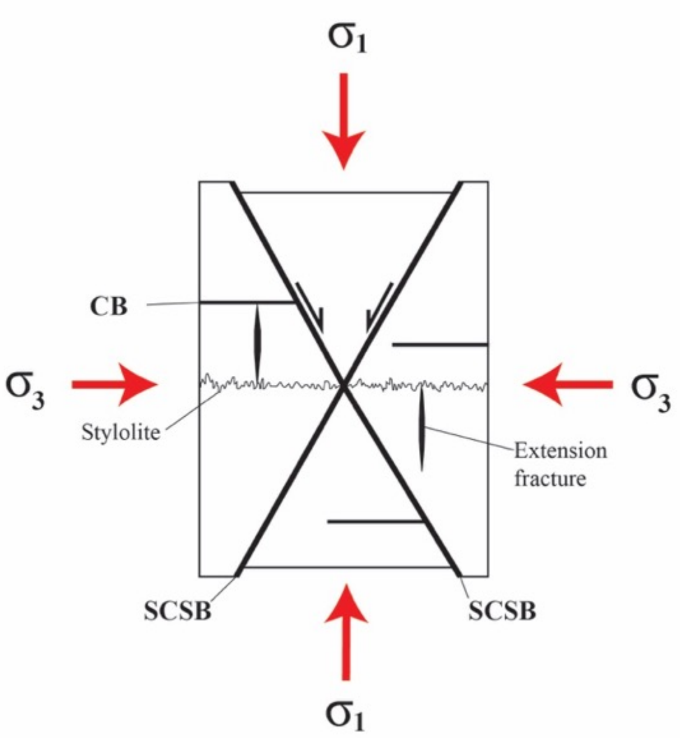

Figure 6.1: Conceptual illustration showing the spatial relationship between compaction bands (CB), stylolites, solution compaction shear bands (SCSB) and extension fractures. Modified from Fossen (2010) and Fossen et al. (2015).

“Healed fractures” also known as hairline discontinuities (see section 3.2.4) have been reported to show a reduction in porosity, and being exclusively found in intervals of redeposited chalk (Feazel, 1988). However, they have been classified as early fractures developing while the sediments were partly lithified, and later been “healed” by diagenetic dissolution and precipitation. The oil staining is therefore interpreted to be indications of flow of hydrocarbons before the diagenetic event (Agarwal et al., 1997) (see section 3.3.4). No evidence has been observed indicating that the hairline discontinuities initially have been fractures, or precipitation of calcite crystals “healing” the fracture. Disaggregation and pressure solution features are rather observed. This study would therefore argue, following with Wennberg et al. (2013), that the hairline discontinuities should be classified as deformation bands. However, extension fractures, veins and irregular calcite veins have been observed at the same microscale. This study can therefore not confirm whether or not all the hairline discontinuities observed in macroscale are deformation bands and not fracture related features.

Nevertheless, the orientation of the observed veins and fractures form the scanline (see section 5.4.3) show higher angle to the bedding than the hairline discontinuities on average. It could therefore be argued if “hairline fractures”, such as extension fractures, veins and irregular calcite veins could be distinguished from the deformation bands by the higher angle to the bedding. In addition, only irregular calcite veins show the distinct tortuous pattern (see section 5.6.1.3).

6.2.1 Compaction band (CB)

Natural pure compaction bands are rare in sandstones (Mollema and Antonellini, 1996, Fossen et al., 2015), and they seem restricted to granular rocks with a porosity of 30% or higher (Fossen et al., 2015, Tondi et al., 2006). Bed-parallel compaction bands in carbonates are however more abundant, and they are localized within the most porous layers. Previous authors on bed-parallel compaction bands in porous carbonate rocks deformed in the contractional regime, interpreted their formation to have formed during vertical loading due to the progressive burial of the sediments (Tondi et al., 2006, Rustichelli et al., 2012, Cilona et al., 2012).

The observed dissolution seam within the compaction band in Fig. 5.39, show that the grain size reduction has occurred solely by pressure solution process and the clay minerals within are subparallel with the bedding. The rest of the band has been difficult to recognize in the SEM-images, whereas the colouring difference between the band and the host rock is present in the PPL-images. It has therefore been concluded that the band is present, however, the dissolution seam is the only obvious mechanical alteration observed in the band compared to the host rock. Tondi et al. (2006) argue that a mechanical transition in deformation band processes to pressure solution developing stylolites could be possible due to their similarities in kinematic (see section 3.34).

6.2.2 Solution compactive shear bands (SCSB)

Compactive shear bands at a low angle to the maximum principal stress axis (σ_1) have both been observed in contractional (Fossen et al., 2015, Tondi et al., 2006) and extensional

(Rotevatn et al., in press) setting. Tondi et al. (2006) also argue that compactive shear bands with no stylolites or cataclasis represent the simplest fundamental shear structure formed in porous carbonate grainstones. The “dark” deformation bands seen in PPL-images (see Fig. 5.27) where not easy to recognize in SEM-images. However, the abundance of sutured grain boundaries in both the “light” and the “dark” deformation bands (see section 5.6.2.1 and 5.6.2.2) show that the deformation bands have been affected by pressure solution. Nevertheless no dissolution seams have been observed within the bands.

Very little differences in the mechanisms was found between the “light” and “dark” deformation bands at high angle to the bedding. However, the colour difference where observed due to more clustering of grains within the “light” deformation bands compared to the “dark” deformation bands. The “light” deformation bands shows abundance of aggregation of grains sutured together. The “dark” deformation bands shows abundance of sutured grain boundaries and some, but less clustering compared to the “light” deformation bands. This colour difference could be due to fluid flowing through the “light” deformation bands and precipitation (e.g. Gaviglio et al., 2009). The fluids must have been baffled by the stylolites to follow certain paths. Due to the small scale of the broken coccoliths and the micrite crystals, cementation at this level has shown to be difficult to detect.

Both the “light” and the “dark” deformation bands show preferential alignment of elongated grains being parallel to the band (se Fig. 5.32 and 5.36), indicating that shear and compaction where accommodated by granular flow mechanisms and that they are both kinematically similar.

6.3 Tectonic controls on development

Based on the results mentioned above (see section 6.1 and 6.2), three different hypotheses on the tectonic controls developing the deformation bands would be outlined in the following. The first hypothesis is based on the Early Cretaceous reactivation of major fault (see section 2.1.1) and that the extension is the influencing tectonic (6.3.1). The second hypothesis look at the development of a monocline due to upward propagation of reactivated faults, and associating deformation bands (6.3.2). The last hypothesis consider burial compaction and differential compaction as the controlling processes to developing the deformation bands (6.3.3).

6.3.1 Early Cretaceous rifting

Deformation bands are particularly frequent in fault damage zones (see section 3.1), and are expected to be formed due to development of faults (Aydin and Johnson, 1978, Shipton and Cowie, 2003) (see section 3.3.3). In addition, deformation bands have already been observed and interpreted to be an important feature in developing faults in chalk (Gaviglio et al., 2009) (see section 3.3.4). Deformation bands are in general more distributed in contractional regime compared to the extensional regime, due to the difference in stress directions (Soliva et al., 2016). However, spatial distribution of deformation band sets have been observed in extensional settings within relay ramps (Rotevatn et al., 2007) or where the lithological contrast delayed the propagation of shear bands in sandstone (Schultz and Fossen, 2002). Soliva et al. (2016) suggests that the remote tectonic stress in general has a stronger influence on band distribution than local stress, such as developed by reactivation of inherited faults, layering or fault segmentation.

Deformation bands found in extensional regimes are typically of compactive shear bands and shear bands clustered around and defining the damage zone to the faults (see section 3.1). The shear bands are therefore naturally oriented in clusters subparallel to the fault with centimetres to decimetres scale of displacement (Soliva et al., 2016). The frequency of deformation bands tends to act as a function of the distance to the fault core (Schueller et al., 2013) (see section 3.1).

Pressure solution has been reported to be more abundant in contractional regimes, where the mechanism can develop by burial compression, and less important to facilitate cataclasis in an extensional regime (Rotevatn et al., in press) (see section 3.3.4). whereas this might be true, the evidence shows that the deformation bands generally lacked indications for shear, such as cataclasis and offset was not observed due to lack of markers (see section 5.6.2).

During Early Cretaceous, major faults where subjected to reactivation due to thermal subsidence (see section 2.1.1). The area was also later subjected to uplift and erosion during

Oligocene, however, the area did not undergo salt tectonic such as in the Ekofisk Field area (Surlyk et al., 2003). One fault was encountered in the core from the horizontal well 30/9-B-24B and analysed by Wennberg et al. (2013). The fault has a N-S strike and a dip of about 54-60°, trending with the major faults in the area such as Oseberg and Brage faults (see section 2.1.1).

6.3.2 Monoclinal

As already mentioned (see section 2.1.1), reactivation of major faults occurred during Cretaceouse due to thermal subsidence. Reactivation and upwards propagating of a fault can develop a monocline in the post-rift sedimentary sequence deposits, in the form of a broad flexure (Sharp et al., 2000). With increasing fault displacement, the monoclonal limb steepens and tilts towards the hanging wall (Fig. 6.2). Presence of high-angle to locally reverse secondary faults and fractures occurs in the hanging-wall during the upward-propagation of a normal fault and formation of the monocline (see Fig. 6.2d). Continued fault propagation would lead to half-graben geometry (Sharp et al., 2000).

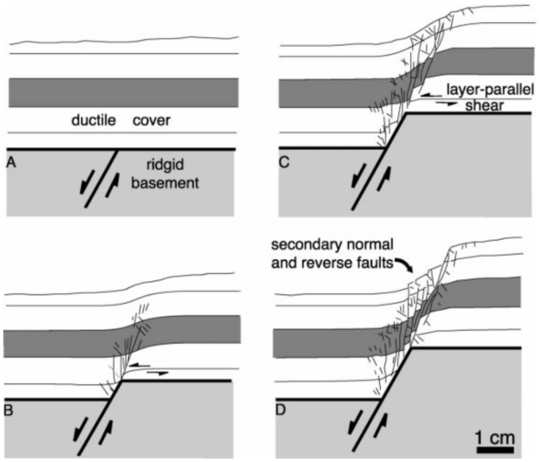

Figure 6.2: Schemtically illustration of an experimental clay model of extensional propagation of a monocline. From Sharp et al. (2000).

Monocline also known as fault-propagation fold are commonly represented at the tip of a surface-breaking normal fault (Walsh and Watterson, 1987, Schlische, 1995). The monocline is defined by horizontal to increasingly inclined strata in the footwall, and a relatively wide

faulted zone of steeply dipping to locally overturned strata with a strongly asymmetric hanging wall syncline (Sharp et al., 2000).
Zuluaga et al. (2014) reports nucleation and growth of progressive and complex deformation band arrays developing during the growth of a monocline. The development of strain in a monocline during an upward propagation of a normal fault was by Zuluaga et al. (2014) subdivided into 4 following stages: i) nucleation of bed-parallel deformation bands at lithology contrast or pre-weaknesses in the bedding. ii) At 25° dip of the forelimb, strain increases and deformation bands develops into conjugate sets, transecting the bedding and the former bed-parallel deformation bands as folding progresses. iii) Strain continues as the limb exceeds 32° in dip , rotates all pre-existing deformation bands and the deformation bands increase in thickness and number. iv) The final stage, clusters of deformation bands aggregates at the top of the unit, whereas slip surfaces develops at the base of the formation during flexural slip at about 65° in dip of the forelimb.

Both the Early Cretaceous and monocline hypotheses would explain formations of shear enhanced deformation bands, however, these hypotheses would not explain the deformation bands association to bed-parallel stylolites. Reactivations of the major faults during Cretaceous is thought to have been developed due to compaction and thermal subsidence (see section 2.1.1).

6.3.3 Differential compaction

The chalk was deposited as a pelagic ooze with primary porosity of about 60-80% (Fabricius, 2003), before being redeposited by mass flows and compacted due to burial to comprise a secondary porosity of about 20-40% (Wennberg et al., 2013). Between the tubular or platy fragmented coccoliths and micrite crystals, the chalk comprises of very small pores (1-10 μm, see section 5.5), however it constitute to a high effective porosity even after compaction (Surlyk et al., 2003).

Hairline fractures are interpreted to be developed early as closed fractures filled with matrix of coccolith debris, and are related to dewatering of the chalk after mechanical compaction and consolidation (Surlyk et al., 2003, Agarwal et al., 1997) (see section 3.2.4). Stylolite-associated fractures are interpreted to occur in tight chalk in anastomosing network with some infilled by calcite (Surlyk et al., 2003, Agarwal et al., 1997). Solution compactive bands and bed-parallel stylolites have been reported as structures developing in response to overburden pressure (Tondi et al., 2006). Most of the hairline discontinuities have in this study been observed in abundant within in chalk layers of facies 2 and 4 – redeposited chalk by turbidites and mass flows (see Tab. 1.2).

Initially, sediments deposited in a basin consist basically of grain matrix and interstitial fluid, as the sediments progressively accumulate the underlying strata are subjected to an increase in overburden pressure. In permeable layers from which the pore fluid is free to escape, no fluid pressure develops. Increase in overburden pressure is a function of depth and in the case of the aforementioned, the pore space is reduced and the grain matrix is compacts (Cowie and Karner, 1990). If that is not the case, and the fluid is trapped between non-permeable layers, the fluid pressure increases and the layer are subjected to overpressure (Cowie and Karner, 1990, Fossen, 2010). An increase in pore fluid pressure reduces the effective stress distributed over the grain contact and the compaction of the porous rock is not entirely a function of depth. High overpressure could therefore indicate that the porous rock is less compacted and lithified then expected from the burial depth. The overpressured layers would therefore be less consolidated and high pore pressure could lead to deformation of the porous rock (Fossen, 2010).

During burial diagenesis, the chalk is overlain by sediments, mechanical compaction occurs by translation and breakage of grains to reduce porosity and permeability (see section 3.1). At about 1 m of burial depth, mechanical compaction begins to dehydrate the rock and the strain is concentrated at grain contacts. The overburden pressure can result in mechanical failure at grain boundaries, by plastic deformation of grains and grain crushing. During mechanical compaction, porosity of the porous chalk is reduced to about 40% (Flügel, 2004).

When the pressure of compaction leads to dissolution of grain boundaries (see section 3.2.3), mechanical compaction is gradually replaced by chemical compaction. The porosity and permeability of the chalk is further reduced and structures made by pressure solution such as dissolution seams, stylolites and shear fractures are produced. Chemical compaction for calcite start around 300 m of burial depth and pore-water is of prime importance (see section

3.2.5) (Flügel, 2004). The greater the degree of oversaturated pore water with dissolved calcite, the greater must the overburden pressure be to cause pressure solution (Weyl, 1959). Oil and organic films between the grains could also prevent the formation of stylolites. Chemical compaction depends on burial depth and vertical stress caused by overburden pressure results in preferential solution (Flügel, 2004).

Progressive burial and deposition of overburden sediments results in compaction, decrease in porosity and increase in the density of the overlaying sediments. Lateral variation in thickness of a given layer, or contrast in the amount of vertical compaction develops differential compaction within the given layer of sediments (Pluijm and Marshak, 2004). The thickness of a sedimentary sequence may decrease by c. 55% due to compaction, and that would apply more compaction where the sediment sequence is thickest compared to the thinner parts. In addition the magnitude of the displacement decrease is dependent on lithology, whereas displacement loss due to compaction increase with the increase of shale percentage (sensu Taylor et al., 2008).

It is suggested by Wennberg et al. (2013) that the open anticlinal of the Cretaceous succession over the Oseberg Field was developed due to differential compaction and not primarily on deposition (see section 5.1.1). The structural depth map in Fig. 5.2 show that the studied well 30/9-B-46A is located in the greenest area, which is where the Cretaceous succession is thinnest and has undergone the most compaction. The differential compaction would have applied even more strain to the bedding than burial compaction alone. Based on the mentioned, the deformation bands described in this study is interpreted to have been developed due to burial compaction and differential compaction.

7. Conclusions

This study has attempted to describe and characterize the geometry, microstructure and deformation mechanisms associated with deformation bands present in the Maastrichtian to Danian chalk above the Oseberg Field. From the work presented in this study, the following conclusions are drawn:

- Two types of deformation bands have been described and classified in chalk in this study: bed-parallel compaction bands (CBs), and solution-compactive shear bands (SCSBs) at high angle to the bedding.
- The cross-cutting relations show that the deformation bands formed more or less contemporaneously with the stylolites and under the same overall stress regime.
- Extension fractures and veins are also observed in association with stylolites.
- The image-based porosity analysis showed that the porosity within the deformation bands is significantly reduced as compared to the host rock.
- The microstructural analysis done on the studied deformation bands exposed evidence of pressure solution and disaggregation of grains as the dominant deformation mechanisms.
- It is suggested that the deformation bands evolved during burial and differential compaction, where the maximum stress axis (σ_1) was oriented vertical to the bedding.
- Both deformation bands and extension fractures seem to be present as “hairline discontinuities”
- The “hairline discontinuities” could not be define as deformation bands or fractures based on macroscopic observations. Microscopic analysis has to be done to do separate the two different microstructures.

8. Implications, limitations and future work

8.1 Implications of the study

This study has given, new awareness regarding the occurrence, geometry and the deformation mechanism developing deformation bands in porous chalk. Structural analysis and microscopic investigations have for the first time improved the knowledge of compaction bands (CBs) and solution compactive shear bands (SCSBs) development within chalk.

Most deformation bands represents narrow tabular zones with reduced porosity and permeability relative to the host rock, and may act as baffles, barrier or conduits for fluid flow in reservoir settings (e.g. Antonellini and Aydin, 1994, Hesthammer and Fossen, 1999) (see section 3.1 and 3.3.5). Deformation bands dominated by granular flow could have little influence on permeability, while cataclastic and/or pressure solution dominated deformation bands show a slightly more influence on the permeability (see section 3.3.5). In this study, no indication of cataclasis was found within the deformation bands, and the grain size reduction have occurred solely by disaggregation of grains and pressure solution mechanisms (see section 6.2.2). Due to the difference in clustering of grains (discussed in section 6.2.2) observed within the solution compactive shear bands. It is suggested by this study that the fluids have been baffled by the stylolites and that it is the stylolites structures that controls the conduits of fluid flow, with some minor influence by the deformation bands.

8.2 limitations and future work

The porosity was measured by the ImageJ software, which uses binary 2D SEM images of the thin section to calculate the porosity, this may lead to some degree of underestimation of the porosity. The threshold is done manually and could encounter some complications such as human errors.

10 low resolution μCT-scans where done at the facility of Statoil in Bergen, unfortunately the hard-driver to the CT-machine's main computer broke down. With the main computer did also the realization program go and the 10 μCT-scans where never realized. Wennberg et al. (2013) managed to resolve deformation bands in chalk with a thickness down to about 300 μm with μCT-scans. It would therefore be of interest to do to more μCT-scans to resolve more deformation bands to map out the distribution in 3D.

There was done a study on the topology with the software ArcMap 10.3 to the hairline discontinuities highlighted in Fig. 5.9c (see appendix III). The network image in Fig. 5.10 where made from the topology measurements. The fractures and the deformation bands could not be distinguished on the macroscale by this study (see section 6.1), therefore the data were not further used. It would however, be of interest if future studies of topology on different types of deformations bands could make it possible to use topology as a measurement to distinguish different deformation bands. Or, to use topology to calculate the network differences of the deformation bands within the the same facies.

The study was limited to one well, more samples from the chalk in well 30/9-B-44B would therefore be of interest for future study. The exact location of the wells regarding the regional setting was given at high uncertainties to this study, due to confidentiality. More detailed information on the locations of the wells would therefore be of interest to interpret the tectonic controls on the development of the deformation bands in more details.
For future work, grain-size distribution (e.g. Cilona et al., 2012) and grain to matrix measurements (e.g. Cilona et al., 2012, Tondi, 2007) within the deformation bands would be of interest, to better evaluate the micromechanism involved during the development of the deformation bands.

There are few published papers on outcrop studies of deformation bands in chalk. Therefore, more field-based studies would be of great importance for the understanding of distribution and growth of deformation bands in porous chalk.

Agarwal, B., Allen, L. & Farrell, H. 1997. Ekofisk Field reservoir characterization: mapping permeability through facies and fracture intensity. *SPE Formation Evaluation,* 12**,** 227-234.

Agosta, F., Alessandroni, M., Tondi, E. & Aydin, A. 2010. Oblique normal faulting along the northern edge of the Majella Anticline, central Italy: inferences on hydrocarbon migration and accumulation. *Journal of Structural Geology,* 32**,** 1317-1333.

Aharonov, E. & Katsman, R. 2009. Interaction between pressure solution and clays in stylolite development: Insights from modeling. *American Journal of Science,* 309**,** 607-632.

Andrews, L. M. & Railsback, L. B. 1997. Controls on stylolite development: morphologic, lithologic, and temporal evidence from bedding-parallel and transverse stylolites from the US Appalachians. *The Journal of Geology***,** 59-73.

Antonellini, M. & Aydin, A. 1994. Effect of faulting on fluid flow in porous sandstones: petrophysical properties. *AAPG bulletin,* 78**,** 355-377.

Antonellini, M., Cilona, A., Tondi, E., Zambrano, M. & Agosta, F. 2014a. Fluid flow numerical experiments of faulted porous carbonates, Northwest Sicily (Italy). *Marine and Petroleum Geology,* 55**,** 186-201.

Antonellini, M., Petracchini, L., Billi, A. & Scrocca, D. 2014b. First reported occurrence of deformation bands in a platform limestone, the Jurassic Calcare Massiccio Fm., northern Apennines, Italy. *Tectonophysics,* 628**,** 85-104.

Antonellini, M., Tondi, E., Agosta, F., Aydin, A. & Cello, G. 2008. Failure modes in deep-water carbonates and their impact for fault development: Majella Mountain, Central Apennines, Italy. *Marine and Petroleum Geology,* 25**,** 1074-1096.

Antonellini, M. A., Aydin, A. & Pollard, D. D. 1994. Microstructure of deformation bands in porous sandstones at Arches National Park, Utah. *Journal of structural geology,* 16**,** 941-959.

Antonellini, M. A. & Pollard, D. D. 1995. Distinct element modeling of deformation bands in sandstone. *Journal of structural Geology,* 17**,** 1165-1182.

Aydin, A. 1978. Small faults formed as deformation bands in sandstone. *Pure and Applied Geophysics,* 116**,** 913-930.

Aydin, A., Borja, R. I. & Eichhubl, P. 2006. Geological and mathematical framework for failure modes in granular rock. *Journal of Structural Geology,* 28**,** 83-98.

Aydin, A. & Johnson, A. M. 1978. Development of faults as zones of deformation bands and as slip surfaces in sandstone. *Rock Friction and Earthquake Prediction.* Springer.

Aydin, A. & Johnson, A. M. 1983. Analysis of faulting in porous sandstones. *Journal of Structural Geology,* 5**,** 19-31.

Badley, M., Price, J., Dahl, C. R. & Agdestein, T. 1988. The structural evolution of the northern Viking Graben and its bearing upon extensional modes of basin formation. *Journal of the Geological Society,* 145**,** 455-472.

Badley, M. E., Egeberg, T. & Nipen, O. 1984. Development of rift basins illustrated by the structural evolution of the Oseberg feature, Block 30/6, offshore Norway. *Journal of the Geological Society,* 141**,** 639-649.

Ballas, G., Fossen, H. & Soliva, R. 2015. Factors controlling permeability of cataclastic deformation bands and faults in porous sandstone reservoirs. *Journal of Structural Geology,* 76**,** 1-21.

Bathurst, R. G. 1995. Burial diagenesis of limestones under simple overburden; stylolites, cementation and feedback. *Bulletin de la Société géologique de France,* 166**,** 181-192.

Baud, P., Schubnel, A. & Wong, T. F. 2000. Dilatancy, compaction, and failure mode in Solnhofen limestone. *Journal of Geophysical Research: Solid Earth,* 105**,** 19289-19303.

Bons, P. D., Elburg, M. A. & Gomez-Rivas, E. 2012. A review of the formation of tectonic veins and their microstructures. *Journal of Structural Geology,* 43**,** 33-62.

Borg, I., Friedman, M., Handin, J. & Higgs, D. V. 1960. Experimental deformation of St. Peter sand: a study of cataclastic flow. *Geological Society of America Memoirs,* 79**,** 133-192.

Brekke, H. & Olaussen, S. 2006. Høyt hav og lave horisonter: Kritt, Jordas drivhustid; 146-66 Ma. *In:* RAMBERG, I. B., BRYHNI, I. & NØTTVEDT, A. (eds.) *Landet blir til: Norges geologi.* Trondheim: Norsk Geologisk Forening (NGF).

Byrd, W. 1975. Geology of the Ekofisk field, offshore Norway. *Petroleum and the Continental Shelf of Northwest Europe,* 1**,** 439-445.

Cashman, S. & Cashman, K. 2000. Cataclasis and deformation-band formation in unconsolidated marine terrace sand, Humboldt County, California. *Geology,* 28**,** 111-114.

Choquette, P. W. & Pray, L. C. 1970. Geologic nomenclature and classification of porosity in sedimentary carbonates. *AAPG bulletin,* 54**,** 207-250.

Cilona, A., Baud, P., Tondi, E., Agosta, F., Vinciguerra, S., Rustichelli, A. & Spiers, C. J. 2012. Deformation bands in porous carbonate grainstones: Field and laboratory observations. *Journal of Structural Geology,* 45**,** 137-157.

Coward, M., Dewey, J., Hempton, M. & Holroyd, J. 2003. The millennium atlas: Petroleum geology of the central and northern North Sea. *Tectonic Evolution, Geological Society, London***,** 17-33.

Cowie, P. A. & Karner, G. D. 1990. Gravity effect of sediment compaction: examples from the North Sea and the Rhine Graben. *Earth and Planetary Science Letters,* 99**,** 141-153.

De Boer, R. 1977. Stability of Mg-Ca carbonates. *Geochimica et Cosmochimica Acta,* 41**,** 265-270.

Deegan, C. T. & Scull, B. J. 1977. *A standard lithostratigraphic nomenclature for the Central and Northern North Sea*, HMSO.

Du Bernard, X., Eichhubl, P. & Aydin, A. 2002. Dilation bands: A new form of localized failure in granular media. *Geophysical Research Letters,* 29.

Dunham, R. J. 1962. Classification of carbonate rocks according to depositional textures.

Ebner, M., Toussaint, R., Schmittbuhl, J., Koehn, D. & Bons, P. 2010. Anisotropic scaling of tectonic stylolites: A fossilized signature of the stress field? *Journal of Geophysical Research: Solid Earth,* 115.

Fabricius, I. L. 2003. How burial diagenesis of chalk sediments controls sonic velocity and porosity. *AAPG bulletin,* 87**,** 1755-1778.

Fabricius, I. L. 2007. Chalk: composition, diagenesis and physical properties. *Geological Society of Denmark. Bulletin,* 55**,** 97-128.

Færseth, R. 1996. Interaction of Permo-Triassic and Jurassic extensional fault-blocks during the development of the northern North Sea. *Journal of the Geological Society,* 153**,** 931-944.

Færseth, R., Gabrielsen, R. & Hurich, C. 1995. Influence of basement in structuring of the North-Sea basin, offshore southwest Norway. *Norsk Geologisk Tidsskrift,* 75**,** 105-119.

Færseth, R. & Ravnås, R. 1998. Evolution of the Oseberg fault-block in context of the northern North Sea structural framework. *Marine and Petroleum Geology,* 15**,** 467-490.

Feazel, C. T. 1988. Chalk from the Ekofisk area, North Sea: nannofossils+ micropores= giant fields.

Ferreira, T. & Rasb, W. 2012. ImageJ user guide.

Fisher, Q. & Knipe, R. 2001. The permeability of faults within siliciclastic petroleum reservoirs of the North Sea and Norwegian Continental Shelf. *Marine and Petroleum Geology,* 18**,** 1063-1081.

Fletcher, R. C. & Pollard, D. D. 1981. Anticrack model for pressure solution surfaces. *Geology,* 9**,** 419-424.

Flügel, E. 2004. *Microfacies Data: Fabrics*, Springer.

Folk, R. L. 1962. Spectral subdivision of limestone types.

Folkestad, A., Odinsen, T., Fossen, H. & Pearce, M. A. 2014. Tectonic influence on the Jurassic sedimentary architecture in the northern North Sea with focus on the Brent Group. *From Depositional Systems to Sedimentary Successions on the Norwegian Continental Margin***,** 389-415.

Fossen, H. 2010. *Structural geology*, Cambridge University Press.

Fossen, H., Dallman, W. & Andresen, A. 2008. The mountain chain rebounds and founders. The Caledonides are worn down: 405–359 million years. *The making of a land. Geology of Norway***,** 232-259.

Fossen, H. & Hesthammer, J. 1997. Geometric analysis and scaling relations of deformation bands in porous sandstone. *Journal of Structural Geology,* 19**,** 1479-1493.

Fossen, H., Johansen, T. E. S., Hesthammer, J. & Rotevatn, A. 2005. Fault interaction in porous sandstone and implications for reservoir management; examples from southern Utah. *AAPG bulletin,* 89**,** 1593-1606.

Fossen, H., Schultz, R. A., Shipton, Z. K. & Mair, K. 2007. Deformation bands in sandstone: a review. *Journal of the Geological Society,* 164**,** 755-769.

Fossen, H., Schultz, R. A. & Torabi, A. 2011. Conditions and implications for compaction band formation in the Navajo Sandstone, Utah. *Journal of Structural Geology,* 33**,** 1477-1490.

Fossen, H., Zuluaga, L. F., Ballas, G., Soliva, R. & Rotevatn, A. 2015. Contractional deformation of porous sandstone: Insights from the Aztec Sandstone, SE Nevada, USA. *Journal of Structural Geology,* 74**,** 172-184.

Foster, P. & Rattey, P. The evolution of a fractured chalk reservoir: Machar Oilfield, UK North Sea. Geological Society, London, Petroleum Geology Conference series, 1993. Geological Society of London, 1445-1452.

Gabrielsen, R. H., Kyrkjebø, R., Faleide, J. I., Fjeldskaar, W. & Kjennerud, T. 2001. The Cretaceous post-rift basin configuration of the northern North Sea. *Petroleum Geoscience,* 7**,** 137-154.

Gaviglio, P., Bekri, S., Vandycke, S., Adler, P., Schroeder, C., Bergerat, F., Darquennes, A. & Coulon, M. 2009. Faulting and deformation in chalk. *Journal of structural geology,* 31**,** 194-207.

Gawthorpe, R. & Leeder, M. 2000. Tectono-sedimentary evolution of active extensional basins. *Basin Research,* 12**,** 195-218.

Geus 2010. Oseberg Field: Shetland Group Core Description. Well 30/9-B-46A, core 1. *Danmarks og Grønlands Geologiske Undersøgelse Rapport 2010/37*.

Geus 2011. Oseberg Field: Shetland Group Core Description. Well 30/9-B-44B, core1,2. *Danmarks og Grønlands Geologiske Undersøgelse Rapport 2011/99*.

Gibson, R. G. 1998. Physical character and fluid-flow properties of sandstone-derived fault zones. *Geological Society, London, Special Publications,* 127**,** 83-97.

Harper, T. & Lundin, E. 1997. Fault seal analysis: reducing our dependence on empiricism. *Norwegian Petroleum Society Special Publications,* 7**,** 149-164.

Heeremans, M. & Faleide, J. I. 2004. Late Carboniferous-Permian tectonics and magmatic activity in the Skagerrak, Kattegat and the North Sea. *Geological Society, London, Special Publications,* 223**,** 157-176.

Helland-Hansen, W., Ashton, M., Lømo, L. & Steel, R. 1992. Advance and retreat of the Brent delta: recent contributions to the depositional model. *Geological Society, London, Special Publications,* 61**,** 109-127.

Hesthammer, J. & Fossen, H. 1999. Evolution and geometries of gravitational collapse structures with examples from the Statfjord Field, northern North Sea. *Marine and Petroleum Geology,* 16**,** 259-281.

Hesthammer, J. & Fossen, H. 2000. Uncertainties associated with fault sealing analysis. *Petroleum Geoscience,* 6**,** 37-45.

Hooke, R. L. & Iverson, N. R. 1995. Grain-size distribution in deforming subglacial tills: role of grain fracture. *Geology,* 23**,** 57-60.

Hubbert, M. K. & Rubey, W. W. 1959. Role of fluid pressure in mechanics of overthrust faulting I. Mechanics of fluid-filled porous solids and its application to overthrust faulting. *Geological Society of America Bulletin,* 70**,** 115-166.

Isaksen, D. & Tonstad, K. 1989. *A revised Cretaceous and Tertiary lithostratigraphic nomenclature for the Norwegian North Sea*, Norwegian Petroleum Directorate.

Johansen, T. E. S. & Fossen, H. 2008. Internal geometry of fault damage zones in interbedded siliciclastic sediments. *Geological Society, London, Special Publications,* 299**,** 35-56.

Johansen, T. E. S., Fossen, H. & Kluge, R. 2005. The impact of syn-faulting porosity reduction on damage zone architecture in porous sandstone: an outcrop example from the Moab Fault, Utah. *Journal of Structural Geology,* 27**,** 1469-1485.

Kaminskaite, I., Fisher, Q. & Grattoni, C. Deformation Bands in Chalk and Their Impact on Fluid Flow-An Example from Pegwell Bay, Kent. Fourth International Conference on Fault and Top Seals, 2015.

Karig, D. & Lundberg, N. 1990. Deformation bands from the toe of the Nankai accretionary prism. *Journal of Geophysical Research: Solid Earth,* 95**,** 9099-9109.

Knipe, R., Fisher, Q., Jones, G., Clennell, M., Farmer, A., Harrison, A., Kidd, B., Mcallister, E., Porter, J. & White, E. 1997. Fault seal analysis: successful methodologies, application and future directions. *Norwegian Petroleum Society Special Publications,* 7**,** 15-38.

Li, Y. & Schmitt, D. R. 1998. Drilling-induced core fractures and in situ stress. *Journal of Geophysical Research: Solid Earth,* 103**,** 5225-5239.

Lind, I. Stylolites in chalk from leg 130, Ontong Java Plateau. Proceedings of the Ocean Drilling Program, scientific results, 1993. 445-451.

Liteanu, E., Spiers, C. & De Bresser, J. 2013. The influence of water and supercritical CO 2 on the failure behavior of chalk. *Tectonophysics,* 599**,** 157-169.

Lothe, A., Gabrielsen, R., Hagen, N. B. & Larsen, B. 2002. An experimental study of the texture of deformation bands: effects on the porosity and permeability of sandstones. *Petroleum Geoscience,* 8**,** 195-207.

Lucas, S. E. & Moore, J. C. 1986. Cataclastic deformation in accretionary wedges: Deep Sea Drilling Project Leg 66, southern Mexico, and on-land examples from Barbados and Kodiak Islands. *Geological Society of America Memoirs,* 166**,** 89-104.

Mair, K., Main, I. & Elphick, S. 2000. Sequential growth of deformation bands in the laboratory. *Journal of Structural Geology,* 22**,** 25-42.

Marchegiani, L., Van Dijk, J., Gillespie, P., Tondi, E. & Cello, G. 2006. Scaling properties of the dimensional and spatial characteristics of fault and fracture systems in the Majella Mountain, central Italy. *Geological Society, London, Special Publications,* 261**,** 113-131.

Matthäi, S., Aydin, A., Pollard, D. & Roberts, S. 1998. Numerical simulation of departures from radial drawdown in a faulted sandstone reservoir with joints and deformation bands. *Geological Society, London, Special Publications,* 147**,** 157-191.

Micarelli, L., Benedicto, A. & Wibberley, C. 2006. Structural evolution and permeability of normal fault zones in highly porous carbonate rocks. *Journal of Structural Geology,* 28**,** 1214-1227.

Mollema, P. & Antonellini, M. 1996. Compaction bands: a structural analog for anti-mode I cracks in aeolian sandstone. *Tectonophysics,* 267**,** 209-228.

Nelson, R. 1981. Significance of Fracture Sets Associated with Stylolite Zones1.

Nixon, C. 02.05. 2016 2016. *RE: ArcMap 10.3.* Type to KNUTSEN, H. H.

Npd. 2015. *30/9-1, Wellbore* [Online]. Norwegian Petroleum Directorate. Available: http://factpages.npd.no/FactPages/Default.aspx?nav1=wellbore&nav2=PageView|Exploration|All&nav3=65&culture=en [Accessed 07.01.2015 2015].

Npd. 2016a. *NPD FactMaps* [Online]. Norwegian Petroleum Directorate Available: http://gis.npd.no/factmaps/html_20/ [Accessed 09.02.2016 2016].

Npd. 2016b. *OSEBERG* [Online]. Norwegian Petroleum Directorate. Available: http://factpages.npd.no/FactPages/default.aspx?nav1=field&nav2=PageView|All&nav3=43625&culture=en [Accessed 04.05.2016 2016].

Nystuen, J. P., Müller, R., Mørk, A. & Nøttvedt, A. 2006. Fra økren til elveslette - fra land tl hav. Trias; 251-200 Ma. *In:* RAMBERG, I. B., BRYHNI, I. & NØTTVEDT, A. (eds.) *Landet blir til: Norges geologi.* Trondheim: Norsk Gegologisk Forening (NGF).

Odinsen, T., Christiansson, P., Gabrielsen, R. H., Faleide, J. I. & Berge, A. M. 2000a. The geometries and deep structure of the northern North Sea rift system. *Geological Society, London, Special Publications,* 167**,** 41-57.

Odinsen, T., Reemst, P., Van Der Beek, P., Faleide, J. I. & Gabrielsen, R. H. 2000b. Permo-Triassic and Jurassic extension in the northern North Sea: results from tectonostratigraphic forward modelling. *Geological Society, London, Special Publications,* 167**,** 83-103.

Passchier, C. W. & Trouw, R. A. 1996. *Microtectonics*, Springer.

Perez, R. J. & Boles, J. R. 2005. Interpreting fracture development from diagenetic mineralogy and thermoelastic contraction modeling. *Tectonophysics,* 400**,** 179-207.

Pluijm, B. & Marshak, S. 2004. Earth Structure. WW Norton Company, New York, London.

Pollard, D. & Segall, P. 1987. Theoretical displacements and stresses near fractures in rock: with applications to faults, joints, veins, dikes, and solution surfaces. *Fracture mechanics of rock,* 277**,** 277-349.

Priest, S. & Hudson, J. Estimation of discontinuity spacing and trace length using scanline surveys. International Journal of Rock Mechanics and Mining Sciences & Geomechanics Abstracts, 1981. Elsevier, 183-197.

Prosser, S. 1993. Rift-related linked depositional systems and their seismic expression. *Geological Society, London, Special Publications,* 71**,** 35-66.

Railsback, L. B. & Andrews, L. M. 1995. Tectonic stylolites in the 'undeformed'Cumberland Plateau of southern Tennessee. *Journal of Structural Geology,* 17**,** 911-915.

Rath, A., Exner, U., Tschegg, C., Grasemann, B., Laner, R. & Draganits, E. 2011. Diagenetic control of deformation mechanisms in deformation bands in a carbonate grainstone. *AAPG bulletin,* 95**,** 1369-1381.

Rotevatn, A., Fossen, H., Hesthammer, J., Aas, T. E. & Howell, J. A. 2007. Are relay ramps conduits for fluid flow? Structural analysis of a relay ramp in Arches National Park, Utah. *Geological Society, London, Special Publications,* 270**,** 55-71.

Rotevatn, A., Thorsheim, E., Bastesen, E., Fossmark, H. S. S., Torabi, A. & Sælen, G. in press Sequential growth of deformation bands in carbonate grainstones in the hangingwall of an active growth fault: implications for deformation mechanisms in different tectonic regimes.

Rotevatn, A., Torabi, A., Fossen, H. & Braathen, A. 2008. Slipped deformation bands: a new type of cataclastic deformation bands in Western Sinai, Suez rift, Egypt. *Journal of Structural Geology,* 30**,** 1317-1331.

Rustichelli, A., Tondi, E., Agosta, F., Cilona, A. & Giorgioni, M. 2012. Development and distribution of bed-parallel compaction bands and pressure solution seams in carbonates (Bolognano Formation, Majella Mountain, Italy). *Journal of Structural Geology,* 37**,** 181-199.

Safaricz, M. & Davison, I. 2005. Pressure solution in chalk. *Aapg Bulletin,* 89**,** 383-401.

Schlische, R. W. 1995. Geometry and origin of fault-related folds in extensional settings. *AAPG bulletin,* 79**,** 1661-1678.

Schueller, S., Braathen, A., Fossen, H. & Tveranger, J. 2013. Spatial distribution of deformation bands in damage zones of extensional faults in porous sandstones: Statistical analysis of field data. *Journal of Structural Geology,* 52**,** 148-162.

Schultz, R. A. & Fossen, H. 2002. Displacement–length scaling in three dimensions: the importance of aspect ratio and application to deformation bands. *Journal of Structural Geology,* 24**,** 1389-1411.

Schultz, R. A. & Fossen, H. 2008. Terminology for structural discontinuities. *AAPG bulletin,* 92**,** 853-867.

Segall, P. & Pollard, D. D. 1983. Nucleation and growth of strike slip faults in granite. *Journal of Geophysical Research: Solid Earth,* 88**,** 555-568.

Sharp, I. R., Gawthorpe, R. L., Underhill, J. R. & Gupta, S. 2000. Fault-propagation folding in extensional settings: examples of structural style and synrift sedimentary response from the Suez rift, Sinai, Egypt. *Geological Society of America Bulletin,* 112**,** 1877-1899.

Shipton, Z. & Cowie, P. 2001. Damage zone and slip-surface evolution over μm to km scales in high-porosity Navajo sandstone, Utah. *Journal of Structural Geology,* 23**,** 1825-1844.

Shipton, Z. K. & Cowie, P. A. 2003. A conceptual model for the origin of fault damage zone structures in high-porosity sandstone. *Journal of Structural Geology,* 25**,** 333-344.

Soliva, R., Ballas, G., Fossen, H. & Philit, S. 2016. Tectonic regime controls clustering of deformation bands in porous sandstone. *Geology***,** G37585. 1.

Steel, R. Triassic–Jurassic megasequence stratigraphy in the Northern North Sea: rift to post-rift evolution. Geological Society, London, Petroleum Geology Conference series, 1993. Geological Society of London, 299-315.

Steel, R. & Ryseth, A. 1990. The Triassic—Early Jurassic succession in the northern North Sea: megasequence stratigraphy and intra-Triassic tectonics. *Geological Society, London, Special Publications,* 55**,** 139-168.

Sternlof, K. & Pollard, D. Deformation bands as linear elastic fractures: progress in theory and observation. AGU Fall Meeting Abstracts, 2001.

Surlyk, F., Dons, T., Clausen, C. & Higham, J. 2003. Upper cretaceous. *Millennium Atlas: Petroleum Geology of the Central and Northern North Sea.* Geological Society of London.

Taylor, J. M. 1950. Pore-space reduction in sandstones. *AAPG bulletin,* 34**,** 701-716.

Taylor, S. K., Nicol, A. & Walsh, J. J. 2008. Displacement loss on growth faults due to sediment compaction. *Journal of Structural Geology,* 30**,** 394-405.

Tondi, E. 2007. Nucleation, development and petrophysical properties of faults in carbonate grainstones: evidence from the San Vito Lo Capo peninsula (Sicily, Italy). *Journal of Structural Geology,* 29**,** 614-628.

Tondi, E., Antonellini, M., Aydin, A., Marchegiani, L. & Cello, G. 2006. The role of deformation bands, stylolites and sheared stylolites in fault development in carbonate grainstones of Majella Mountain, Italy. *Journal of Structural Geology,* 28**,** 376-391.

Tondi, E., Cilona, A., Agosta, F., Aydin, A., Rustichelli, A., Renda, P. & Giunta, G. 2012. Growth processes, dimensional parameters and scaling relationships of two conjugate sets of compactive shear bands in porous carbonate grainstones, Favignana Island, Italy. *Journal of Structural Geology,* 37**,** 53-64.

Toublanc, A., Renaud, S., Sylte, J., Clausen, C., Eiben, T. & Nådland, G. 2005. Ekofisk Field: fracture permeability evaluation and implementation in the flow model. *Petroleum Geoscience,* 11**,** 321-330.

Twiss, R. J. & Moores, E. M. 1992. *Structural geology*, Macmillan.

Ujiie, K., Maltman, A. J. & Sánchez-Gómez, M. 2004. Origin of deformation bands in argillaceous sediments at the toe of the Nankai accretionary prism, southwest Japan. *Journal of structural geology,* 26**,** 221-231.

Vajdova, V., Baud, P. & Wong, T. F. 2004. Compaction, dilatancy, and failure in porous carbonate rocks. *Journal of Geophysical Research: Solid Earth,* 109.

Vollset, J. & Doré, A. G. 1984. *A revised Triassic and Jurassic lithostratigraphic nomenclature for the Norwegian North Sea*, Oljedirektoratet.

Walderhaug, O. 1996. Kinetic modeling of quartz cementation and porosity loss in deeply buried sandstone reservoirs. *AAPG bulletin,* 80**,** 731-745.

Walsh, J. & Watterson, J. 1987. Distributions of cumulative displacement and seismic slip on a single normal fault surface. *Journal of Structural Geology,* 9**,** 1039-1046.

Walsh, J., Watterson, J., Heath, A. & Childs, C. 1998. Representation and scaling of faults in fluid flow models. *Petroleum Geoscience,* 4**,** 241-251.

Welton, J. E. 1984. *SEM petrology atlas*, American Association of Petroleum Geologists Tulsa^ eOklahoma Oklahoma.

Wennberg, O. P., Casini, G., Jahanpanah, A., Lapponi, F., Ineson, J., Wall, B. G. & Gillespie, P. 2013. Deformation bands in chalk, examples from the Shetland Group of the Oseberg Field, North Sea, Norway. *Journal of Structural Geology,* 56**,** 103-117.

Wennberg, O. P., Malm, O., Needham, T., Edwards, E., Ottesen, S., Karlsen, F., Rennan, L. & Knipe, R. 2008. On the occurrence and formation of open fractures in the Jurassic reservoir sandstones of the Snøhvit Field, SW Barents Sea. *Petroleum Geoscience,* 14**,** 139-150.

Weyl, P. K. 1959. Pressure solution and the force of crystallization: a phenomenological theory. *Journal of Geophysical Research,* 64**,** 2001-2025.

Yielding, G., Badley, M. E. & Roberts, A. M. 1992. The structural evolution of the Brent Province. *Geological Society, London, Special Publications,* 61**,** 27-43.

Zhou, W., Apkarian, R., Wang, Z. L. & Joy, D. 2006. Fundamentals of Scanning Electron Microscopy (SEM). *Scanning Microscopy for Nanotechnology.* Springer.

Ziegler, P. 1987. Compressional intra-plate deformations in the Alpine foreland—an introduction. *Tectonophysics,* 137**,** 1-5.

Ziegler, P. A. & Maatschappij's-Gravenhage, K. N. P. 1982. Geological atlas of western and central Europe.

Zuluaga, L. F., Fossen, H. & Rotevatn, A. 2014. Progressive evolution of deformation band populations during Laramide fault-propagation folding: Navajo Sandstone, San Rafael monocline, Utah, USA. *Journal of Structural Geology,* 68**,** 66-81.

Appendix

Appendix I: Scanline

Appendix II: Thin sections

Appendix III: Topology

Appendix I: Scanline

Table AI.1: The scanline data

Well: 30/9-B 46 A From: 3346 m To: 3342 m Measured distance: 4 m Facies: 4. Shredded, intraclastic chalk, shear deformed mass flows. Structures notation: DB/Fr • Deformation band /Fracture Fr • Fracture FrI • Fracture induced Sty • Stylolite	Depth (m MD)	Type structure	Orientation to the scanline		Length (cm)
			Left	Right	
	3346.000	-	-	-	-
	3345.925	-	-	-	-
	3345.92	DB/Fr	121	128	1
	3345.917	DB/Fr	119	131	3.5
	3345.915	DB/Fr	107	108	1.8
	3345.9135	DB/Fr	93	100	0.9
	3345.91	DB/Fr	137	121	1.3
	3345.908	DB/Fr	99	116	2
	3345.906	DB/Fr	137	125	2.4
	3345.90	DB/Fr	128	129	3
	3345.892	DB/Fr	138	141	4.4
	3345.89	DB/Fr	113	113	2.7
	3345.888	DB/Fr	95	97	0.6
	3345.886	DB/Fr	-	124	0.5
	3345.883	DB/Fr	115	114	1.20
	3345.881	DB/Fr	113	110	3.9
	3345.878	DB/Fr	90	96	1.5
	3345.875	DB/Fr	107	103	2.2
	3345.871	DB/Fr	142	134	1
	3345.866	DB/Fr	88	85	14
	3345.865	DB/Fr	121	122	1.3
	3345.86	DB/Fr	128	130	2.2
	3345.857	DB/Fr	119	125	2.5

	3345.854	DB/Fr	-	112	1.6
	3345.849	DB/Fr	129	119	1.6
	3345.849	DB/Fr	103	102	2
	3345.846	DB/Fr	119	110	1.4
	3345.842	DB/Fr	123	140	8.2
	3345.837	DB/Fr	112	121	2.5
	3345.833	DB/Fr	77	75	3
	3345.831	DB/Fr	104	106	5.5
	3345.824	DB/Fr	108	118	3.7
	3345.816	DB/Fr	120	125	4.4
	3345.81	DB/Fr	119	134	2.4
	3345.808	DB/Fr	121	123	1.5
	3345.804	DB/Fr	104	113	2
	3345.799	DB/Fr	134	127	3
	3345.798	DB/Fr	134	120	3.2
	3345.797	DB/Fr	134	120	3.2
	3345.790	DB/Fr	129	123	2
	3345.785	DB/Fr	119	120	1.2
	3345.784	DB/Fr	133	130	0.9
	3345.780				
	3345.765				
	3345.761	DB/Fr	95	98	0.4
	3345.760	DB/Fr	128	130	0.9
	3345.758	DB/Fr	110	112	0.3
	3345.755	DB/Fr	120	120	0.6
	3345.754	DB/Fr	162	160	1
	3345.751	DB/Fr	115	120	0.7
	3345.746	DB/Fr	140	141	0.6
	3345.745	DB/Fr	140	100	1
	3345.742	DB/Fr	135	110	0.6
	3345.741	DB/Fr	130	145	1
	3345.731	DB/Fr	140	140	1.2
	3345.724	DB/Fr	152	149	1.3
	3345.712	DB/Fr	135	135	0.7
	3345.708	DB/Fr	140	140	-
	3345.704	DB/Fr	133	133	0.2
	3345.701	DB/Fr	95	95	1
	3345.700	DB/Fr	145	145	1.4
	3345.696	DB/Fr	130	130	0.5
	3345.694	DB/Fr	155	153	0.8
	3345.692	DB/Fr	130	130	0.9
	3345.687	DB/Fr	142	141	
	3345.674	DB/Fr	155	155	
	3345.659	FrI	91	150	16.5
	3345.651	DB/Fr	90	74	2.7

	3345.648	DB/Fr	114	85	
	3345.633	DB/Fr	140	127	
	3345.630	DB/Fr	130	129	
	3345.615				
	3345.613				
	3345.597	St	33	30	26.1
	3345.588	DB/Fr	124	126	
	3345.585	DB/Fr	115	118	
	3345.580				
	3345.570				
	3345.504	FrI	90	40	14
	3345.485	DB/Fr	127	136	2.1
	3345.480	St	35	35	24
	3345.474	DB/Fr	121	135	0.5
	3345.473	DB/Fr	121	115	0.5
	3345.472	DB/Fr	121	100	0.5
	3345.468	DB/Fr	136	145	1.1
	3345.466	DB/Fr	135	132	0.9
	3345.464	DB/Fr	130	120	1.1
	3345.462	DB/Fr	140	141	1.1
	3345.460	DB/Fr	128	116	1.7
	3345.456	DB/Fr	125	138	1.6
	3345.454	DB/Fr	122	122	1.4
	3345.453	DB/Fr	90	90	1.2
	3345.448	DB/Fr	112	126	0.8
	3345.446	DB/Fr	125	125	0.4
	3345.442	Fr	146	128	2.9
	3345.434	DB/Fr	120	132	1.5
	3345.432	DB/Fr	107	107	0.3
	3345.431	DB/Fr	131	114	1.4
	3345.424	DB/Fr	143	150	2.3
	3345.417	DB/Fr	133	135	1.1
	3345.410	DB/Fr	90	90	0.9
	3345.407	DB/Fr	125	125	0.6
	3345.405	DB/Fr	130	130	1
	3345.400	St	50	50	24
	3345.398	DB/Fr	110	90	0.4
	3345.396	DB/Fr	132	-	0.3
	3345.393	st/f	40	28	1.4
	3345.389	st/f	-	31	1
	3345.384	DB/Fr	145	115	0.7
	3345.378	DB/Fr	130	130	0.4
	3345.377	DB/Fr	120	128	0.4
	3345.375	st/f	30	22	10
	3345.372	DB/Fr	129	136	2.2

	3345.370	DB/Fr	148	140	1.4
	3345.366	DB/Fr	135	140	1.4
	3345.363	DB/Fr	90	90	1.2
	3345.357	DB/Fr	115	122	0.9
	3345.352	DB/Fr	147	134	1.8
	3345.348	DB/Fr	113	93	0.9
	3345.346	DB/Fr	128	115	1.6
	3345.338	DB/Fr	136	115	1
	3345.335	DB/Fr	116	141	1
	3345.331	DB/Fr	127	129	1.8
	3345.330	sf/f	85	77	0.7
	3345.317				
	3345.279	DB/Fr	115	116	0.7
	3345.278	DB/Fr	127	127	1.1
	3345.273	DB/Fr	-	127	0.7
	3345.269	DB/Fr	128	128	1
	3345.268	DB/Fr	110	110	1.1
	3345.268				
	3345.223	DB/Fr	115	115	3.3
	3345.201	DB/Fr	106	106	4
	3345.185	DB/Fr	128	128	2
	3345.177	DB/Fr	140	120	2.3
	3345.170	DB/Fr	137	130	2.5
	3345.168	DB/Fr	132	132	2.30
	3345.165	DB/Fr	118	118	2.4
	3345.153	DB/Fr	130	130	1.3
	3345.140	DB/Fr	75	55	1
	3345.139	DB/Fr	57	57	1.2
	3345.130	DB/Fr	122	122	2.2
	3345.126	DB/Fr	122	122	2.2
	3345.120	DB/Fr	105	120	1.4
	3345.113	DB/Fr	130	130	0.7
	3345.111	DB/Fr	145	145	0.6
	3345.107	DB/Fr	99	75	1.5
	3345.099	DB/Fr	131	112	1.3
	3345.092	DB/Fr	130	130	1
	3345.090	DB/Fr	78	60	0.4
	3345.082	DB/Fr	100	100	0.7
	3345.079	DB/Fr	133	133	0.8
	3345.077	DB/Fr	120	92	0.7
	3345.074	DB/Fr	122	122	1.5
	3345.065	DB/Fr	93	93	1.5
	3345.061	DB/Fr	70	70	2.8
	3345.047	DB/Fr	115	115	2
	3345.045	DB/Fr	82	95	1.5

	3345.035	DB/Fr	138	138	2.2
	3345.025	DB/Fr	132	132	0.8
	3345.021	DB/Fr	-	55	0.7
	3345.015	DB/Fr	116	95	1
	3345.013	DB/Fr	90	90	0.8
	3345.010	DB/Fr	120	120	0.9
	3345				
	3344.921				
	3344.917	DB/Fr	144	132	1.5
	3344.915	DB/Fr	127	127	1.1
	3344.913	DB/Fr	125	125	2
	3344.908	DB/Fr	90	98	1.5
	3344.902	DB/Fr	126	126	2.2
	3344.898	DB/Fr	143	134	1.7
	3344.895	DB/Fr	81	88	1
	3344.890	DB/Fr	90	90	1.3
	3344.883	DB/Fr	165	159	1
	3344.855	FrI	44	83	3.2
	3344.846	DB/Fr	138	138	1.3
	3344.837	DB/Fr	142	142	2.6
	3344.834				
	3344.812	DB/Fr	132	132	1.4
	3344.811	DB/Fr	128	128	1.2
	3344.810	DB/Fr	100	114	0.4
	3344.806	DB/Fr	117	117	1.3
	3344.804	DB/Fr	137	125	1
	3344.802	DB/Fr	142	160	1
	3344.7985	DB/Fr	118	118	0.5
	3344.797	DB/Fr	137	137	0.6
	3344.791	DB/Fr	138	138	1.8
	3344.789	FrI	30	30	16.5
	3344.778	DB/Fr	140	140	1.1
	3344.773	DB/Fr	106	106	1.2
	3344.771	DB/Fr	127	127	1.2
	3344.768	DB/Fr	140	140	1.3
	3344.765	DB/Fr	112	112	1
	3344.759	DB/Fr	106	106	0.9
	3344.748	DB/Fr	130	130	0.6
	3344.747	DB/Fr	141	141	0.6
	3344.741	DB/Fr	101	101	0.5
	3344.735				
	3344.715	FrI	100	100	7.2
	3344.704	DB/Fr	140	140	cutting mark
	3344.693	DB/Fr	115	115	1.4

	3344.684	DB/Fr	116	116	2.3
	3344.677	DB/Fr	125	125	2
	3344.669	DB/Fr	127	127	
	3344.663	Fr	117	117	1.5
	3344.660	Fr	130	130	1
	3344.656	Fr	129	129	1
	3344.653	Fr	127	127	1.1
	3344.649	Fr	131	131	1.3
	3344.643	Fr	133	133	4
	3344.641	St	27	27	15
	3344.634	Fr	125	125	0.4
	3344.630	Fr	140	140	1.1
	3344.623	Fr	94	94	1
	3344.617	St	40	40	
	3344.614	Fr	114	114	0.4
	3344.612	St	38	38	10.5
	3344.599	St	52	52	0.7
	3344.588	DB/Fr	112	98	1.1
	3344.582	Fr	141	141	2
	3344.574	DB/Fr	118	118	1
	3344.573	DB/Fr	83	83	0.3
	3344.571	DB/Fr	133	133	0.6
	3344.569	DB/Fr	78	78	0.3
	3344.568	DB/Fr	130	130	0.4
	3344.565	DB/Fr	124	124	0.7
	3344.563	DB/Fr	100	100	0.4
	3344.557	DB/Fr	112	112	2.1
	3344.555	Fr	90	90	3
	3344.550	FrI	81	81	3.9
	3344.548	DB/Fr	80	80	0.7
	3344.543	DB/Fr	86	86	1.4
	3344.542	Fr	30	30	8
	3344.535	Fr	30	30	9.4
	3344.532	Fr	33	33	1.4
	3344.516	Fault	79	79	13.3
	3344.502	DB/Fr	88	88	1.3
	3344.493				
	3344.428	DB/Fr	80	80	1.3
	3344.425	DB/Fr	60	60	1.5
	3344.423	DB/Fr	79	57	1.4
	3344.420	DB/Fr	85	85	0.8
	3344.417				
	3344.408	DB/Fr	120	120	1.6
	3344.403	DB/Fr	122	122	2.5
	3344.397	DB/Fr	121	121	1

	3344.395	DB/Fr	95	95	
	3344.390	DB/Fr	140	147	0.9
	3344.383	DB/Fr	117	117	2.1
	3344.380	DB/Fr	120	120	0.3
	3344.379				
	3344.343	DB/Fr	104	104	1.2
	3344.339	DB/Fr	130	130	1.2
	3344.337				
	3344.040				
	3344				
	3343.942				
	3343.931	DB/Fr	122	108	2.1
	3343.927	DB/Fr	95		2
	3343.922	DB/Fr	133		0.7
	3343.920	DB/Fr	123		0.4
	3343.906	DB/Fr	122	110	2.1
	3343.901	DB/Fr	133	133	2
	3343.899	DB/Fr	125	125	0.9
	3343.895	DB/Fr	104	104	1.7
	3343.891	DB/Fr	79	100	1.2
	3343.888	DB/Fr	92	92	1.5
	3343.883	DB/Fr	120	120	2.1
	3343.876	DB/Fr	96	96	2.8
	3343.864	DB/Fr	117	117	2.3
	3343.859	Fr	101	128	3.5
	3343.857	DB/Fr	110	135	1.7
	3343.850	DB/Fr	117	117	0.9
	3343.847	DB/Fr	115	115	0.8
	3343.845	DB/Fr	88	88	0.4
	3343.844	DB/Fr	140	125	0.4
	3343.842	DB/Fr	126	113	0.4
	3343.838	DB/Fr	112	112	1.1
	3343.829	DB/Fr	128	130	0.6
	3343.828	DB/Fr	125	90	0.7
	3343.824	DB/Fr	122	122	
	3343.818	DB/Fr	104	104	1.5
	3343.815	DB/Fr	77	125	1.3
	3343.805	DB/Fr	145	130	1.5
	3343.795	DB/Fr	120	-	1.1
	3343.792	DB/Fr	115	-	1
	3343.791	DB/Fr	137	-	0.6
	3343.783	DB/Fr	109	109	2.1
	3343.776	DB/Fr	86	116	2
	3343.773	DB/Fr	122	138	1
	3343.766	DB/Fr	111	111	0.8

	3343.765	FrI	92	84	11.3
	3343.759	DB/Fr	93	93	1.3
	3343.755	DB/Fr	125	125	1.3
	3343.752	DB/Fr	102	114	0.5
	3343.751	DB/Fr	113	113	1
	3343.744	DB/Fr	95	95	1
	3343.740	DB/Fr	135	135	1
	3343.736	DB/Fr	96	96	0.5
	3343.735				
	3343.708	DB/Fr	138	-	0.5
	3343.703	DB/Fr	112	112	2.7
	3343.702	DB/Fr	104	104	1.3
	3343.698	DB/Fr	123	123	1.3
	3343.696	DB/Fr	78	78	0.6
	3343.692	DB/Fr	128	128	2
	3343.688	DB/Fr	125	113	1.1
	3343.686	DB/Fr	98	98	1.8
	3343.681	DB/Fr	120	120	1.4
	3343.677	DB/Fr	137	119	2.5
	3343.663	DB/Fr	110	110	0.8
	3343.652	DB/Fr	113	113	0.9
	3343.650	DB/Fr	130	130	1.5
	3343.6425	DB/Fr	112	112	2.7
	3343.638	DB/Fr	105	105	2.8
	3343.632	DB/Fr	124	124	1.6
	3343.628	DB/Fr	117	117	1
	3343.625	DB/Fr	100	100	3.7
	3343.623	DB/Fr	93	102	2.9
	3343.617	DB/Fr	70	.	1.5
	3343.611	DB/Fr	104	104	1.2
	3343.610	DB/Fr	90	90	1.8
	3343.605	DB/Fr	93	113	1.4
	3343.603	DB/Fr	70	-	0.4
	3343.599	DB/Fr	90	90	0.8
	3343.597	DB/Fr	87	87	0.8
	3343.594	DB/Fr	125	125	0.6
	3343.591	DB/Fr	83	-	0.9
	3343.584				
	3343.547	DB/Fr	120	88	2.7
	3343.539	DB/Fr	82	82	1.5
	3343.534	DB/Fr	111	130	1.5
	3343.522	DB/Fr	95	95	2.9
	3343.517	DB/Fr	113	113	3.2
	3343.510	DB/Fr	127	127	1.5
	3343.504	DB/Fr	146	146	2

	3343.493	DB/Fr	127	113	2.4
	3343.492	DB/Fr	105	105	0.4
	3343.478	DB/Fr	101	101	0.8
	3343.475	DB/Fr	130	130	1.1
	3343.472	DB/Fr	131	131	0.8
	3343.469	DB/Fr	127	127	0.9
	3343.467	DB/Fr	83	96	1.2
	3343.464	DB/Fr	118	118	3.4
	3343.455	DB/Fr	119	119	2.3
	3343.448	DB/Fr	138	138	2.4
	3343.446	DB/Fr	138	138	2.2
	3343.444	DB/Fr	100	100	1.2
	3343.440	DB/Fr	105	105	0.8
	3343.439	DB/Fr	124	118	1.2
	3343.436	DB/Fr	105	110	0.5
	3343.435	DB/Fr	144	144	0.7
	3343.432	DB/Fr	132	132	1.2
	3343.429	DB/Fr	134	134	1.3
	3343.425	DB/Fr	127	96	0.9
	3343.417	DB/Fr	125	125	0.9
	3343.416	DB/Fr	123	133	1.2
	3343.415	DB/Fr	82	82	0.7
	3343.410	DB/Fr	70	70	0.7
	3343.405	DB/Fr	135	135	1
	3343.400	FrI	92	104	13.7
	3343.399	DB/Fr	74	74	1
	3343.396	DB/Fr	73	91	1.2
	3343.387	DB/Fr	132	132	1.7
	3343.380	DB/Fr	96	62	0.7
	3343.377	DB/Fr	115	115	0.9
	3343.370	DB/Fr	152	139	1.6
	3343.365	DB/Fr	117	117	0.4
	3343.356	DB/Fr	73	73	0.9
	3343.354	DB/Fr	141	141	0.8
	3343.347	DB/Fr	62	62	0.9
	3343.343	DB/Fr	125	125	2.4
	3343.334	DB/Fr	99	110	2.4
	3343.329	DB/Fr	50	67	1
	3343.312	DB/Fr	118	92	0.8
	3343.303	DB/Fr	-	102	
	3343.298	DB/Fr	95	95	2
	3343.283	DB/Fr	123	123	1.1
	3343.261	DB/Fr	103	-	1.3
	3343.244	DB/Fr	150	150	2
	3343.242	DB/Fr	95	95	0.9

	3343.234	St	48	48	3.5
	3343.232	Fr	127	127	0.4
	3343.228	Fr	133	133	0.5
	3343.223	Fr	143	103	0.7
	3343.221	Fr	122	137	0.7
	3343.217	DB/Fr	-	106	1
	3343.208	DB/Fr	156	170	3.2
	3343.200	DB/Fr	150	167	1.5
	3343.194	DB/Fr	145	145	2
	3343.189	St	24	24	13
	3343.184	Fault	45	45	18.7
	3343.168	Fr	40	40	8
	3343.158	Fr	40	40	7
	3343.114	Fr	135	-	2.2
	3343.060	DB/Fr	108	108	6.4
	3343.046	DB/Fr	100	100	4.5
	3343				
	3342.921				
	3342.894	DB/Fr	98	98	
	3342.866	DB/Fr	92	92	
	3342.857	St/Fr	147	147	8.7
	3342.8942	FrI	70	70	17.5
	3342.772				
	3342.722	St/Fr	35	35	7.4
	3342.635	DB/Fr	142	142	2.1
	3342.604	DB/Fr	78	90	5.8
	3342.555	DB/Fr	140	140	3.9
	3342.484	DB/Fr	87	87	3.3
	3342.478	DB/Fr	80	80	3.2
	3342.454	DB/Fr	125	125	1.1
	3342.429	DB/Fr	83	130	1.1
	3342.427	DB/Fr	70	70	1.3
	3342.415	DB/Fr	138	138	2
	3342.406	DB/Fr	78	78	3.3
	3342.382	FrI	127	127	6.3
	3342.360				
	3342.325				
	3342.000				

Appendix II: Thin section

Table AII.1: Thin section from well 30/9-B 44 B

Sample number (plug)	Depth (m MD)	Description
215	4305.50	

Table AII.2: Thin section from well 30/9-B 46 A

Sample number (plug)	Depth (m MD)	Description
1	3335.76	Visible stylolite and conglomerate in host rock
2	3336.26	Stylolite with visible
3	3337.10	
4	3340.72	
5	3342.67	
6	3343.17	
7	3344.51	
8	3349.33	
9	3354.55	
10	3359.81	
11	3335.84	Visible stylolite and conglomerate in host rock
12	3346.64	
13	3349.64	
14	3359.80	
15	3365.40	
H8	3335.75	Visible stylolite and conglomerate in host rock
H11	3336.50	
H24	3339.75	
H32	3341.75	
H36	3342.75	
H44	3344.75	
H48	3345.75	

Appendix III: Topology

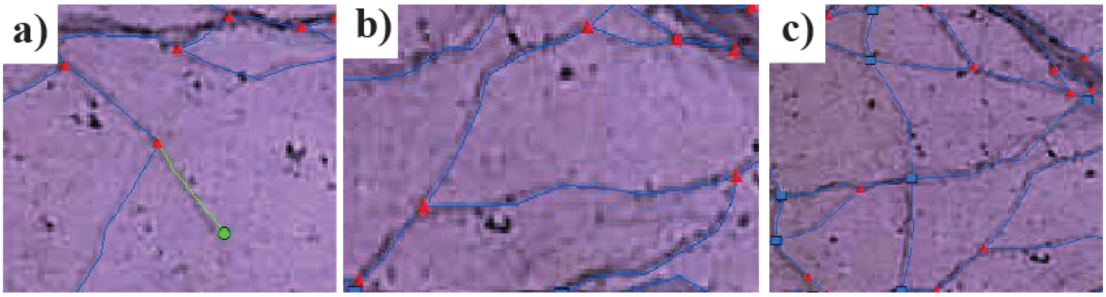

Figure A.1: The different types of nodes a) I node, b) Y node and c) X node.

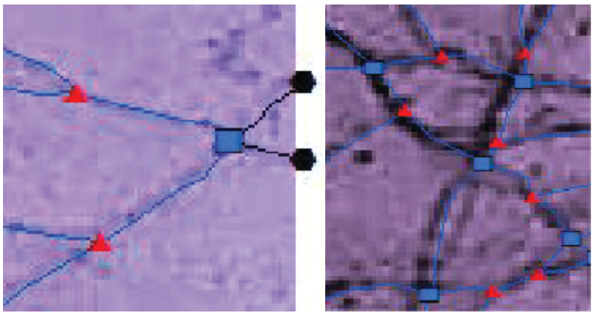

Figure A.2: To the left is a E node and the right is a star crossing note .

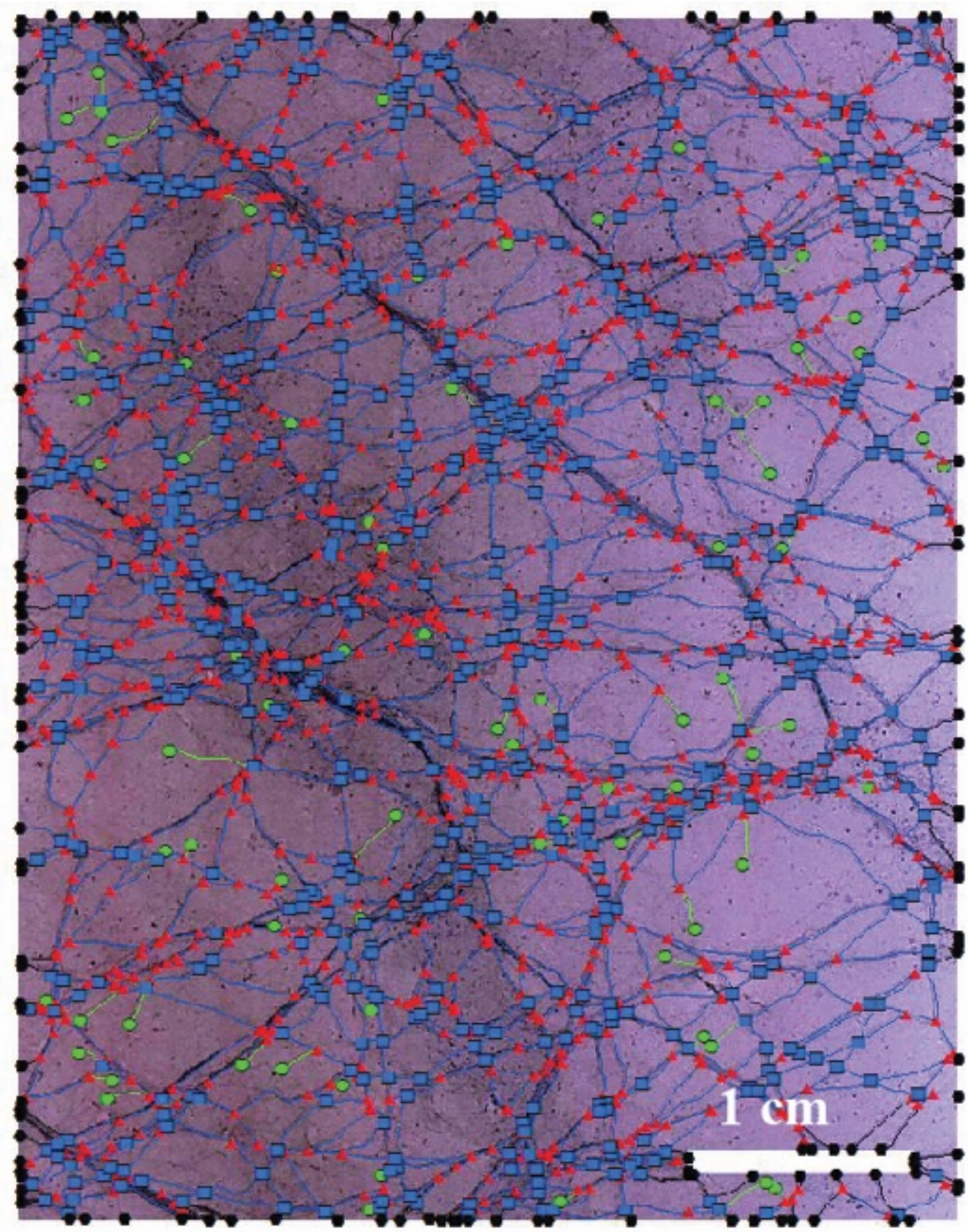

Figure A.3: The topology pattern made on the image in Fig. 5.9c at 3344.95 m MD.

Table AIII.1: Data from the plot in ArcMap

Sample area (cm^2)	Total Trace-length (cm)	Nodes				Branch		
		I	Y	X	E	II	IC	CC
21.4	297,6	77,0	1065,0	724,0	148,0	0,0	72,0	2914,0

Table AIII.2: Data from Topology Analysis plot

No. Lines	No. Branches	Average Line Length (cm)	Average Branch Length (cm)	Cb
571,0	3084,0	0,5	0,1	2,0

Table AIII.3: Data from Topology Analysis plot

Connect/Line	Connect/Branch	Frequency (Branches/area)	Intensity (T.T.L./area)	Dimenstionless intensity

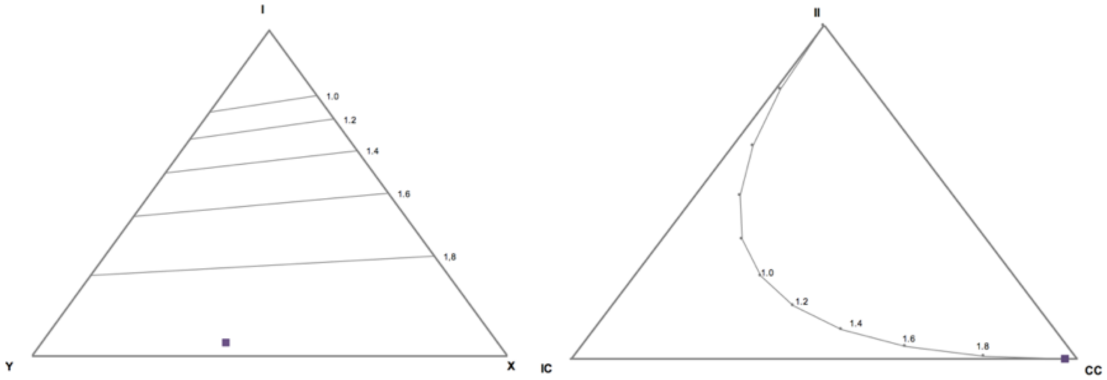

Figure A.4: The result from the topology measurement